LUDWIG MAXIMILIAN UNIVERSITÄT

MASTER THESIS

The Influence of Environment on the Stellar Kinematics of Brightest Cluster Galaxies

---

Author:
Maximilian KÜHN

Supervisors:
Dr. Rhea-Silvia REMUS
PD Dr. Klaus DOLAG

A thesis submitted in fulfillment of the requirements
for the degree of Master of Science

in the

Computational Astrophysics Group
Physics Department

May 7, 2020

LUDWIG MAXIMILIAN UNIVERSITÄT

MASTERARBEIT

Umgebungseinflüsse auf die Stellare Kinematik der Hellsten Galaxie des Galaxienhaufens

Autor:
Maximilian KÜHN

Betreuer:
Dr. Rhea-Silvia REMUS
PD Dr. Klaus DOLAG

Eine Masterarbeit, eingereicht unter Erfüllung der Kriterien
des Abschlusses Master of Science

in der

Computational Astrophysics Group
Physik Fakultät

May 7, 2020

Acknowledgements

An dieser Stelle möchte ich mich bei den Menschen bedanken, ohne die das Fertigstellen dieser Arbeit nicht möglich gewesen wäre.

Manchmal wusste ich nicht, wie ich an einem Problem weiterkommen würde, aber ich wusste immer, dass ich bei Klaus, Rhea und Felix nachfragen konnte. Ich möchte euch danken, dass ich mich durch euch nie verloren gefühlt habe und unglaublich viel gelernt habe.

Es gab Tage, da war meine Motivation am Projekt zu arbeiten nicht besonders groß. Ich möchte mich bei allen Mitgliedern der HydroSims Gruppe bedanken, die dazu beigetragen haben ein Klima zu schaffen, in dem ich mich willkommen und nützlich gefühlt habe und deshalb gerne jeden Tag zur Universitätssternwarte gegangen bin.

Es kam durchaus vor, dass ich an der Bedeutung meiner Ergebnisse gezweifelt habe. Ich möchte mich bei allen, insbesondere bei Andreas Burkert, bedanken, die mich durch Anregungen und Lob unterstützt haben.

Ich hätte niemals diese Bandbreite an Größen untersuchen können, wenn ich von grundauf hätte anfangen müssen. Ich möchte mich bei Felix bedanken, dass er mir zahlreiche seiner Routinen zur Verfügung gestellt und erklärt hat.

Diese gesamte Arbeit wurde wegen der Ausbreitung des Coronavirus' während der staatlich verordneten Ausgangsbeschränkung geschrieben. Ich möchte mich bei meiner Freundin Miriam bedanken, ohne die ich in dieser Zeit nicht nur etliche Barthaare, sondern vermutlich auch meinen Verstand verloren hätte.

Schließlich möchte ich mich bei meinen Eltern bedanken, die mich immer und überall, wo sie konnten, unterstützt haben.

“Nobody ever figures out what life is all about, and it doesn’t matter. Explore the world. Nearly everything is really interesting if you go into it deeply enough.”

Richard P. Feynman

LUDWIG MAXIMILIAN UNIVERSITÄT

Abstract

University Observatory Munich
Physics Department

Master of Science

The Influence of Environment on the Stellar Kinematics of Brightest Cluster Galaxies

by Maximilian KÜHN

When I try to explain the subject of my master thesis to people that are not involved in the dark arts of astrophysics, I like to use the following analogy:
Psychological research tells us that we, as homo sapiens, are influenced by two main mechanisms. First, our genes. This includes specific traits directly inherited from our parents, our grandparents etc. and more general traits, slowly adjusted during the course of evolution. Second, our environment. This includes our immediate environment e.g. the upbringing in our family, friends and a broader environment like the social structures we live in.
In astrophysics, more precisely in the context of galaxy formation, we can find parallels. Genes and inheritance can be interchanged with mergers. The morphology (phenotype) and the kinematics (behaviour) of galaxies are directly influenced by the characteristics of their ancestors. This includes their mass, angular momentum, gas content etc. This has been observed by many astronomers (e.g. Emsellem, Cappellari, Peletier, et al. (2004)). By using cosmological computer simulations it is possible to construct merger trees displaying a galaxy's ancestry that is similar to family trees.
To what extend the stellar movement in galaxies is a product of their environment, however, is rather unclear. Brightest cluster galaxies, sitting in the gravitational centre of galaxy clusters, act as a link between galaxy and cluster physics. If cluster characteristics influence galaxy kinematics this effect should be most obvious in BCGs.
In this master thesis, I take an in-depth look at the kinematics of 398 BCGs from the MAGNETICUM Pathfinder simulations (Dolag et al., in prep., Hirschmann et al., 2014, Ragagnin et al., 2017). First, their kinematics are studied at z=0. Then 250 galaxies are traced to z=2. This allows to investigate the temporal evolution of many kinematical and environmental properties. The statistical evolution of these properties is examined and finally a case study of 12 BCGs is completed where the development of kinematics and environment is set in relation to one another. Six of these galaxies end up in a non-cool core environment whereas the cluster of four of these BCGs keeps its cool core.
The findings suggest that there is a correlation between coolcoreness and the h_4 parameter. Furthermore, the development of a cool-core is a continuous process that correlates with strong mass accretion between $2 > z > 1.5$ for the sample of 12 BCGs in this case study.

Contents

Chapter 1

The Play's the Thing, wherein I'll catch the Conscience of the King

Imagine you are seated in a festival theatre. Every evening, many people want to watch the show. Today, you only got one of the cheaper seats in the far back. The curtain called, the lights dimmed and the show begins. The theatre is pitch-black now. There is no limelight that illuminates the stage, instead, every actor wears a small lamp making them look like fireflies. The actors are positioned in multiple rows on this enormous stage. You can see the ones in the front clearly but struggle to see beyond that. You take out the opera glasses from your pocket. Many more actors become visible. You know that they are likely from the rows further back where the lights seem dimmer, yet you have the impression that the show is displayed on a screen rather than on a stage with actual depth. There is also this hazy light transcending the audience that makes it hard for you to focus on stage. You think to yourself: 'I'm pretty sure I would see much more if not every other person would look at their phone screens'.

That is the quest and the challenge of astronomers. They search for the best seats and build increasingly sophisticated opera glasses. There is the *Very Large Telescope* (**VLT**) on the Cerro Paranal in northern Chile, far away from any city lights to grant a minimally polluted view of the night sky of the southern hemisphere. Four 8.2m wide mirrors are the heart and soul of this telescope. With our current materials, it is so far impossible to manufacture mirrors (in one piece) much larger than that because they would break under their own weight. But boundaries spark creativity. So the mirrors can be synced together in order to effectively quadruple their size and resolution. This allows the actors in the furthest rows to become visible. However, the award for the best seat, the prime lodge so to say, goes to the *Hubble Space Telescope* (**HST**). Like the name suggests, stationed in space, it has a clear view on astronomical objects, free from the influence of Earth's atmosphere. And the race still goes on. 2021 is the year of the planned launch of the *James-Webb-Telescope*. Similar to the HST in the fact that it is stationed in space (although in one of Earth's Lagrangian points - roughly 4 times further away than our moon), it will have unparalleled resolution. And still, no matter how precise and well-engineered these instruments are, there are fundamental difficulties that can only be overcome by understanding the physical processes within and around these objects.

Therefore, in this chapter, I want to focus on the actors. Before we can interpret the play, we need to know who they are, what they want and where they come from.

1.1 Prologos: Protagonists on the Universe Stage

A lot of people might say that it is misleading to describe astronomical objects in a way that suggests that they have a conscience. In my opinion this is insincere. We use the language of logic e.g. in maths in order to fool-proof ourselves. In maths, everything is proven and can be reduced to basic principles if need be. There is very little space for conceptual human error. In physics, however, it is almost never possible to give an unbiased account of observations. Even if machines collect all the data, in the end we are the ones who interpret that data. And the way we think, the way we derive causalities, is imprinted in our 'objective' description of these observations. This is especially important when we classify things. Classification is a reoccurring method and of central importance in this chapter. We classify things, immediately, by what is most obvious to us. The first classification of galaxies was done by *Edwin Hubble* depending on the way they look while observing them through an optical telescope. He categorised them in what is known as the *Hubble Sequence* of Galaxies. The details will be discussed in the following subsections but suffice to say that, on a most basic level, there are two types. One type is an ellipsoidally shaped object, the other is a flat disk usually with distinct spiral arm features. The Hubble Sequence has been thought of as an evolutionary scheme. That is why the first type is called *Early Type Galaxies* (**ETG**) and the second *Late Type Galaxies* (**LTG**). We will see that modern galaxy formation assumes the exact opposite, yet the nomenclature still persists.

We see that science might never be free from human bias. Nevertheless, already in this young century, scientists managed to detect gravitational waves, decoded the human genome and built the first prototypes of self-driving cars. The beauty of science is that there is no central dogma. New discoveries can always spark innovation by falsifying or at least questioning everything discovered before that - including everything written in this thesis.

1.1.1 Galaxy Clusters - Kingdoms in the Universe

'Galaxy clusters are the largest gravitationally bound and relaxed structures in the universe'. This (or variations thereof) is the first sentence in the majority of all cluster papers. But what does it mean? First, we need to have a concept of structure formation in our universe. The following serves as a short overview of the most important theories. For the historical development of these theories and the role numerical simulations played to establish these theories see Frenk and S. White (2012). An introduction to cosmic inflation can be found in Watson (2000).

Right after the *Big Bang*, roughly 13.7 billion years ago, space was filled with a hot and dense plasma. A plasma is a physical state of matter in which there are freely moving charged particles. This plasma was nearly homogeneous although there were small overdensities due to quantum fluctuations. Quantum fluctuations can be described with Heisenberg's uncertainty principle. This principle states that certain pairs of physical quantities of a particles (e.g. position and momentum) can never be predicted with arbitrary certainty even if all initial conditions are specified. This micro-scale universe experienced a phase of enormous inflation in a very short time (shorter than any time we could ever measure) such that the quantum fluctuations reached astronomical sizes. This theory of inflation is necessary to explain two key features we observe in our universe today: Our universe appears nearly flat. If it expanded drastically in an inflationary phase we might just not be able to observe a curvature because it seems as flat to us as Earth to me when I look outside my

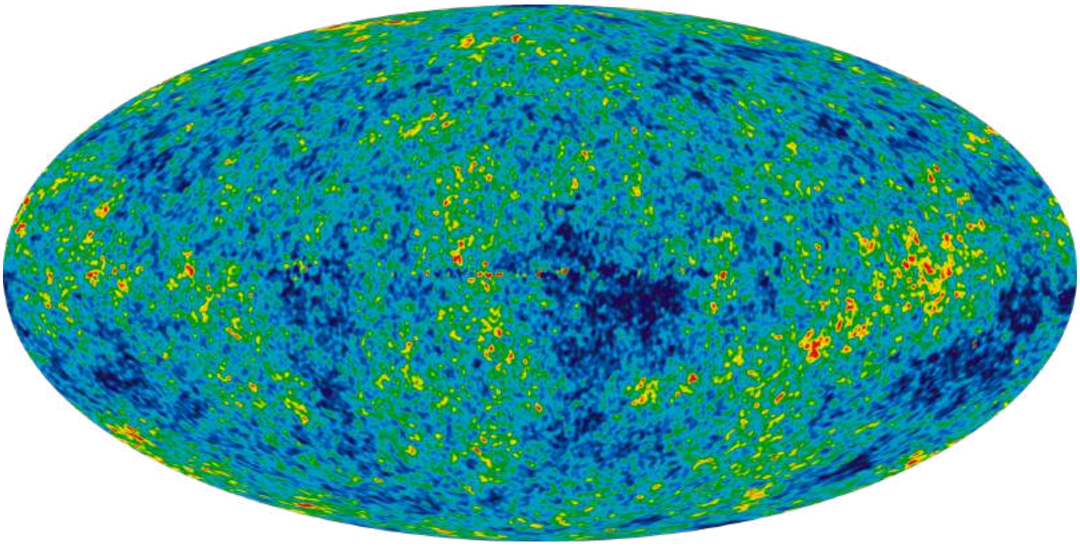

FIGURE 1.1: The cosmic microwave background. Observed with WMAP (`https://wmap.gsfc.nasa.gov/media/101080/`)

window in Munich. The theory of inflation also explains how these overdensities were not destroyed through interaction with the surroundings. They are the seeds for galaxies in our universe.

Shortly after inflation, these astronomical overdensities consisted mainly of dark matter, hence they are also called dark matter halos. The plasma was comprised of negatively charged electrons that could move freely among positively charged protons. This plasma was optically thick, i.e. non-translucent, for photons because, being electro-magnetic waves themselves, they had electro-magnetic interactions with the free electrons inside the plasma. Or in simpler terms: Photons were not able to escape the plasma. Furthermore, baryonic, i.e. visible, matter-structures could not form because they would be destroyed by these high-energy photons in an instant. However, photons do not have any influence on the dark matter halos.

When a closed volume expands, its density and temperature decrease. Since the observation of supernovae type Ia in distant galaxies (Perlmutter et al., 1999) we know that the universe is not only expanding but also expanding in an accelerated fashion. The reason for this expansion is still unknown and therefore comprised in a mysterious source called dark energy. The behaviour of this expansion, however, is relatively well understood and described by the *Friedmann-Lemaitre-Equations*. When light travels through expanding space its wavelength also expands. Objects emitting light are therefore observed with a redder colour depending on their distance. This behaviour is known as redshift. Furthermore, because of expansion, there is a point in time when the temperature, and therefore the kinetic energy of the particles in the plasma, becomes smaller than the binding energy of the electrons and protons. Nuclear fusion (cosmologists prefer the more confusing term of recombination) begins and electrons and protons can combine to form electrically neutral hydrogen atoms. After this process bound most electrons to protons, the photons were finally able to travel freely. These first photons after recombination constitute what astronomers call the cosmic microwave background (**CMB**). The observation of the CMB is central for our understanding of structure formation in the universe. The observation is shown in Fig. 1.1. These very weak radio frequencies that are distributed isotropically around the entire sky turned out to be the oldest observable light in our universe, predicted by particle physicists to be emitted almost $380,000$ years after the

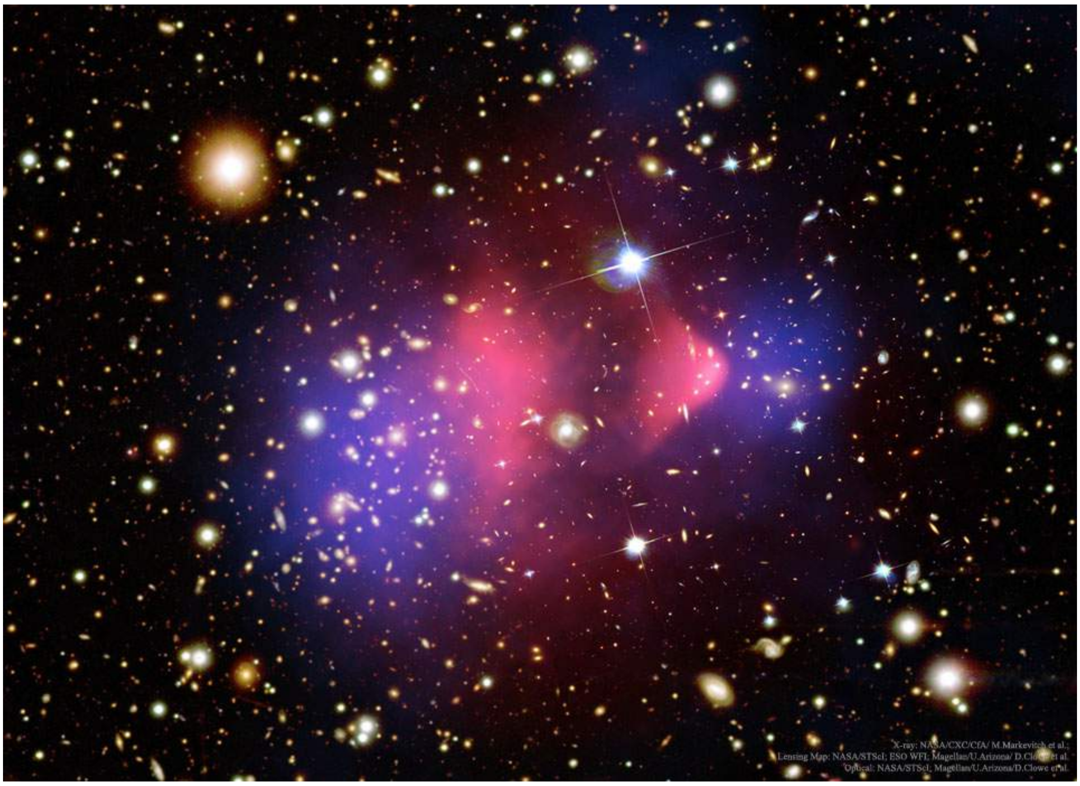

FIGURE 1.2: The Bulletcluster. Observed with Chandra (https://science.nasa.gov/matter-bullet-cluster)

big bang (Penzias and Wilson, 1965). For comparison: if the universe would be one day old, this corresponds to the first 2.5 seconds of it.
This means that after recombination, baryonic structures were able to form in these relatively cold dark matter halos. The smallest of these structures are dwarf galaxies that are believed to be fundamental building blocks of our universe (Frenk and S. White, 2012). They interact gravitationally and form more and more massive structures in what is called hierarchical growth. Galaxy clusters are on top of this hierarchy.
What I described here is known as the ΛCDM (cold dark matter with gravitational constant)- model of the universe. This is the model that I will presume in the following chapters. Although this model agrees outstandingly well with observations (notably the cosmic background fluctuations, particle horizon and predictions of baryon acoustic oscillations) note that there are alternative models that try to explain the observations differently, most notably modified Newtonian gravity (**MOND**).

Contents

Now that we know where galaxy clusters come, from we can figure out who they are. The matter contents in galaxy clusters are probably best illustrated with the composite image of the bullet cluster by the Chandra telescope (Fig. 1.2). It is important to note that the bullet cluster is special because it is actually two clusters that are colliding with each other (Clowe, Gonzalez, and Markevitch, 2004). Instead of colliding, astronomers use the term *merging* because there is practically no collision in the usual sense. There is so much space between stars that the likelihood of two stars hitting each other is extremely low.

Here we can already see the first component of a galaxy cluster: the stars. Their radiation can be described with Planck's law of thermal radiation. It is mind blowing that the same law can be used to describe the CMB that we got to know in the introduction of this chapter! However the CMB seems very cold in our observational frame and is therefore only visible in radio wavelengths. Stars are hot enough to be visible for our own eyes. If they would be much colder or hotter most of the night sky would probably seem completely dark to us. This light is what we see in the picture as white, blue and red clouds. The colour of this light depends on properties of the galaxies they are part of. I will describe galaxies in more detail in section 1.1.2. Although a cluster is inhabited by hundreds to thousands of galaxies and galaxies themselves have hundreds of billions of stars, the stellar mass accounts to only four percent of the cluster's total mass!

The most massive component in a galaxy cluster is the dark matter halo. Roughly 82% of the mass in a galaxy cluster is non-visible dark matter! This lead to strong confusion among astronomers when galaxy clusters were first observed. They believed that the total mass of a galaxy cluster could be derived in two ways: from the motion of the galaxies inside the cluster and from the radiation luminosity of the gas. These two ways lead to very different results, however. The mass derived from the motion of the galaxies was much higher. This is known as the missing mass problem. Zwicky (1933) was the first to resolve this problem with the introduction of dark matter that influences the motion of galaxies but not the radiation from the gas. Dark matter can explain many more things like the rotational curves of galaxies and the structure formation of the universe that we already learned about. The bullet cluster is one of the prime examples for the existence of dark matter. The blue clouds in Fig. 1.2 were inferred from gravitational lensing measurements (according to Einstein's theory of general relativity, mass can influence the trajectory of photons and therefore create lensing effects) and represent matter that is inside the cluster but cannot be observed with traditional methods of spectroscopy. Nevertheless the true nature of dark matter is still unknown and particle physicists are working hard to find particles with the same properties as dark matter. Before we interpret the distribution of masses in Fig. 1.2 one more component needs to be introduced.

The remaining mass of roughly 14% of the cluster's total mass is the intra cluster medium (**ICM**). This is what we can see as the pink cloud in Fig. 1.2. This gas cloud consists of highly ionised plasma. It is mainly hydrogen atoms and free electrons but also a non-negligible amount of heavier atomic cores like iron that are distributed roughly isotropically across the cluster. This gas is very hot and emits X-rays mainly because of Bremsstrahlung. Bremsstrahlung is produced when a high-energy electron is deflected in the electric field of an atomic nucleus. The electron is losing kinetic energy that is in turn transformed into radiation. Therefore the gas temperature can be inferred by measuring the Bremsstrahlung spectrum. There are many more smaller sources of radiation and a multitude of complex physical processes in the ICM. One important process can be seen in Fig. 1.2.

If you look at the distribution of the components in Fig. 1.2, you can see that the DM are two separate ellipsoidally shaped clouds whereas the gas forms more of a cone-like structure and is located in between the two DM clouds. The reason for this differences can be explained if the clusters already flew through each other. The dark matter could keep its shape during a fly-through because it interacts with its surroundings significantly less than ordinary matter. The gas, however, being subject to hydrodynamical processes that create shock waves, was subsequently slowed down and is therefore still in the centre.

As we have seen, the bulk of the mass in a galaxy cluster is extended with a density

FIGURE 1.3: Composite image of NGC1275 the brightest cluster galaxy of the Perseus cluster. Hubble data from the Advanced Camera for Surveys covers visible-light wavelengths and is shown in the red, green and blue. Radio data from NRAO's Very Large Array at 0.91 m was also used. In this composite image, dust lanes, star-forming regions, hydrogen filaments, foreground stars, and background galaxies are contributions from the Hubble optical data. The X-ray data contributes to the soft but violet shells around the outside of the centre. The pinkish lobes toward the centre of the galaxy are from radio emission. The radio jets from the black hole fill the X-ray cavities. Chandra data from the ACIS covers X-ray wavelengths from 0.1771 to 4.133 nm (0.3-7 KeV). From: `https://spacetelescope.org/images/heic0817b/`

profile that can even reach infinity. Because there is no obvious 'edge' to a cluster, standard areas were defined for which the mass is then calculated. An example we will see later is M_{500}. This is the total mass confined to a region R_{500} where the density is 500 times higher than the critical density of the universe. The critical density marks the transition between an open and a closed universe and can be calculated from the Friedmann equations.

Cooling Flows

The ICM is constantly emitting high energy photons. This loss of energy is large enough to cool 10 to 1000 solar masses of X-ray emitting plasma every year (A. C. Fabian et al., 1974). Thus cooling flows have been postulated that can be derived from the assumptions about hydrodynamical conditions in the ICM. The details of the cooling process vary but in most models, parcels of cooling plasma collect at the centre of a cluster. The X-ray emission is proportional to the square of the central electron density. This leads to even more emission for clusters that already have high central electron densities. Additionally, the pressure of the overlying ICM should cause more gas to flow inwards once the gas in the core cools out. This positive feedback loop would eventually lead to a cooling catastrophe. Despite high central electron densities being indeed observed the classical cooling flow model has been ruled out by X-ray spectroscopic observations (Peterson and A. Fabian, 2006). If the cooling catastrophe cannot be observed there needs to be another process that heats the gas. Many possible mechanisms have been proposed (Li and Bryan, 2012), whereas feedback from active galactic nuclei is considered to be the most plausible (McNamara and Nulsen, 2007).

Fig. 1.3 shows a composite image of NGC1275. It can be seen that this galaxy shows interesting dynamics in X-ray, radio and optical light. Furthermore this BCG contains a super massive black hole and a cool core. One of the goals in this thesis is to find out if the presence of a cool core impacts star forming regions and therefore the stellar kinematics. In order to do this, the cool core has to be quantified.

Many cool core diagnostics exist for separating cool core and non-cool core clusters. This thesis is concerned with the central cooling time and the central entropy. The central region is defined as $0.00 < r < 0.048 R_{500}$ (Hudson et al., 2010). The cooling time t_{cool} is defined as the time the gas would need until all of its thermal energy is radiated away

$$t_{\text{cool}} = \frac{E_{\text{gas, thermal}}}{\epsilon^{ff}} \approx 8.5 \times 10^{10} yr (\frac{n_e}{10^{-3}\text{cm}^{-3}})^{-1} (\frac{T_g}{10^8 K})^{1/2}, \tag{1.1}$$

with the electron density n_e and gas temperature T_g. If the cooling time is smaller than the Hubble time, cooling effects due to the radiative losses become noticeable and the hydrostatic assumption is no longer valid (A. C. Fabian, 1994). Non-cool core clusters can be separated from cool core cluster with a cooling time of $t_{\text{cool, s}} = 7.7\text{Gyrs}$ (Hudson et al., 2010). The central entropy can be used to quantify the heating and cooling in a system. For the ICM it is defined as

$$K = n_e^{-2/3} T_g, \tag{1.2}$$

with the electron density n_e and gas temperature T_g. Hudson et al. (2010) set a threshold value of $K_0 = 150\text{keVcm}^2$. In the simulation, a quantity is used that is derived from these two properties. The coolcoreness is introduced in Hinz (2018) and will be described in detail in section 4.2.

1.1.2 Galaxies - A Colourful and Diverse Crowd

A kingdom is nothing without its people. If the kingdom is a galaxy cluster, well it is quite obvious that the people should be galaxies! We already got to know the king: the brightest cluster galaxy in the centre of a galaxy cluster. Actually we have already seen many galaxies in Fig. 1.2 and Fig. 1.3. They appear in different shapes and colours. Every galaxy is unique. In order to make sense of this beautiful mess people started categorising galaxies into digestible groups. The first person to categorise galaxies was Edwin Hubble who introduced classes according to the morphological structure of their stars (Hubble, 1926).

A schematic illustration of the Hubble sequence of galaxies can be seen in Fig. 1.4. Reading from left to right, there is first the class of elliptical galaxies. They are further separated by their degree of flatness or their ellipticity from spherically symmetric (0) to strongly ellipsoidal (7). Then he proposed a transition stage S0. These are called lenticular galaxies. From there, the galaxy can evolve into either S galaxies with a spherical central bulge or into SB galaxies with a central bar. They are further separated by the amount of unwinding of their spiral arms, from tightly wound (a)

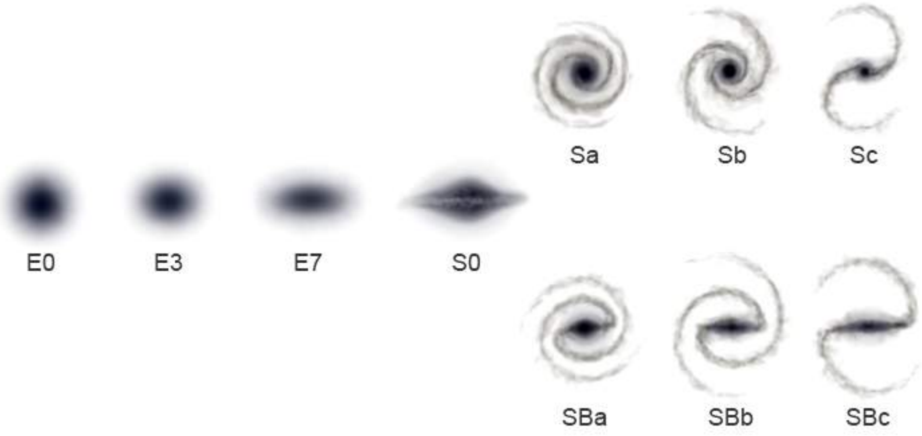

FIGURE 1.4: A schematic illustration of the Hubble sequence of galaxies. Wikimedia commons graphic, edited by the author.

to weakly wound (c). This diagram is also called Hubble's 'tuning fork' with the galaxies on the left being ETGs and the galaxies on the right being LTGs. As mentioned in the introduction of this chapter, the evolutionary aspect of this scheme is proven to be wrong e.g. (Ludwig Oser et al., 2010). If there are groups, there are always things that will just not match. This is not any different for Hubble's tuning fork. Some of the galaxies that do not belong to any of these classes are the most beautiful objects in our universe. NGC1275 looks like an elliptical galaxy at first glance. Its strong flows of cold gas reaching towards the centre, resembling peculiar spider-like structures, make it unique. According to the Morgan classification scheme, it belongs to the cD type of galaxies like many other brightest cluster galaxies.

The colour of a galaxy is determined by the colour of its stars and the surrounding gas. Much can be said about stellar properties and evolution but here is neither the time nor place to describe things like nuclear fusion or the stellar main sequence. In a galactic context, however, it is important to know that stars form in dense regions of relatively cool gas. Only then the gas cloud can collapse and form dense objects that will eventually start nuclear fusion. At z=2 (or roughly 3.5 billion years after the Big Bang) most galaxies contain a lot of gas. At this point they are able to cool the gas efficiently through radiation and form a lot of stars in their centres. This is observed as the cosmic peak of star formation (Moster, 2013). Stars that form within a galaxy are called in-situ stars. In-situ star formation is responsible for the blue colour of galaxies. During $2 > z > 1$ the observed star formation in galaxies decreases especially in more massive galaxies. Feedback mechanisms like stellar winds, growing black holes and dying stars start to feed a hot gaseous halo that hinders the gas inflow from cold streams. From this time on, galaxies start to grow mainly through mergers with other galaxies. The 'new' stars during this growth are stars from other galaxies. Because these stars did not form within the galaxy they are called ex-situ stars. If there is no ongoing star formation anymore the galaxies appear red. This is called the two-phase scenario of galaxy growth (Ludwig Oser et al., 2010). Galaxies are usually disk galaxies with spiral arms during the first phase that become elliptical galaxies through merging.

Very massive stars can turn into black holes. Black holes are objects so massive and so dense that even light is not fast enough to escape the gravitational pull if it comes too close (closer than the Schwarzschild radius). Every massive ETG is believed to exhibit a super massive black hole (**SMBH**) in its centre (Genzel and Eckart, 1999). If a black hole does not emit anything that is sucked in - how is it possible that it can heat the gaseous halo as stated above? Matter does not fall into the black hole in a straight line. It forms an accretion disk around the black hole. Because the accretion disk is a very dense cloud of gas and dust, friction starts to heat the disk. SMBHs with an active accretion disk are called active galactic nuclei (**AGN**). Feedback from AGNs can heat the gas in a galaxy tremendously through hot bubbles and jets.

As with galaxy clusters, the stars in galaxies are responsible for only a small fraction of the total mass. That there had to be some hidden mass became clear when the radial line-of-sight velocity profiles were observed in more detail. To make the understanding of stellar orbits in a galaxy a bit easier, let us have a quick look at our Solar System. The planets in our Solar System rotate once around the Sun in different times. This is obvious because they are on different orbits. On closer inspection, however, one finds that they also have different velocities on their orbits. The further out they are the more slowly they orbit around the sun. A galaxy is obviously quite different from a star. Entire books can be written about density profiles of galaxies. But most of its visible mass is also concentrated in the centre. One would expect that stars in the outskirts of a galaxy move more slowly. The observed velocity profiles, however, show that stars move roughly with the same speeds even if they are at different distances from the centre (Oort, 1940)! Again, this can be explained with an extended dark matter halo around the galaxy. Consequently the movement of the stars, i.e. stellar kinematics, contains information about the galaxy that we cannot observe directly.

We see that classifying galaxies based on their behaviour rather than classifying them based on their looks might be the more sensible approach. There are many different kinematical properties a galaxy can have and I will describe most of them in detail in Chapter 2. Generally ETGs and LTGs show different kinematics. Gas and stars of LTGs usually rotate fast and ordered around their centre in mostly circular orbits. Only their bulge components show random motion. The kinematics for disk galaxies that show bars and rings can be much more complicated. ETGs on the other hand seemed to have a rather modest diversity of stellar kinematics. Their ellipsoidal appearance is mostly supported by random motion with high velocity dispersion. The results of the Atlas3D survey (Cappellari, Emsellem, Krajnović, et al., 2011), however, showed that ETGs show a wide variety of rotation patterns in their centres.

1.1.3 A Never Ending Dance

BCGs are special ETGs with very high mass and a rich merger history that are exposed to a unique cluster environment. It will be interesting to see which kinematical features they show and how they compare to ETGs in other parts of a cluster. In order to understand a bit better where eventual differences might come from, we have to have a little bit of a closer look at what happens when a galaxy interacts with other galaxies or parts of the galaxy cluster. Information in this section is based on Remus (2015).

As mentioned above, the most important mechanism for galaxy growth, especially for BCGs, is galaxy merging. If there is an encounter with two or more galaxies where the differences in orbital energy and angular momentum are low enough, they will eventually merge. The merging process is finished when the orbital energy between the encountering galaxies is transferred to the internal energy of the newly formed system. Thus, the lower these differences are, the quicker they merge.

The morphological and kinematical properties of the resulting galaxy strongly depend on the mass ratio between the two progenitor galaxies. Usually the BCG is much more heavy than the galaxies it merges with. If the mass ratio is below 1:3, the type of merging is called a minor merger. Minor mergers can hardly alter the morphological and kinematical properties of the BCG. However, being in the most active region of the galaxy cluster, BCGs are likely to experience a lot of consecutive minor mergers. This does indeed have an impact on the BCG. Especially because the stars of the smaller galaxy are usually already ripped away in the outer region and are therefore the main contributor of stars in the outer region, i.e. the intra cluster light (**ICL**).

A major merger describes the merging event of galaxies with a mass fraction larger than 1:3. In this case, the properties of the resulting galaxy depend on the properties of both progenitor galaxies and the orbit of the encounter. There are only few to no instances of major merger events for BCGs between $2 > z > 0$ but if they happen they have a significant impact on the BCG. This impact also differs greatly if there is gas (wet merger). If gas is accreted through mergers with gas-rich galaxies the star formation in the BCG can be fuelled. However, most of the galaxies in a galaxy cluster, and especially the BCG, lost most of their gas a long time ago.

There are more effects that can happen between a BCG and surrounding galaxies - especially if they have gas. They have usually a strong impact on the merging satellite galaxy but a tiny effect on the BCG. Therefore, star bursts, strangulation, harassment, ram-pressure stripping etc. will not be discussed here. A final noteworthy effect is tidal stripping. If a galaxy passes the BCG with a close distance, the galaxy or parts of it might be torn apart. This does not have an impact of the BCG itself but the stripped stars contribute to the ICL.

There is much more that can be said about galaxies and galaxy clusters. I think, however, that this background is enough to understand the introduction of the kinematical properties and the conclusions derived from their evolution - with one major exception. The BCGs in this thesis are numerical representations of brightest cluster galaxies in our real universe. Albeit originating from a fully cosmological context, there are fundamental differences that have to be kept in mind. The next section will give a short introduction to the benefits and drawbacks of cosmological computer simulations and serve as an overview of the technical specifications of the simulation used in this thesis.

1.2 A Whole Universe Inside a Box

Computer simulations are a backbone of modern astrophysics and have driven major advances in the understanding of our universe. This is because they open up new dimensions for the investigation of astrophysical processes - quite literally. In a computer simulation, all coordinates of the position of a particle i (x^i, y^i, z^i), the velocity (v^i_x, v^i_y, v^i_z) and its mass m_i are known for every time step t. As illustrated with the example of a theatre screen in the introduction of this chapter, observers have to work with much less information. They only see the x-component and the y-component of an object. They measure different luminosities L for objects that are further away but their luminosities often depend on much more than just the distance of that object. Distance measuring is a very complex subject that is often accompanied with large errors. Because galactic processes happen on unimaginable long timescales it seems like galactic objects are frozen in time. This makes the observation of the evolution of individual galaxies impossible. Although individual objects can move with enormous velocities (hundreds of kilometres per second) the distance they travel in observable time frames is undetectable. Their line of sight velocity v_z, however, can be measured with a trick. If an object is moving away from an observer its light is shifted to lower frequencies just like an ambulance sounds lower when it is driving away from you. It is important to note that this is a different effect than the cosmological redshift that was introduced at the beginning of this chapter.

If there are so many more observables for simulated galaxies why do we even keep looking at the real ones? Simulated objects only follow the physical prescriptions that we attribute to them. But space is governed by fundamental physical laws that we might never be able to understand in their entire beauty. Every physical prescription that we formulate is an approximation based on assumptions and/or observations. With every iteration, however, we come one step closer to an adequate description of truth. Gravity, for example, is relatively well understood. The earliest simulations of the cosmos were dark matter only simulations (Springel, S. D. M. White, et al., 2005). These were able to reproduce many features we can observe and helped constraining the cosmological parameters. With ordinary matter, things become much more complicated. There are feedback processes and physics that happen on small scales. And this is where every simulation hits a boundary: resolution. Because the memory of every computer is limited, there has to be a limit on the number of discretization elements that make up the virtual cosmos. The discretization elements in the simulation used for this thesis are particles. Since cosmological simulations want to reproduce known densities, this resolution limit is given by a minimum mass for each particle. Particles are points in space with different properties. Dark matter particles, for example, only interact gravitationally. There are also stellar particles that interact with each other and gas particles in various ways. These stellar particles usually have masses that are orders of magnitudes larger than their real-life counterparts: stars. Therefore a stellar particle represents a whole bunch of stars that are confined to a single point in space. While this seems very different from the truth on small scales, it is a good approximation for galaxies that can contain thousands of stellar particles.

Every simulation is described by some key features. First box size and the number of particles. The higher the box size the stronger is the cosmological context. The higher the number of particles the smaller the minimum mass. This means a higher resolution. The simulation I use for my thesis is the high resolution version of Box 2 of the MAGNETICUM Pathfinder-Simulation set. It contains 2×1584^3 particles in a volume of $(352\text{Mpc}/h)^3$. This results in a mass for dark matter particles of $6.9 \times 10^8 M_\odot/h$ and gas particles with a mass of $1.4 \times 10^8 M_\odot/h$. The heart of each simulation are the algorithms that compute the interaction between particles. The way they work and how they differ is a whole topic in and of itself and will not be described here. But note that there are specific algorithms for the calculation of gravity and hydrodynamics (properties like gas temperature and pressure). This simulation uses a tree/particle mesh (TreePM) code to calculate gravity. The hydrodynamics are calculated with with an extended version of the SPH-Code GADGET-2 (Springel, 2005) called P-GADGET-3. Then there are different processes that are modelled semi-analytically or empirically because the necessary resolution is not high enough. Such models included in the MAGNETICUM simulation are: Cooling, star formation and stellar winds following Springel and Hernquist (2003). Metals, stellar populations and chemical enrichment according to Tornatore et al. (2003). Black holes and AGN feedback are modelled according to Fabjan et al. (2010) with various improvements by Hirschmann et al. (2014). Thermal conduction further described in K. Dolag, Jubelgas, et al. (2004). A low viscosity scheme is implemented to track turbulences (K. Dolag, Vazza, et al., 2005) with improvements from Beck et al. (2015). Finally, magnetic fields are implemented according to K. Dolag and Stasyszyn (2009). Halos and subhalos are identified using the SubFind algorithm (K. Dolag, Borgani, et al., 2009). The MAGNETICUM pathfinder simulations use a WMAP7 cosmology taken from Komatsu et al., 2010, with the cosmological parameters $\Omega_0 = 0.272$, $\Omega_\Lambda = 0.728$, and $H_0 = 70.4$.

Chapter 2

Parodos: Kinematical Properties

Given the background information provided in the previous chapter it is now possible to focus on the BCGs of BOX 4 in the MAGNETICUM simulation. I divide my research into two parts. The first part leaves the time dimension out of the discussion. All properties are investigated at present time, i.e. redshift zero (z=0). These results will be compared with observational data which themselves only exist for a specific galaxy at one specific redshift. After we convinced ourselves that the simulated BCGs are indeed good toy models for real BCGs (at least at z=0), their evolution through time will be set in relation to the evolution of environmental properties in part two. It is likely that properties do not evolve in parallel but instead influence each other on different time scales. Furthermore, they could not even depend on absolute values but on their respective changes over time. Therefore, the time dimension is essential for that part of the analysis.

In the following I will use terms that need a bit of explanation to be precise. Concerning observations, I will frequently use the words *galaxy cluster* and *galaxy* as described in Chapter 1. The simulation analogues are *halo* and *subhalo* respectively. I use the term BCG for both observations and simulations. In my case a BCG is the first subhalo of a parent halo with a virial mass of $M_{\mathrm{vir}} > 10^{14} M_{\odot}$. The first subhalo is connected to the main overdensity from which local overdensities lead to the construction of additional subhalos. This mass threshold for the parent halo is chosen to differentiate between BCGs and centrals of groups. I only consider subhalos at all if they have a stellar mass of $M_{*} > 5 \times 10^{11} M_{\odot}$ which is a reasonable minimum mass for BCGs. These masses and many of the following properties are calculated by SubFind on-the-fly (K. Dolag, Borgani, et al., 2009). It is important to note that for BCGs this is the total stellar mass (ICL+BCG). When talking about stellar mass in this and the following chapter this is the referred mass unless stated differently. We will see later that the minimum mass of our classified sample lies well above this threshold.

2.1 The Brightest Cluster Galaxies of the Simulation

Mass and number density of galaxy clusters are global properties with central importance to cosmology because the halo mass function is dependent on cosmological parameters. Since this link is established the relation between halos and subhalos can be tested.

First, the subhalo-halo mass relationship is investigated. It is obvious that a more massive halo should inhibit a more massive BCG. For a good agreement with observations, the slope should be well fit as well.

On the left side of Fig. 2.1 the relationship between M_{500} and M_{*} is shown with M_{*} being the stellar mass within an aperture of $0.05 \times R_{500}$. This includes the BCG

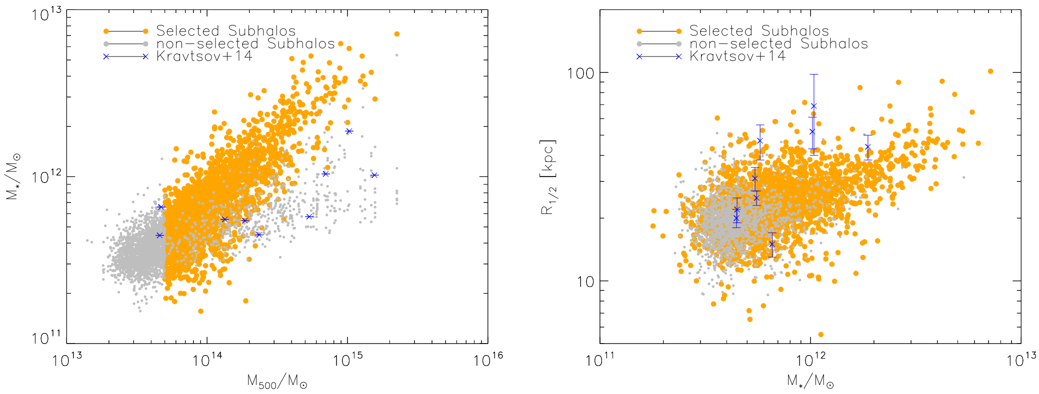

FIGURE 2.1: Stellar mass in an aperture of $0.05 \times R_{500}$ of subhalos in relation to other properties compared with observational data taken from Kravtsov, Vikhlinin, and Meshcheryakov (2014). **Left:** The sub mass-halo mass relationship, **right:** Mass-Size relation.

and stellar light from the halo without contamination from other subhalos in that aperture. Modelling the BCG and its outer regions (the ICL) separately is difficult in practice therefore this combination makes for the easiest comparison. The aperture is chosen to be very small because this has the lowest error in the observation. According to (Kravtsov, Vikhlinin, and Meshcheryakov, 2014) the magnitude of the errors is so small that they did not quote them in their work. Selected BCGs are coloured in orange and non-selected subhalos in light grey. BCGs fulfil the criteria described above and non-selected subhalos only have the minimum stellar mass. The border between satellites and BCGs at $M_{500} > 0.5 \times 10^{14} M_\odot$ seems arbitrary. However, this border had to be placed somewhere because the first subhalo of a halo is not always guaranteed to be a BCG. For low masses it could also be a central of a galaxy group or just an isolated galaxy. By ensuring that the parent halo of a minimum mass of $M_{\text{vir}} = 10^{14} M_\odot$ these cases are unlikely. Note how there is scatter below the orange cloud. These are the very massive satellites of the more massive halos. The observational data taken from Kravtsov, Vikhlinin, and Meshcheryakov (2014) is shown in blue ticks. For lower halo masses the masses of the simulated BCGs fit the observations quite well. For higher halo masses the BCG masses are roughly a factor of 2 higher than their observational counterparts. In other words the slope of the relation is overestimated slightly in the simulation. The non-selected subhalos with halo masses $M_{\text{vir}} > 10^{14} M_\odot$ are usually massive satellite companions of BCGs. It can be seen that those follow the trend in the observations more closely.

On the right hand side the mass size relation is displayed. In order to calculate the stellar half mass radius all stars within 10% of the virial radius of the halo are selected. Now these particles are sorted by their distance to the centre of the cluster. By summing up all the masses of stellar particles in this order a point will be reached where this sum equals half of the total stellar mass in that region. The half mass radius is the distance to the centre of the first particle after which the sum would exceed half the total stellar mass.

$$R_{1/2} = |\mathbf{x}_0 - \mathbf{x}_i| \tag{2.1}$$

with i such that

$$|\mathbf{x}_0 - \mathbf{x}_i| < |\mathbf{x}_0 - \mathbf{x}_{i+1}| \text{ and } M = \sum_i m_i \geq M_*/2, \tag{2.2}$$

where $\mathbf{x}_i$ is the three dimensional position of particle i and m_i is the stellar mass of particle i. Kravtsov, Vikhlinin, and Meshcheryakov (2014) calculate the half mass radii with a three-component Sérsic fit to the stellar surface density profiles and measure the projected radius containing half of the total stellar mass measured by extrapolating the best fit three-component fit to infinity. The effective radius is then converted into the 3D half-mass radius using $R_{1/2} = 1.34R_e$.

All observational data lies within the range spanned by the simulated BCGs. The relation becomes even more similar by remembering that high stellar masses are overestimated by roughly a factor of 2.

It can be concluded that although the masses of the simulated BCGs are a bit overestimated in the high-mass regime their internal structure, as far as the half-mass radius goes, resembles observations very well. Thus making the simulated BCGs good models for further investigation. Especially since they all emerged from a fully cosmological context.

2.2 Velocity Maps

As described in section 1.2, the power of simulations is to have three dimensional data. However, in order to compare with observations the data has to be projected onto 2D-maps. There are many properties that can be displayed in maps, e.g. temperature, density or luminosity. These are all statistical properties of a large sample of particles. The maps relevant for my thesis display kinematical information. Every particle in the simulation has three dimensional velocities. These velocities have to be projected and combined in a statistically useful way. The construction of velocity maps and calculation of many properties presented here is based on work done by Felix Schulze (F. Schulze et al., 2018).

2.2.1 Construction

Preparing Particles

The velocities displayed in this thesis are selected in the following way. First every stellar particle within $0.1R_{\text{vir}}$ that belongs to the first subhalo of the halo is selected. This means there is non-negligible contribution of the intra-cluster light (**ICL**) since particles that cannot be associated with smaller subhalos are associated with the central subhalo by construction. Then the stars are rotated edge-on in the sense that the inertia matrix of the stars is diagonalized. Turning all subhalos edge-on introduces a selection bias that has to be kept in mind when comparing to observations. However this makes it easier to compare subhalos from the same simulation. The major axis lies on the x-axis. Following that the positions of the stars are shifted into the centre of mass frame and the velocities of the stars are shifted into the centre of momentum frame. This sets the peculiar motion to zero.

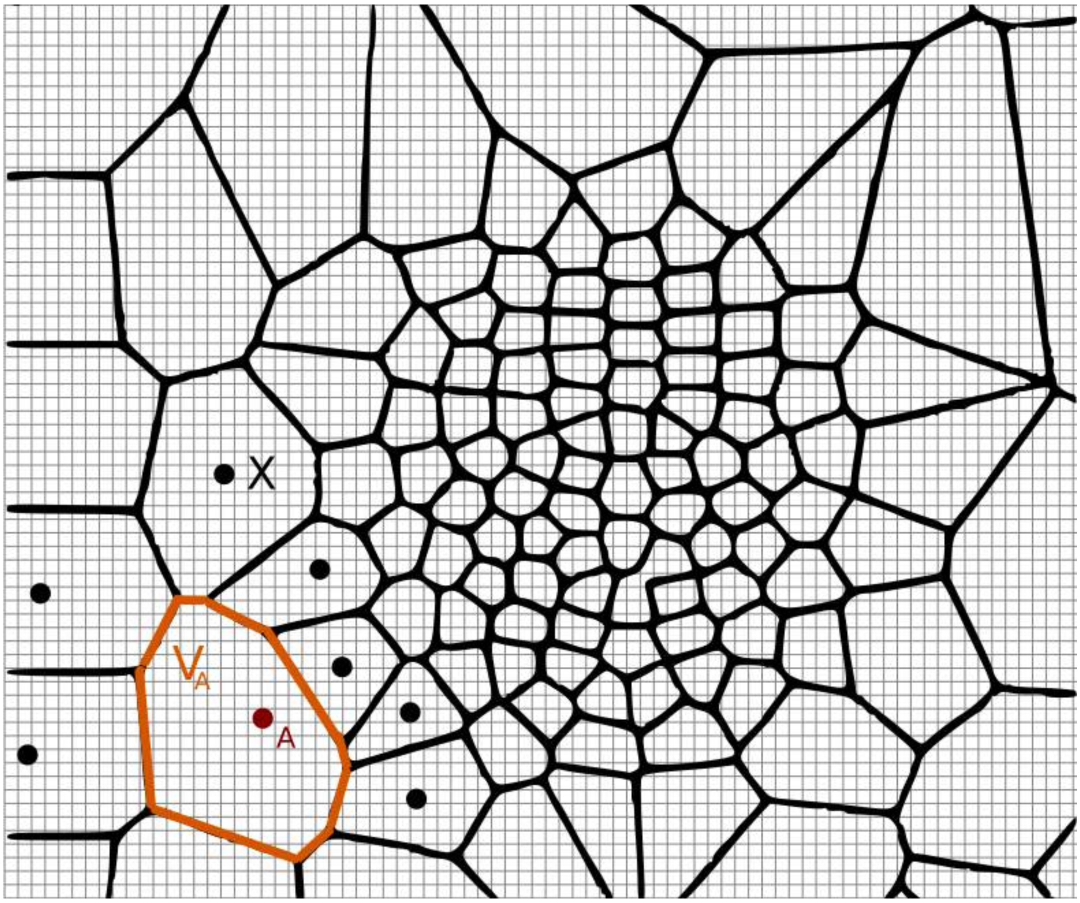

FIGURE 2.2: Schematic for Voronoi cells constructed by individual pixels

Combining Particles

There are three layers of abstraction introduced by combining different particles together. The bottom layer are the individual particles in a box with height and width of one stellar half mass radius $R_{1/2}$ and a depth of $0.1R_{\mathrm{vir}}$. The depth of the box is chosen this way because it is impossible for observers to differentiate the LoS-coordinates of stars within one galaxy. The second layer of abstraction is a grid with 200×200 pixels. Each individual pixel has therefore a height and a width of $0.005R_{1/2}$ and a depth of $0.1R_{\mathrm{vir}}$. Stars are combined in pixels because statistical motions are of interest and not individual motions. However the density, i.e. resolution, in the central region is much higher than in the outskirts. To keep the signal to noise ratio constant in each area a third layer of abstraction is introduced. Different pixels are combined into Voronoi cells. Following the density, virtual points are put into the plane. Every pixel that is closer to point A than to any other point X is combined to a Voronoi cell V_A. This procedure is schematically displayed in Fig. 2.2. Now the pixels have been combined into meaningful groups and it is possible to perform calculations on them. From here on I call Voronoi cells *cells* and grid pixels *pixels*.

Fitting Particles

The line of sight velocities of the stars within a cell are distributed randomly around a mean value. This distribution is assumed to be Gaussian with a specific skewness and kurtosis. Since every cell is the sum of several pixels this assumption is backed up by the central limit theorem. The random variable is the line of sight velocity v and the sample size is the number of stars in each cell. The moments of the distribution μ, σ, h_3 and h_4 describe the kinematics of the stars in one cell and are acquired by fitting the data with a Gaussian distribution that is extended with Hermite polynomials

$$L(w) = \frac{1}{\sqrt{2\pi\sigma}} \exp[-0.5w^2(1 + \sum_{i=3}^{n} h_i H_i(w))], \tag{2.3}$$

with $w = (v - \mu)/\sigma$ and where

$$\begin{aligned} H_3(w) &= \frac{1}{\sqrt{6}}(2\sqrt{2}w^3 - 3\sqrt{2}w), \\ H_4(w) &= \frac{1}{\sqrt{24}}(4y^4 - 12y^2 + 3). \end{aligned}$$

A detailed explanation of higher order moments can be found in van der Marel and Franx (1993). How the higher order moments h_3 and h_4 affect the line-of-sight velocity distribution (**LOSVD**) is displayed in Fig. 2.3. Generally, an arbitrarily extended Gaussian can be described with n moments. We use $n \leq 4$ and Fig. 2.4 illustrates why. Displayed is a bootstrapping of the four fitting parameters. Each colour represents a different Voronoi cell. The five Voronoi cells lie next to each other and are for this purpose comprised of 400 particles. An increasing number of particles is randomly drawn within each bin and the fitting parameters are determined. Each number of particles is drawn 150 times. The arithmetic mean of the resulting fitting parameter is displayed on the y-axis. As can be seen the statistical error decreases with increasing number of drawn particles.

FIGURE 2.3: The extended gaussian distribution for several values of h_3 and h_4. The curves in the left panel have $h_4 = 0$ and demonstrate the effect of nonzero h_3. The peak of the distribution occurs at negative v for $h_3 > 0$ and vice versa. The right panel shows curves with $h_3 = 0$ and demonstrate the effect of nonzero h_4. The extended gaussian is more centrally peaked than a standard Gaussian with $h_4 > 0$ and more flat-topped than a standard Gaussian for $h_4 < 0$. This is Fig. 1 in (van der Marel and Franx, 1993).

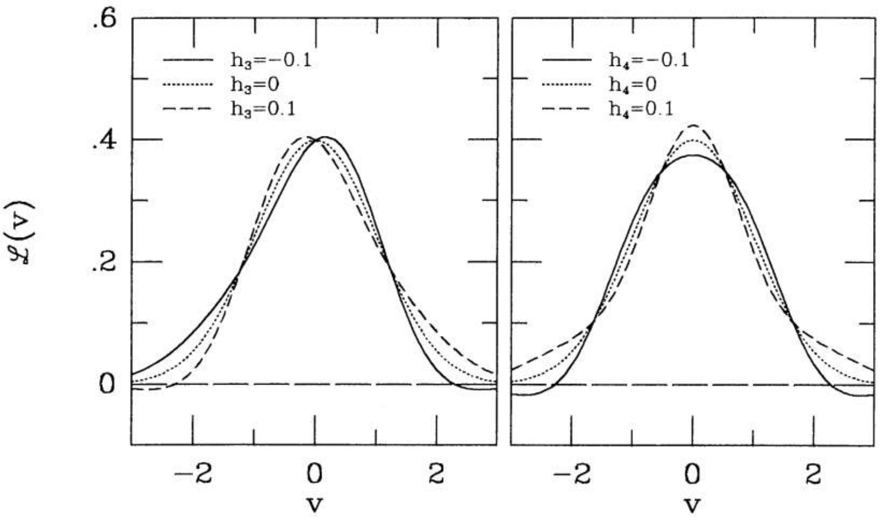

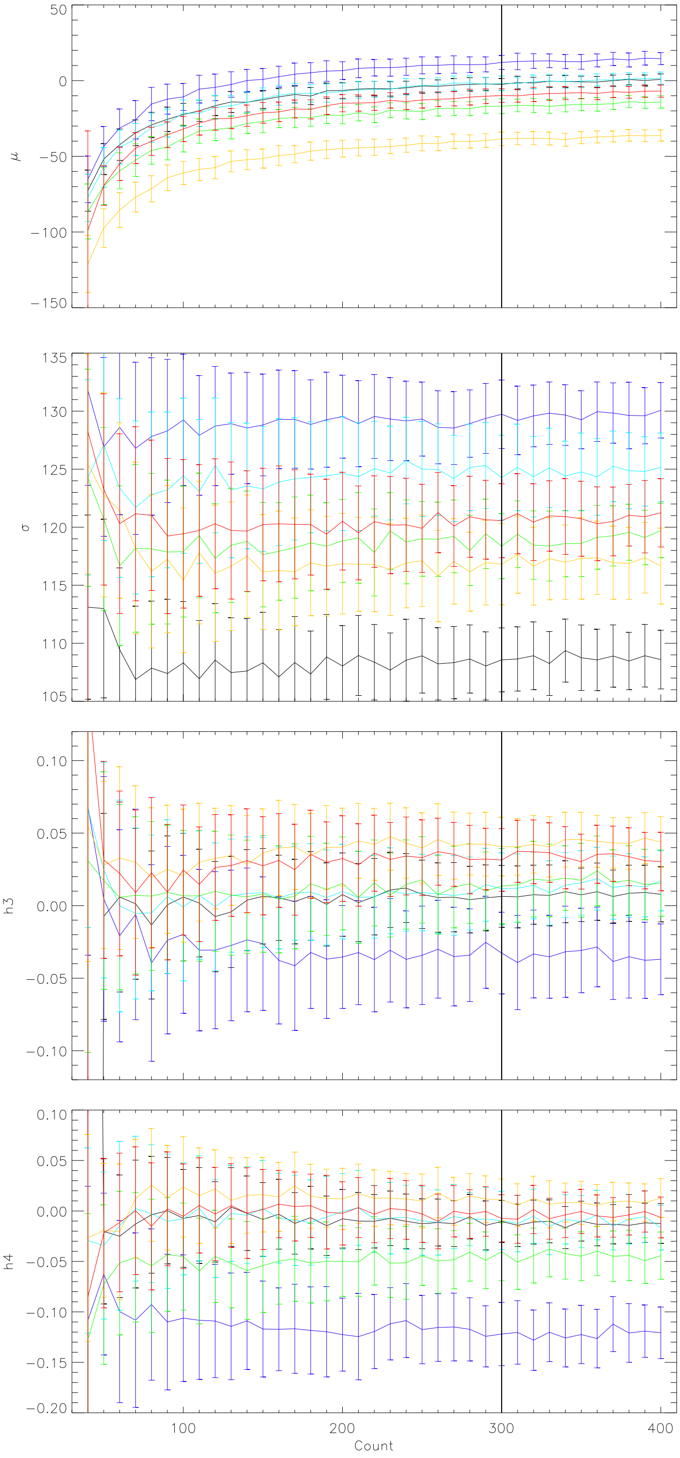

FIGURE 2.4: Bootstrapping of the four fitting parameters: mean velocity μ, standard deviation σ and higher moments h3 and h4. Each colour represents one of six neighbouring Voronoi cells which consist of 400 particles. The number of drawn particles is displayed on the x-axis. Each number of particles is drawn 150 times and the respective mean fitting parameter is displayed on the y-axis. The error bars represent the statistical standard deviation for each number of drawn particles. The solid black lines indicates the number of particles we chose in order to resolve the moments of the distribution.

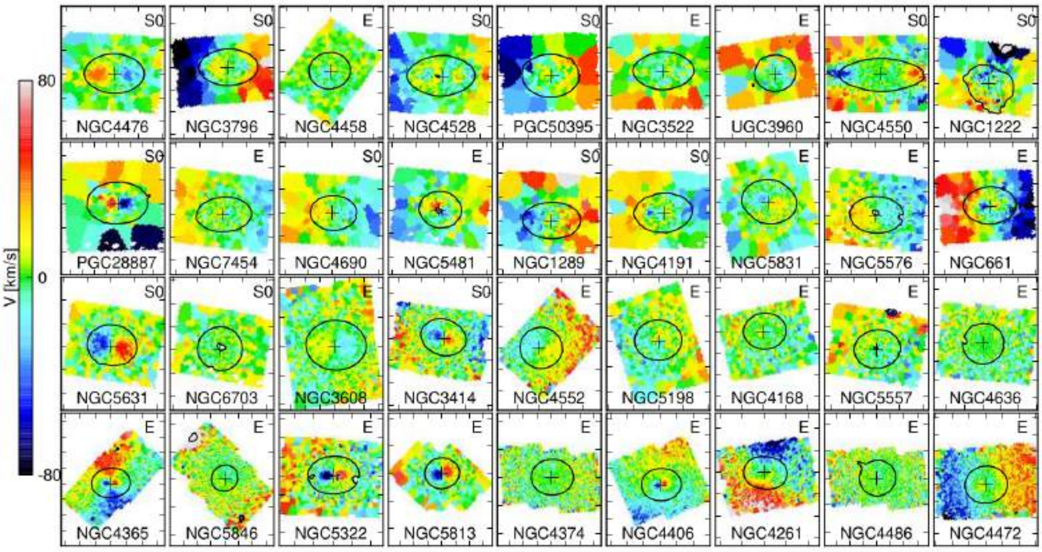

FIGURE 2.5: Stellar velocity fields for 36 ETG slow rotators in the ATLAS 3D sample taken from Emsellem, Cappellari, Krajnović, et al. (2011). The solid black contour correspond to a representative isophote and the centre of the galaxy is indicated by a cross. From top to bottom, left to right, the order follows the (increasing) dynamical mass values. The names of the galaxies and their Hubble types (E or S0) are also indicated.

In short, the problem is one of resolution. Resolution of the map, i.e. more cells, comes at a cost of resolution of each Voronoi cell. But for the map to be meaningful at all each cell has to be resolved. This is the case when it is possible to properly distinguish neighbouring cells, i.e. the values of neighbouring cells differ by at least one standard deviation. Lower order moments are much more constrained than higher order moments. While μ and σ are separated at around 150 particles per cell, h_3 and h_4 are reasonably well separated at 300 particles per pixel. Hence a minimum particle number of $N_{\mathrm{min}} = 300$ is set for all cells.

The higher order moments depend on the stellar orbits of a galaxy and are difficult to interpret. Some interpretations connect the presence of a stellar disk in early-type galaxies with asymmetric line profiles (van der Marel and Franx, 1993). Especially for fast rotating galaxies a strong anti-correlation between h_3 and V/σ has been observed (Bender, Saglia, and Gerhard, 1994). The origin is attributed to z-tube orbits in Röttgers, Naab, and Ludwig Oser (2014). h_4 is an indicator of radial anisotropy if it is positive or tangential anisotropy if it is decreased (Gerhard (1993), van der Marel and Franx (1993)). A bar or disk regrowth in bulges can lead to more complex signatures in h_3 and h_4 (Bureau and Athanassoula (2005), Naab and Burkert (2001)).

2.2.2 Rotational Patterns

The dynamical structure of a galaxy can now be illustrated by colouring each cell according to their mean LoS-velocity. Receding movement is colour coded in red and approaching movement is colour coded in blue. An example of this can be seen in Fig. 2.5. For easier comparison, the outer photometric axis was used to align all galaxies horizontally. Some galaxies show rotating centres with no rotation in the outskirts, others show fast rotation far outside the representative isophote and others do not show significant rotation at all. Furthermore, we see that the Hubble types

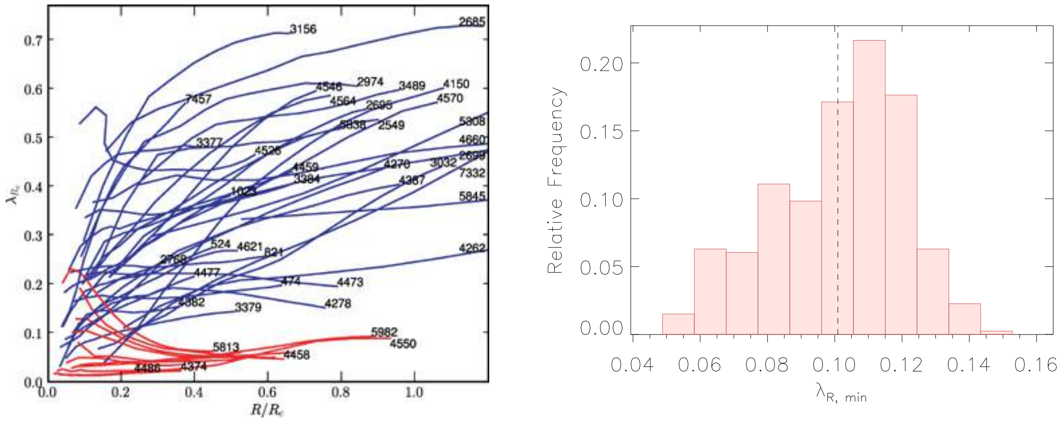

(A) Radial λ_R profiles for fast rotators (blue) and slow rotators (red).

(B) Histogram of minimum values of λ_R. The mean value is marked with a dashed line.

FIGURE 2.6: λ_R properties.

cannot be used as a proxy for kinematics. Some galaxies of type E show rotation while others do not and the same for galaxies of type S0. Another classification scheme has to be introduced.

2.2.3 Global Properties

The simplest classification scheme is one with two different classes based on one single number. This can be achieved with the angular momentum proxy.

Angular Momentum Proxy

General interest lies in quantifying the relative amount of stellar rotation in a system. This is can be achieved by calculating $\langle |V| \rangle / \sigma$. If the fraction is large then ordered motion is high compared to random motion, effectively describing the dynamical state of ETGs. To investigate the difference between large scale and small scale rotation, however, there is another parameter that takes the global velocity structure into account (Emsellem, Cappellari, Peletier, et al., 2004). This is the angular momentum proxy

$$\lambda_R = \frac{\langle R|V| \rangle_w}{\langle R\sqrt{V^2 + \sigma^2} \rangle_w}, \tag{2.4}$$

where R is the projected radius, V the line-of-sight velocity and σ the projected velocity dispersion. w denotes that this is a weighted average. Observations weigh with fluxes. In simulations, these are replaced with stellar masses, assuming a constant mass-to-light ratio within each galaxy. In practice the formula transforms into

$$\lambda_R = \frac{\sum_{i=1}^{N_c} M_i R_i |\overline{V_i}|}{\sum_{i=1}^{N_c} M_i R_i \sqrt{\overline{V_i}^2 + \sigma_i{}^2}}, \tag{2.5}$$

where N_c is the total number of Voronoi cells described above. This reduces artificial statistical noise to a minimum. The mean projected velocity $\overline{V_i}$ and projected velocity dispersion σ_i are obtained by the fitting routine in every cell as described in section 2.2.1. λ_R takes values between 0 and 1. For a purely rotational supported system, λ_R tends to unity and for a dispersion dominated system, λ_R tends to zero. Furthermore, λ_R can be used to distinguish between patterns of rotation. The first

pattern is low rotation in outer regions. No matter if they have high rotation in the cores or not they usually have $\lambda_R < 0.1$. For $\lambda_R > 0.1$ galaxies have high rotation in outer regions. Fig. 2.6a illustrates this behaviour well. From here on, galaxies of the first class will be called slow rotators and galaxies of the second class will be called fast rotators. In Fig. 2.6a slow rotators are coloured in red and fast rotators are coloured in blue. It can be seen that despite some slow rotators having high central rotation, they have decreasing profiles and by definition a total $\lambda_R < 0.1$. Fast rotators can have low central rotation but are always mildly to very fast rotating in the outer regions (Emsellem, Cappellari, Krajnović, et al. (2011)). Slow and fast rotating galaxies have very different dynamical properties, which suggests that there are at least two formation paths for creating the two kinematic classes in early-type galaxies (Naab, L. Oser, et al., 2014). van de Sande et al. (2017) suggest that the formation history is even more complex and cannot be divided into two paths because of different behaviour in the higher order moments.
Regarding this thesis it is important to note that for slowly rotating systems the bias introduced by the resolution limit is substantial. Assuming all velocities to be zero such that $v + \Delta v = \sigma/\sqrt{N}$ there is always $\lambda_{R,\mathrm{min}} > 0$. A histogram of $\lambda_{R,\mathrm{min}}$ for the 397 classified BCGs (the process of classification is described in 2.3) is displayed in Fig. 2.6b. It can be seen that $\lambda_{R,\mathrm{min}}$ takes values between 0.05 and 0.15 with a mean of $\overline{\lambda}_{R,\mathrm{min}} = 0.10$. Therefore it is impossible for most simulated BCGs in my sample to be below the slow rotator line just because of numerical noise. A more sophisticated way of dividing these two groups is described in Emsellem, Cappellari, Krajnović, et al. (2007). Generally, λ_R depends on the shape of the galaxy. This brings us to our first global morphological parameter, the ellipticity ϵ.

Ellipticity

Generally, the ellipticity ϵ of an object is given by $\epsilon = 1 - b/a$ where a denotes the semi-major and b denotes the semi-minor axis. The ellipticity is calculated within a given aperture and is dependent on that aperture. Therefore an iterative approach is taken to calculate the ellipticity in this thesis following Cappellari, Emsellem, Bacon, et al. (2007). Beginning with the calculation of ϵ_0 within a circular aperture with a diameter of $2R_{1/2}$, the aperture is refined 15 times. Each time this aperture is an ellipse with ϵ_{n-1} scaled such that it contains the same mass as before. Since higher ellipticities are found in more extreme objects a scaling between λ_R and ϵ is expected. In order to take this scaling into account, the slow rotator - fast rotator - line is defined as

$$\lambda_R = 0.31\sqrt{\epsilon}. \tag{2.6}$$

The ellipticity is a morphological parameter that is mainly used for ETGs since the ellipticity of LTGs is extremely dependent on the viewing angle. A disk can seem round if viewed face-on and like a line if it is turned edge-on. Since all of our selected BCGs are expected to be ETGs because of their high mass and the large amount of mergers, they experience in the centre of a galaxy cluster this is not of too much concern. But how can we back up our intuition with quantitative data?

b-Value

We already saw that the origin of ETGs and LTGs goes back to the Hubble sequence. Therefore, we could investigate all galaxies individually and classify them. This is tedious and introduces human bias. Fall (1983) introduced a model that predicts that galaxies follow a 2D surface in a 3D space of specific angular momentum $\log j_*$,

stellar mass log M_* and bulge fraction β_*. Disks and bulges follow separate scaling relations of the form $j_* \propto M_*^\alpha$ with $\alpha = 0.67 \pm 0.07$ but offset from each other with a factor of 8 ± 2. This suggests that the distribution of galaxies with different β_* in the $M_* - j_*$ Plane is a physically based alternative to the Hubble sequence.
In order to effectively parametrise the position of a galaxy in the $M_* - j_*$ Plane Teklu et al. (2015) introduced the b-value which is defined as

$$b = \log(\frac{j*}{\text{kpc km/s}}) - \frac{2}{3}\log(M_*/M_\odot) \tag{2.7}$$

with

$$j_* = \frac{|\sum_{j=1}^{N} m_i \mathbf{r}_i \times \mathbf{v}_i|}{\sum_{j=1}^{N} m_i}. \tag{2.8}$$

The b-value parametrises the offset between bulges and disks. Teklu et al. (2015) showed that at z=0 objects with $b \approx -4$ are disc-like galaxies, followed by a smooth transition to elliptical galaxies with decreasing b-value.

Mean Higher Order Moments

To describe the anisotropy of the velocity field of the whole galaxy, the mean higher order moments $\overline{h_3}$ and $\overline{h_4}$ can be used. They are derived by fitting every particle of one subhalo within $2R_{1/2}$ with the extended Gaussian (Eqn. 2.3). This makes this in a sense a luminosity weighted average because there are more particles in the centre than in the outskirts. Note that this is different than averaging the h_3 and h_4 values for every cell.

2.3 Classification

As we have seen in Section 2.2.2, velocity maps carry much more information than what could be expressed in one number. Although λ_R takes different values depending on how the system is supported by ordered motion, there is still ambiguity. A regular rotator could have the same λ_R as a prolate rotator even though they might have very different formation histories. Therefore, it makes sense to classify them individually based directly on what pattern we see in the velocity maps.

For our classification we distinguished between four different groups: non-rotator, regular rotators, prolate rotators and distinct cores. Examples for each can be seen in Fig. 2.7. Non-rotators (**NR**) are characterised by overall low velocities and no apparent velocity structure. Regular rotators (**RR**) feature a rotational supported velocity structure around the minor axis out to one $R_{1/2}$ and farther. Their velocities are on average among the highest in all four classes. Prolate rotators (**PR**) are similar to regular rotators but instead rotate around the major axis and generally have lower velocities. The last class, the distinct cores (**DC**), show strong rotation within the centre but low to no rotation in the outskirts. Some maps show a combination of different structures. If the rotational axis is tilted and cannot be categorised as either a regular rotator or a prolate rotator, a lowercase t is added. If for example a distinct core rotates around the major axis a lower case p is added. For simplicity these additions were dropped later on. We applied these criteria while classifying the 650 most massive subhalos. The procedure was as follows: All subhalos were sorted by mass. In order to minimise human bias, four of us classified 650 subhalos each on their own. Subhalos with smaller stellar masses did not have enough resolution to

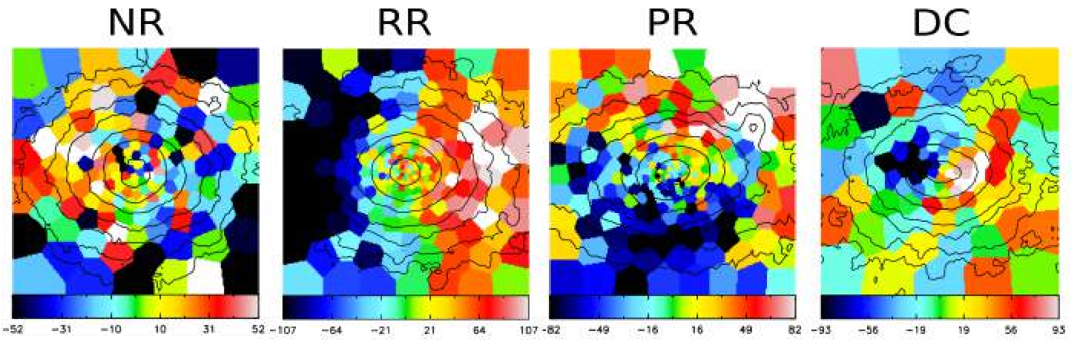

FIGURE 2.7: Examples for each kinematical group based on their velocity structure. Each panel measures $2R_{1/2} \times 2R_{1/2}$. Minimum and Maximum velocities are indicated on the colour bar below. The contour lines mark the area where (from inner to outer) 30%, 50%, 70%, 80%, 90%, 95% and 99% of particles are contained. All galaxies are seen edge-on with their major axis on the x-axis.

make any useful estimates. Following that each subhalo was put in the group where most agreed with each other. When there were two votes for class A and two votes for class B the subhalo was marked as unclassifiable. For some galaxies everyone agreed that this map is not classifiable, e.g. with clear signs of mergers. From the 650 galaxies 253 were either marked as unclassifiable or were non-selected subhalos leaving us with 397 BCGs to study their internal velocity structures.

Chapter 3

Parodos: Stellar Kinematics at Redshift Zero

3.1 Classification

The velocity maps of the 48 most massive BCGs and their respective classifications are displayed in Fig. 3.2. It is obvious that even for the most massive BCGs, the resolution is much lower than the resolution for subhalos in BOX 4 of the MAGNETICUM simulation (Felix Schulze, Remus, and Klaus Dolag, 2017). Nonetheless it was possible to classify most of them.

The results are displayed in Fig. 3.1. It can be seen that the non-rotators comprise the largest fraction of galaxies with 69% followed by regular rotators with 18% and there is only a minor fraction of prolate rotators (8%) and distinct cores (5%). Total stellar masses range from $\log M_*/M_\odot = 12.3$ to $\log M_*/M_\odot = 13.25$ with the heaviest classified BCG being a prolate rotator. This is significantly different to the classification of the subhalos in F. Schulze et al. (2018). There the largest fraction was that of the regular rotators with 69% followed by a non-rotator fraction of 14%. It is important to note, however, that the masses of these subhalos are significantly lower, starting at around $\log M_*/M_\odot = 10.3$ and barely reaching $\log M_*/M_\odot = 12.0$. This difference is part due to the contribution of the ICL for this sample of BCGs.

FIGURE 3.1: Pie Chart that displays the different fractions of kinematical groups in our sample of 397 BCGs.

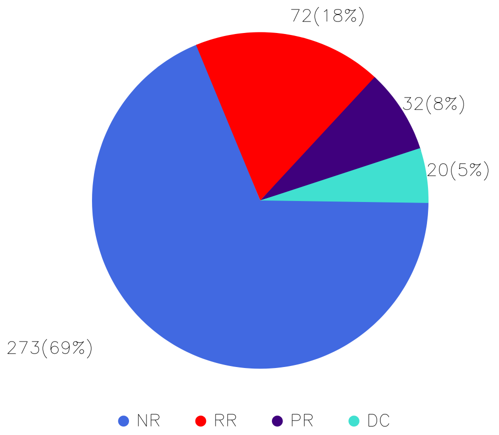

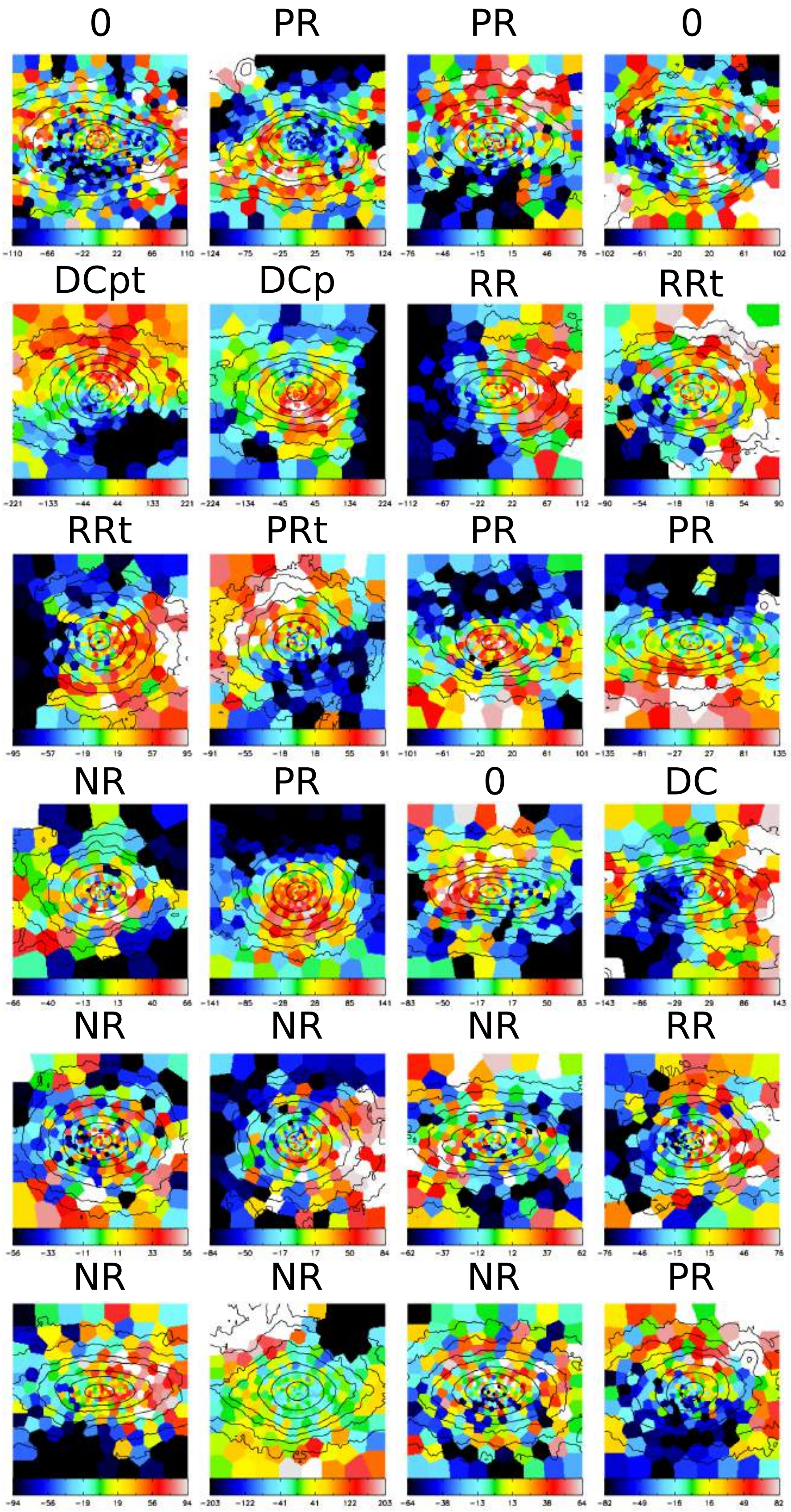
0
PR
PR
0
-110 -66 -22 22 66 110
-124 -75 -25 25 75 124
-76 -46 -15 15 46 76
-102 -61 -20 20 61 102
DCpt
DCp
RR
RRt
-221 -133 -44 44 133 221
-224 -134 -45 45 134 224
-112 -67 -22 22 67 112
-90 -54 -18 18 54 90
RRt
PRt
PR
PR
-95 -57 -19 19 57 95
-91 -55 -18 18 55 91
-101 -61 -20 20 61 101
-135 -81 -27 27 81 135
NR
PR
0
DC
-66 -40 -13 13 40 66
-141 -85 -28 28 85 141
-83 -50 -17 17 50 83
-143 -86 -29 29 86 143
NR
NR
NR
RR
-56 -33 -11 11 33 56
-84 -50 -17 17 50 84
-62 -37 -12 12 37 62
-76 -46 -15 15 46 76
NR
NR
NR
PR
-94 -56 -19 19 56 94
-203 -122 -41 41 122 203
-64 -38 -13 13 38 64
-82 -49 -16 16 49 82

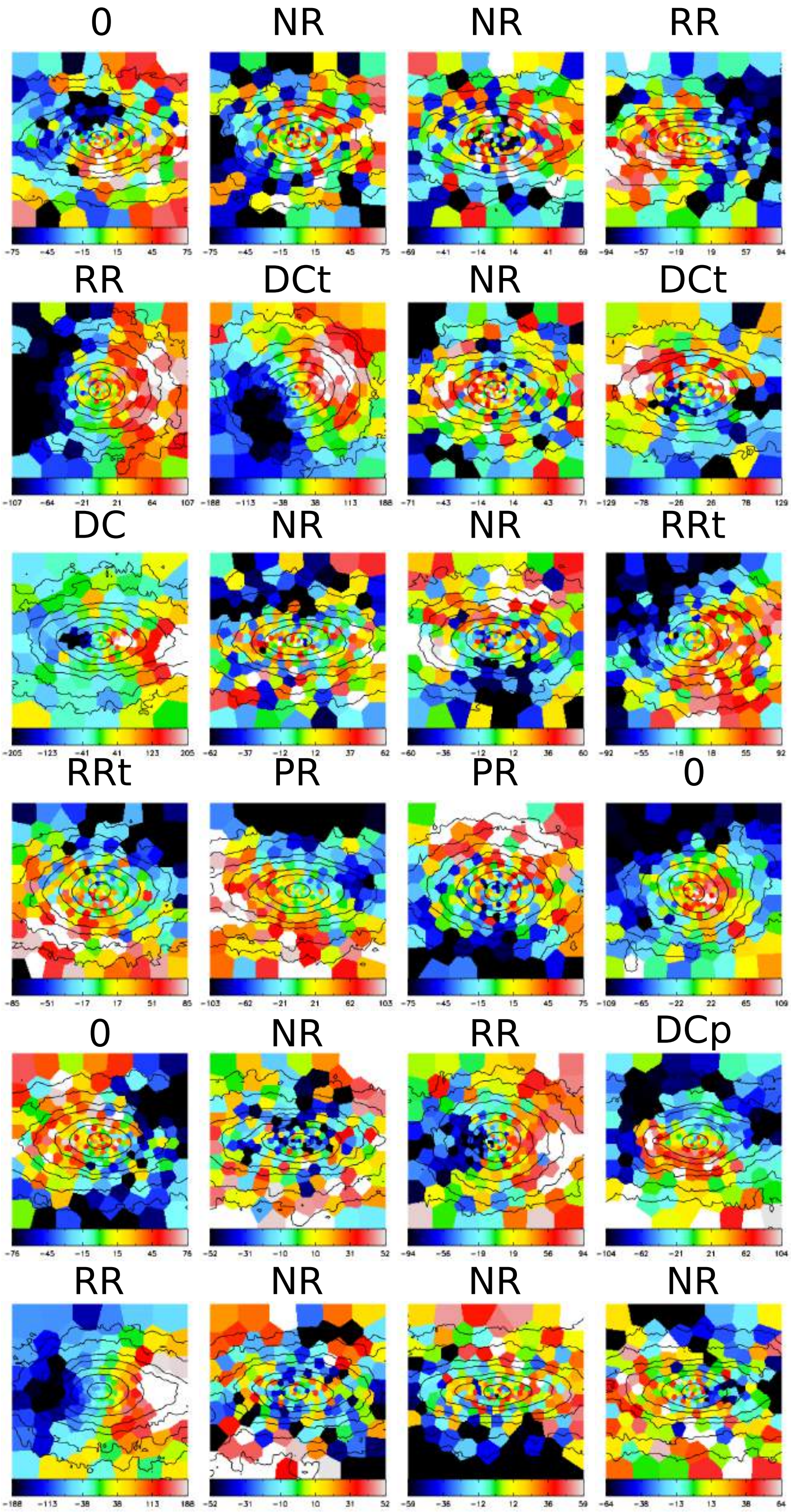

FIGURE 3.2: Velocity maps of the first 48 BCGs in our sample ordered from left to right and top to bottom in stellar mass.

The upper two panels of Fig. 3.4 show how the rotational patterns of the subhalos in BOX 4 are distributed among different mass bins. It can be seen that the relative fraction of regular rotators with respect to the other kinematical types is decreasing for increasing mass bins (I ignore the last bin due to its small sample size). Fig. 3.3 can be seen as a mass extension of the upper two panels in Fig. 3.4.
From the plot on the left side it is clear that the total number of BCGs in each mass bin decreases for higher masses. Since we already saw that more massive halos carry more massive BCGs, this is a result of the halo mass function. For the non-rotators the bulk of BCGs is in the lowest mass bin with each more massive bin having roughly one half of the galaxies in the bin before. This behaviour is similar for all kinematical types. But how are the kinematical types distributed in each mass bin? It can be seen that the fraction of non-rotators decreases significantly for higher masses. This is contrary to what we would expected from the trend in Fig. 3.4. The increasing fraction of the other three kinematical types can be explained by this decrease of the non-rotator fraction. It could be that the high non-rotator fractions result from low spatial resolution of low mass velocity maps. If a map is not resolved it can appear to be random motion leading to the classification as a non-rotator. Therefore, the bin with the highest mass appears most trustworthy. Nevertheless, high non-rotator fractions are expected because massive galaxies (especially BCGs) have a rich merger history. Therefore, these galaxies generally appear as classical ellipsoidal galaxies with low disk-like rotation.

Figure 3.3: These Histograms show the relative frequencies of each kinematical type split into 4 logarithmic mass bins each with $\Delta \log M_* = 0.2$. The lowest mass bin contains 197 BCGs followed by 111, in the next 53 and 36 in the heaviest. **Left:** Relative to the total amount of each class. **Right:** relative to the total amount in each mass bin.

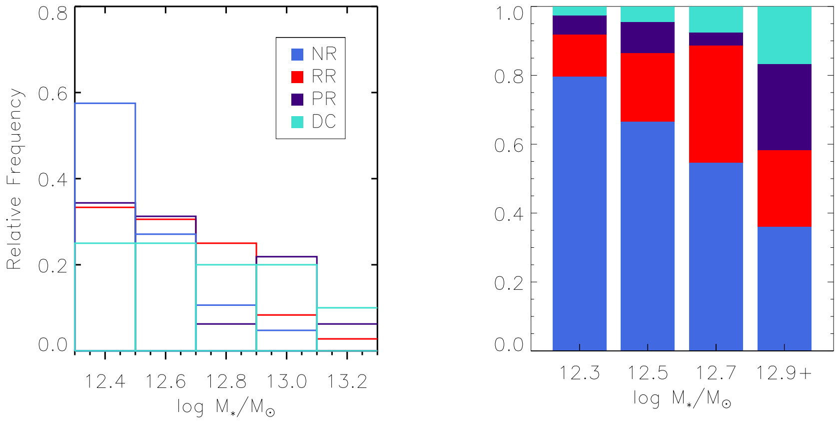

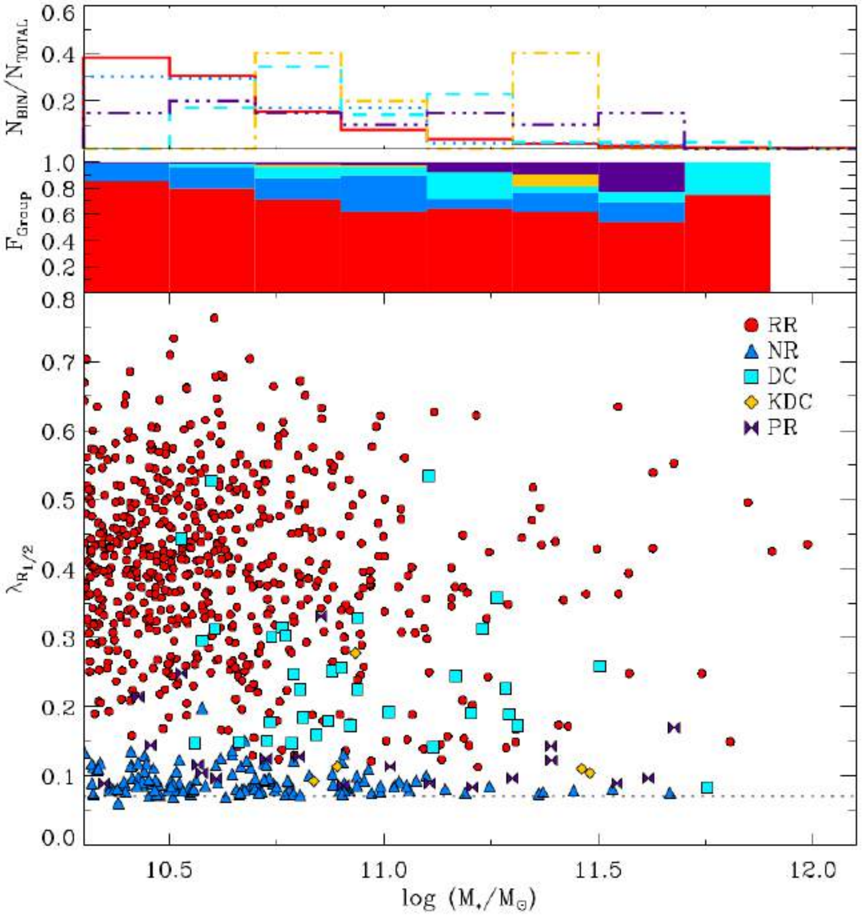

Figure 3.4: **Main panel:** λ_R versus M_* for all ETGs in Magneticum *Box4*. The different rotational patterns are indicated with symbols and colours as in the legend. **Middle panel:** Relative percentage of each kinematical group at the different stellar mass bins, colour-coded as in the lower panel. **Upper panel:** the number of galaxies of a certain kinematical group at different stellar mass bins normalised by the total number of galaxies within each group. The different kinematical groups are colour-coded as in the legend. This is Fig. B1 in F. Schulze et al. (2018).

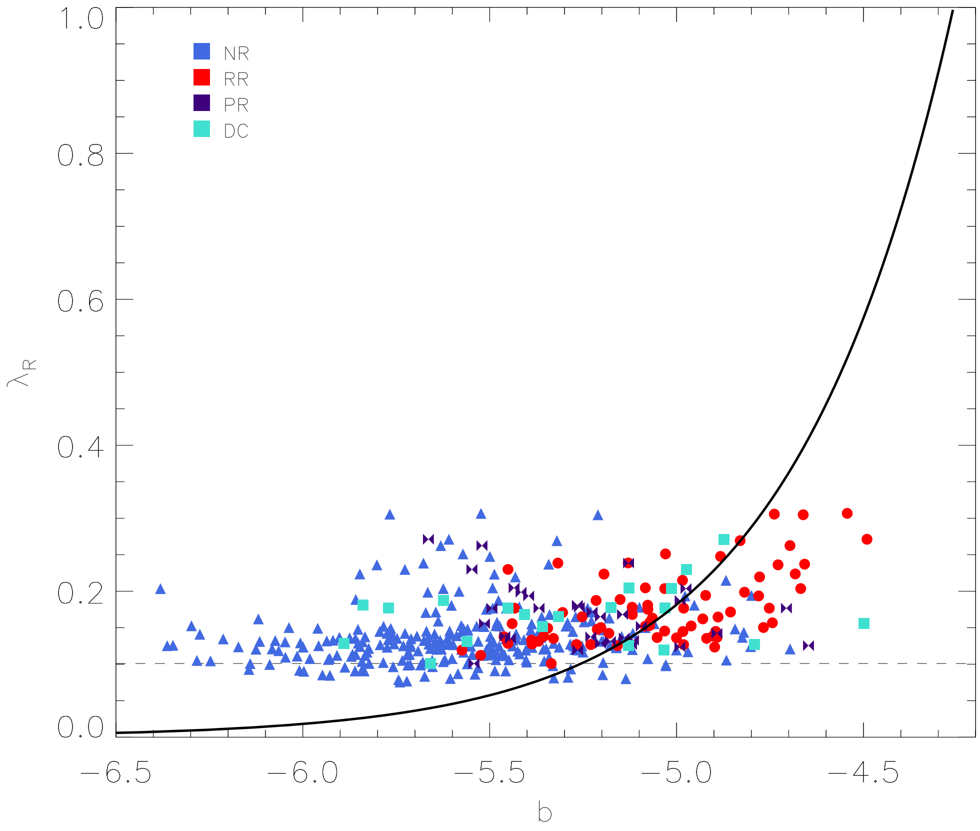

FIGURE 3.5: Relation between angular momentum proxy λ_R and b-value. Each kinematical type is indicated with symbol and colour as in the legend. The dashed line marks the resolution limit of the simulation. The solid black curve represents the prediction of a theoretical model outlined in F. Schulze et al. (2018)
for a galaxy with $M_* = 5 \times 10^{12} M_\odot$.

3.1.1 *b*-Value

F. Schulze et al. (2018) showed that there is a strong distinction between non-rotators and regular rotators based on b-value, where few non rotators show b-values below -5.0 with an average of $\bar{b} = -5.3$ and few regular rotators with b-values above -5.0 with an average of $\bar{b} = -4.7$. Classical spheroidal galaxies usually have higher masses than disk-like galaxies and therefore it seems logical that with higher masses the fraction of non-rotators increases. Fig. 3.5 shows the b-values for all classified galaxies. A clear separation between non-rotating and regular rotating BCGs can be seen here as well. They also follow the curve as predicted in the same paper for a galaxy with $M_* = 5 \times 10^{12} M_\odot$ that is slightly shallower. The shallowness can be explained with BCGs having large half mass radii. The exception are only some BCGs that scatter to higher rotation for intermediate b. Since the $b - \lambda_R$ plane can be reproduced with the classified BCGs, the majority seems to be classified correctly. The decreasing non-rotator fractions need a different explanation. But let us put this question aside until there is more information about their evolution and focus on the stellar kinematics that already appeared twice in these plots.

FIGURE 3.6: Different combinations of mean absolute stellar velocities $< |v| >$, standard deviation of the velocity distribution σ and total stellar mass M_*. The different kinematical groups are indicated by colour as in the legend.

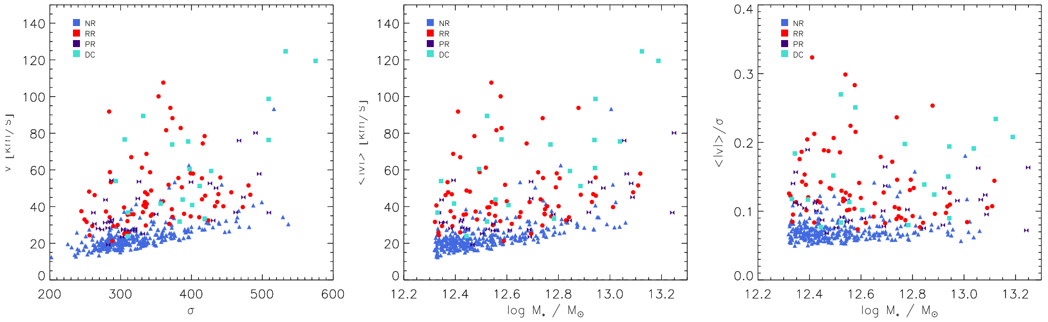

3.2 Stellar Kinematics

In Fig. 3.6, different combinations of mean absolute stellar velocities $< |v| >$, standard deviation of the velocity distribution σ and stellar mass M_* are displayed. It can be seen that velocity and velocity dispersion increase with stellar mass such that their fraction stays constant for increasing mass. For the angular momentum proxy that will be discussed in the following the velocities and dispersions in each cell are important.

3.2.1 Angular Momentum Proxy

In Fig. 3.7a the $\lambda_R - \epsilon$ plane is displayed for classified, unclassified BCGs and observed galaxies. For all three of these groups most galaxies are slow rotators. Notice how the simulated BCGs cannot reach very low λ_R-values. A large fraction scatters around the resolution limit. We can conclude that at these velocities we are mostly sampling noise and the values would decrease with higher resolution. This threshold is only 50% higher than in BOX 4 but combined with the fact that most subhalos at this mass range are slow-rotators this can explain why many subhalos were classified as non-rotators.
Nonetheless they are still below the slow rotator/fast rotator separation line. The stellar movement in observed galaxies is not dependent on the resolution of the telescope. Therefore there is no resolution limit for the observed sample. Additionally to resolution, another difference between simulated and observed galaxies are the ellipticities. Even though most simulated BCGs at this mass range are slow rotators and therefore non-extreme objects, they show large ellipticities. This is in part explained by the fact that all simulated BCGs are turned edge on for the calculation of ϵ. Therefore the ellipticities are at a maximum. Whereas the ellipticities of the observed galaxies are randomly distributed between the minimum and maximum values. High ellipticites are also found in other simulations (Bois et al., 2011).
A lot of information is contained in the distribution of the galaxies. Note how an overwhelming fraction of non-rotators lies on the resolution limit. Regular rotators and distinct cores have a non-negligible fraction that scatters to higher values. Sometimes even being fast rotators. This shows that a majority of non-rotators are indeed slowly rotating (the values here are an upper limit) and are not falsely classified due to small resolution in the maps. It is expected that rotationally supported galaxies like the fast rotators and distinct cores can reach higher λ_R-values than non-rotators.

Out of the 273 non-rotators only 2 are fast rotating (0.7%). The prolate rotators have a fraction of 12.5% fast rotating galaxies. These fractions are a lot higher for distinct cores (30%) and regular rotators (32%). Although in total the fraction of fast rotating galaxies is vanishingly low with less than 1%. Much more unclassified BCGs scatter to higher λ_R which is only in part due to a bigger sample size. There is also a considerable fraction of observed galaxies that are fast rotators. To understand this fact we have to have again a look at their masses. In Fig. 3.7b the dependence between λ_R and M_* is illustrated. For the sake of comparison the stellar masses for the classified BCGs are calculated within 10% R_{vir}. The stellar masses of the unclassified sample is calculated from the total stellar mass with a fraction of 40%, following Remus, Klaus Dolag, and Hoffmann (2017). There is a significant difference between the masses of the observed and the classified BCGs. The highest masses are populated by the classified BCGs ranging from around $\log M_*/M_\odot = 12.1$ to $\log M_*/M_\odot = 13.0$. The lowest masses are populated by the unclassified and MASSIVE galaxies ranging from around $\log M_*/M_\odot = 11.5$ to $\log M_*/M_\odot = 12.2$. We can suspect that there is a trend between λ_R and stellar mass.

Fig. 3.8 shows similar plots for observed galaxies with a wider range of masses. Fig. 3.8a shows the $\lambda_R - \epsilon$ plane of 260 ATLAS 3D galaxies. The dotted magenta line show the edge-on view for ellipsoidal galaxies integrated up to infinity with $\beta = 0.70 \times \rho$. The solid magenta line is the corresponding curve restricted to an aperture at $1R_e$ and for $\beta = 0.65 \times \rho$. The black dashed lines correspond to the location of galaxies with intrinsic ellipticities $\epsilon_{\text{intr}} = 0.85, 0.75, 0.65, 0.55, 0.45, 0.35$ along the relation given for an aperture of $1R_e$ with the viewing angle going from edge-on (on the relation) to face-on (towards the origin).

For our purpose of comparing the two samples, their masses are most important. Note how most massive galaxies lie below the fast rotator/slow rotator separation line. And that is already for masses $\log M_*/M_\odot = 11.5$. Lower than the minimum mass of the MASSIVE sample and an order of magnitude smaller than the classified BCGs. Fig. 3.8b shows that the change between fast rotation and slow rotation happens quite abruptly at a mass cut of around $\log M_*/M_\odot = 11.5$ as can be seen clearly from the histogram in the top panel.

We can conclude that the fraction of slow rotators becomes suddenly larger for all galaxies with a mass above $\log M_*/M_\odot = 11.5$. The 297 BCGs of our sample underline this observation by being mostly slow rotators.

(A) The $\lambda_R - \epsilon$ plane. The solid green line shows the slow rotator/fast rotator separation line. The solid magenta line is the corresponding curve restricted to an aperture at $1R_e$ and for $\beta = 0.65 \times \rho$.

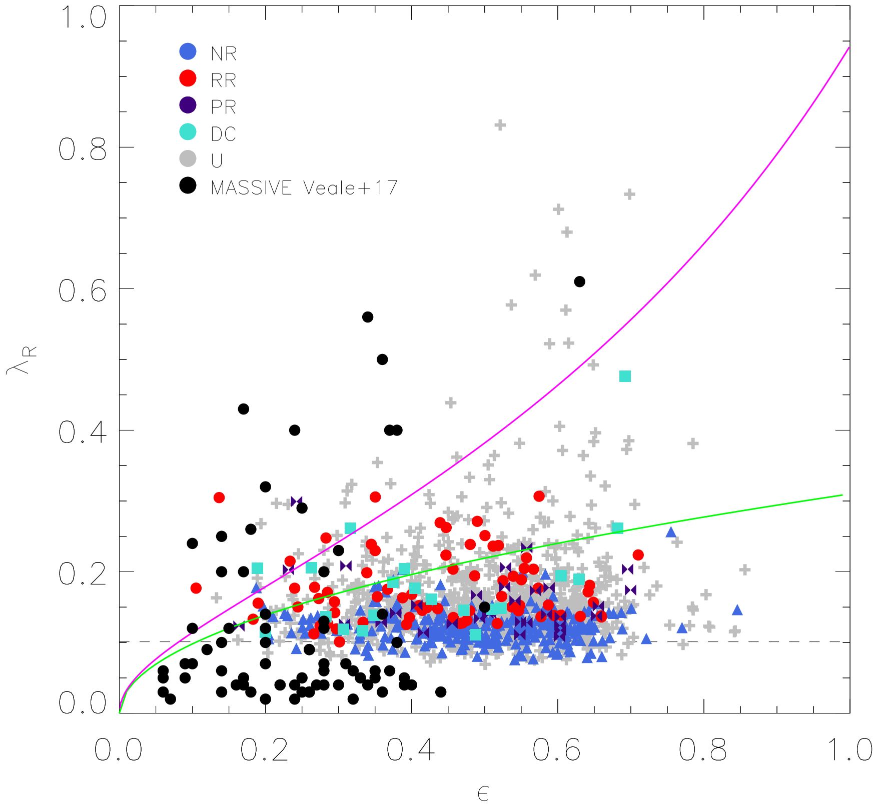

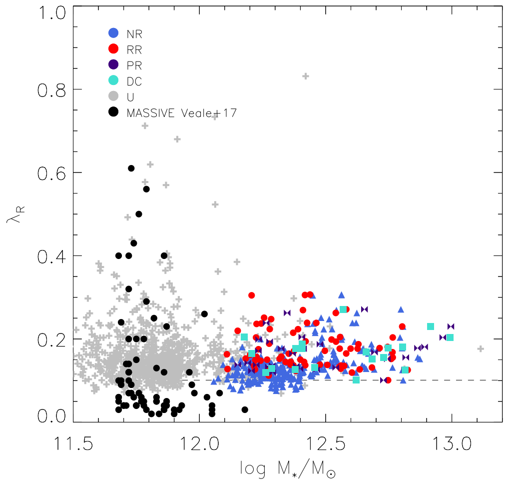

(B) λ_R vs central stellar mass M_*.

FIGURE 3.7: Relationship between λ_R and central stellar mass $M*$ (**bottom**), ellipticity ϵ (**top**) for 397 classified galaxies, 851 non-classified galaxies (grey plus signs) and 78 observed galaxies (solid black dots) from the MASSIVE survey described in Veale et al. (2017). The different galaxies are indicated with different colours and symbols as in the legend. The dashed black line marks the resolution limit of the sample.

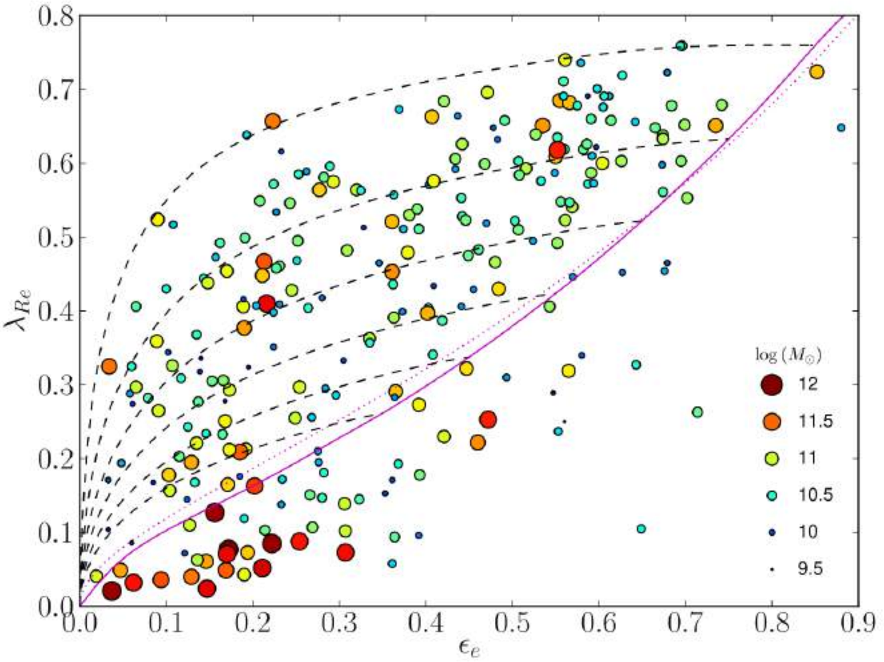

(A) λ_R versus ϵ for all 260 ATLAS 3D galaxies. Mass is indicated by colour and size of the symbol as indicated. For details on the different lines see text. This is Fig. 9 in Emsellem, Cappellari, Krajnović, et al. (2011)

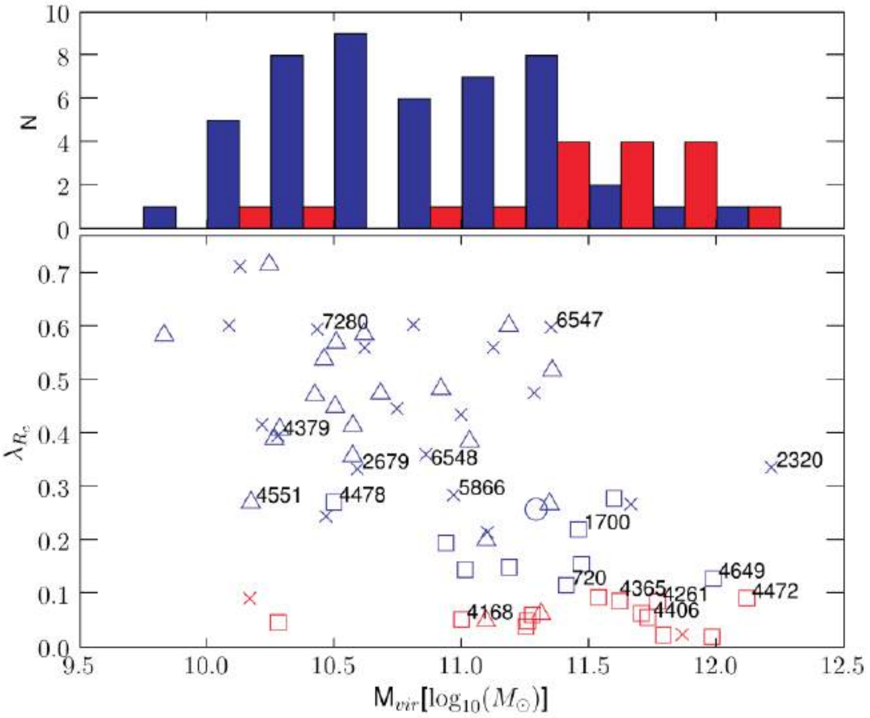

(B) λ_R versus $M_{\rm vir}$ for ETGs from the SAURON sample. The top panel shows histograms of $M_{\rm vir}$ for both slow (red) and fast rotators (blue). This is Fig. 7 in Emsellem, Cappellari, Krajnović, et al. (2007)

FIGURE 3.8: Observed relationship of λ_R against two different properties. **Top:** ellipticity ϵ and **bottom:** virial Mass $M_{\rm vir}$.

3.2.2 Higher Order Moments

The resolution line in Fig. 3.7 illustrates how hard it is to properly resolve kinematics. For the higher order moments an even higher resolution is needed. This resolution is assured with a high particle number in each cell as described in section 2.2.1 but let us see how well the kinematics of the BCGs in our sample compare to observations.

For comparing large samples of galaxies it is useful to define a single property for the whole galaxy. In this case, these are the mass weighted higher order moments for the whole BCG as described in section 2.2.3. Fig. 3.9 shows h_n versus central stellar mass $\log M_*/M_\odot$ with $n = 3, 4$ for the same three groups as in section 3.2.1. Obviously, we see the same mass trends as before. This makes a comparison slightly more difficult. However, it is unavoidable due lacking observational data for very high masses. Nevertheless, most galaxies in all three samples are slow rotators and should therefore have similar behaviour in h_n as well. We can see that this is indeed the case. All three samples scatter around $< h_3 >= 0$ in Fig. 3.9a and $< h_4 >= 0.05$ in Fig. 3.9b. The unclassified sample seems to scatter to higher values. These might be outliers because of the increased sample size. The scatter between the observational sample and the classified sample is very similar. In $< h_4 >$, the scatter seems to be larger in the direction of small values with very few being negative. We can conclude that the simulated BCGs resolve the higher order moments at least globally. So let us see if they resolve local features.

In Fig. 3.10 the maps of all calculated LoS-velocity moments are displayed for each of the four poster child maps. These maps show the rotational patterns described in section 2.2.2 very clearly. The maximum value for the colour bar was determined by taking the maximum absolute mean velocity so that only 15% of the cells have higher mean velocities. This ensures that cells with outlier values do not shift the whole colour bar and therefore the patterns are easier to see. As expected, the non-rotator has the lowest mean velocities in each cell with $-80 < \overline{v} < 80$. The regular

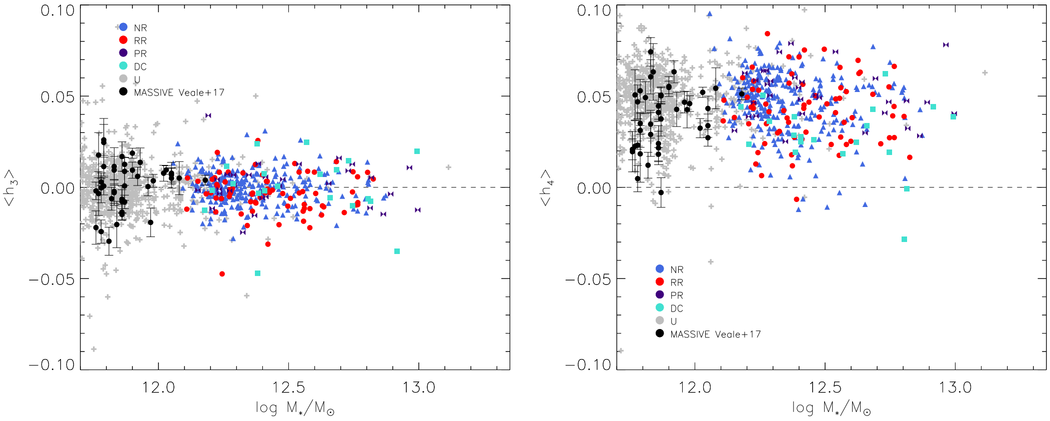

(A) $< h_3 >$ versus $\log M_*/M_\odot$.

(B) $< h_4 >$ versus $\log M_*/M_\odot$.

FIGURE 3.9: Mass weighted average higher order moments $< h_3 >$ (**top**), $< h_4 >$ (**bottom**) versus central stellar mass $\log M_*/M_\odot$ for 397 classified BCGs, 851 non-classified BCGs (grey plus signs) and 78 observed galaxies (solid black dots) from the MASSIVE survey described in Veale et al. (2017). The kinematical features are indicated with different colours and patterns as can be seen in the legend. For $< h_n >= 0$ the line of sight velocity distribution becomes a standard Gaussian. This behaviour is emphasised with the dashed black line.

rotator and the prolate rotator have similar mean velocities with $-112 < \overline{v} < 112$ and $-117 < \overline{v} < 117$ respectively. The distinct core features the highest mean velocities among the four examples within a range of $-163 < \overline{v} < 163$. The velocity dispersion are similar for all four BCGs which was expected since they have similar masses ($8.7 \times 10^{12} < M_{\odot} < 1.16 \times 10^{13}$, see Fig. 3.10 for details). Nevertheless, the maps differ substantially. The standard deviation follows the mean velocity in the sense that the regions with low $\overline{|v|}$ also have low σ, i.e. the green regions in the velocity maps correspond to blue regions in the dispersion maps and blue and red regions in the velocity maps correspond to red regions in the dispersion maps. Since we expect a larger standard deviation for higher velocities, this observation makes sense. Furthermore, all BCGs but the regular rotator show high dispersion in their centres. The centre is at the minimum of the potential well where more potential energy is transformed into motion. This can be explained with the virial theorem.

The maps of the higher order moments all have the same colour bar with a range from $-0.1 < h_n < 0.1$ for easier comparison. They are difficult to interpret.

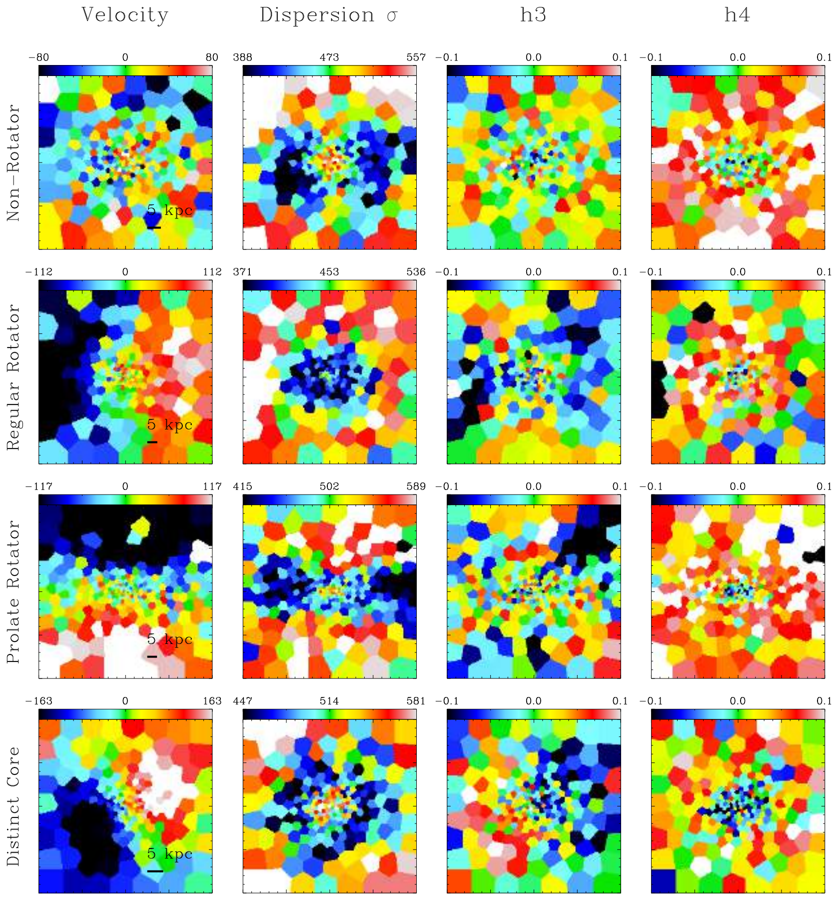

FIGURE 3.10: Maps of the four LoS-velocity moments for poster child BCGs. The non-rotator is BCG16 with a stellar mass of $1.09 \times 10^{13} M_{\odot}$, the regular rotator BCG28 with $8.80 \times 10^{12} M_{\odot}$, the prolate rotator BCG11 with $1.16 \times 10^{13} M_{\odot}$ and the distinct core is BCG29 with a stellar mass of $8.78 \times 10^{12} M_{\odot}$

Nevertheless, there are a couple of things that can be observed. h_3 seems to be somewhat randomly distributed. In the case of the distinct core, however, it is possible to see an anti-correlation between h_3 and $\overline{v}$. The blue region in the velocity map corresponds to the red region in the h_3 map and vice versa. This anti-correlation has been detected in multiple observations (van de Sande et al. (2017), Emsellem, Cappellari, Peletier, et al. (2004), Bender, Saglia, and Gerhard (1994)) and is connected to a formation history where fast rotating systems formed in gas rich mergers (Naab, L. Oser, et al., 2014). h_4 maps mostly consist of cells with positive values, causing the overall positive mean values $\overline{h_4}$ that could be seen in Fig. 3.9b. Additionally, the centres of each BCG show negative values of h_4. In order to investigate the local behaviour in a more systematic way, the values in each cell can be plotted together in one window for multiple BCGs. The result is shown in Fig. 3.11. The top row displays the relationship between h_3 and v/σ for each of the kinematical classes. Every point represents one Voronoi cell of one of the BCGs in the classified sample. The points are coloured with their distance from the centre in units of half mass radii. The bottom row displays the $h_4 - v/\sigma$ relation for the same BCGs. van de Sande et al. (2017) defined five different classes from their $h_n - v/\sigma$ relation. The first class has a vertical relationship between v/σ and both higher order moments h_n. Especially the non-rotators but also the regular rotators and the prolate rotators of our sample can be associated with that category. This is sensical because they associate this group with the slow rotators in their sample and the overwhelming majority in our sample are slow rotators. The distinct cores fall into the third category, showing an anti-correlation and a broadening of the wings. Since there is only a weak signal we do not investigate the slopes but Wang et. al (in prep.) investigated the slopes of MAGNETICUM BOX4 subhalos in more detail.

The trend that the lowest values of h_4 are found in the centres as in Fig. 3.10 can clearly be seen for all classes except the distinct cores - most clearly in the non-rotators. This is not observed for class I galaxies in van de Sande et al. (2017) and could be an indicator for the unique physics in BCG centres. Since positive values for h_4 are found when the LOSVD traces regions with significantly different circular velocities (Gerhard, 1993), negative values could therefore be a tracer of especially similar velocities. This in turn could indicate a stream or a flow-like behaviour.

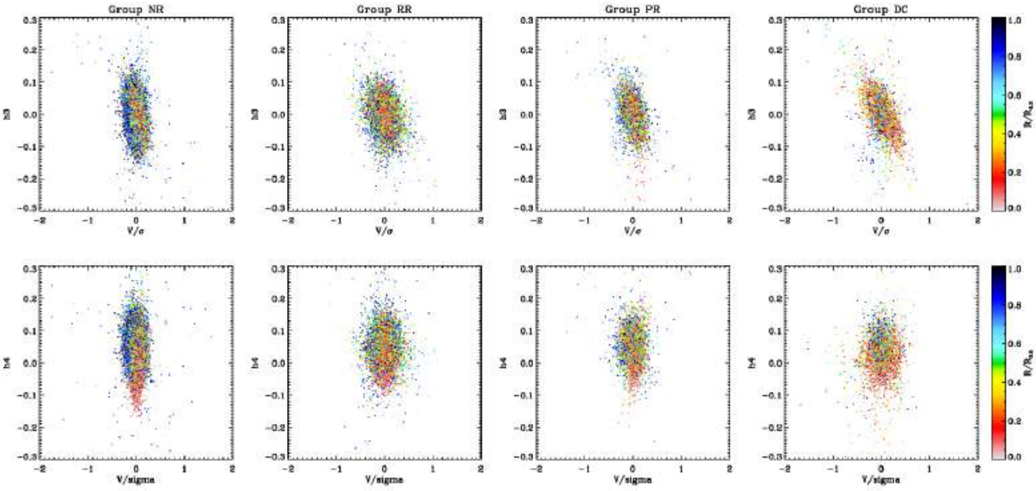

FIGURE 3.11: h_n vs V/σ for our four different kinematical group. Each dot is coloured with respect to their relative distance to the galactic centre and represents one Voronoi cell. These are stacked plots for all subhalos in the respective group.

3.3 Summary

We have seen that even for masses as high as the most massive BCGs, calculating internal kinematics is working at the limit of resolution. Nevertheless, many features could be resolved which is remarkable, given the sheer size and the cosmological context of the simulation. This extends kinematical results to up to 10 times higher masses than the most massive BCGs from the MASSIVE survey and therefore to an uninvestigated mass-regime.

Most of the classified BCGs are slow-rotators. Thus continuing the trend that could already be seen in intermediate mass observations. This suggests that there are indeed two distinct populations that can generally seen in the $\lambda_R - \epsilon$ Plane.

Non-rotation is reasonable for classical spheroidal ETGs with a rich merger history that is expected in cluster centres. This is underlined by the separation of non-rotators and regular rotators in the $b - \lambda_R$ plane. However, we find that the fraction of non-rotators is decreasing with mass in our sample - reversing the trend that was seen for lower masses. The highest mass bin shows very similar fractions for all kinematical classes. This should be the most trustworthy mass-regime due to the higher resolution. One quarter of non-rotators is still significantly larger than the fractions measured in Box 4 of the Magneticum simulation. Furthermore, a fraction of roughly one fourth prolate rotators continues the trend that already started in Box 4 and is expected by e.g. Krajnović et al. (2018). Keep in mind that this is an underestimation because high mass distinct cores showed prolate rotation but were not classified as such. Furthermore, we only classified galaxies as prolate rotating with a misalignment angle of larger than 45°. The decreasing non-rotator fraction is interesting nonetheless and needs further investigation.

The $\lambda_R - \epsilon$ plane shows that most members of each kinematical group are slow-rotators. However, distinct-cores and regular-rotator scatter to higher values. Most of the non-rotators lie on the resolution limit. Therefore, it is hard to decide which are really non-rotating and which seem to be non-rotating but instead their kinematical pattern cannot be resolved.

We showed that, although it is difficult to resolve local features in the BCGs, our sample reproduces the global averages of the higher moments of the velocity distribution seen in observations very well. Suggesting that also for masses above the ones observed in MASSIVE similar $< h_n >$ are to be expected. Regarding the local features of the higher order moments the distinct cores in our sample even reproduce the anti-correlation between h_3 and V/σ expected for rotating systems (van de Sande et al., 2017). Most of our BCGs show the lowest values of h_4 in their centres. This is different from the observations in van de Sande et al. (2017) where they do not find a correlation between radius and h_4 strength for Class I, the class that they associate with slow-rotators. This could be an indicator of the unique physics acting in BCG centres.

Chapter 4

Stasima

The previous chapter introduced kinematical properties that help us understand the stellar motion within BCGs and galaxies in general. In order to use the power of a cosmological simulation to its full extent, we want to find out how differences in these properties arise and if they are connected to environmental properties. Of special interest is the influence of a cool core on stellar dynamics. Chapter 1 introduced cooling flows and stated that a cool core is characterised by low cooling times and low central entropy. This information can be comprised in a single parameter: the *coolcoreness*. The details of its calculation will be described in the following section but suffice to say that a value of 100% indicates a true cool core and a value of 0% indicates a true non-cool core. Fig. 4.1 shows the coolcoreness in relation to the total stellar mass of the BCG and different morphological and kinematical parameters: the b-value, λ_R, $\overline{h_3}$ and $\overline{h_4}$ at z=0. It can be seen immediately that there is no evident scaling between coolcoreness and any of the properties at z=0. This does not mean that there is no influence between those properties at all. The properties could influence each other on different time scales. Furthermore the absolute values might not

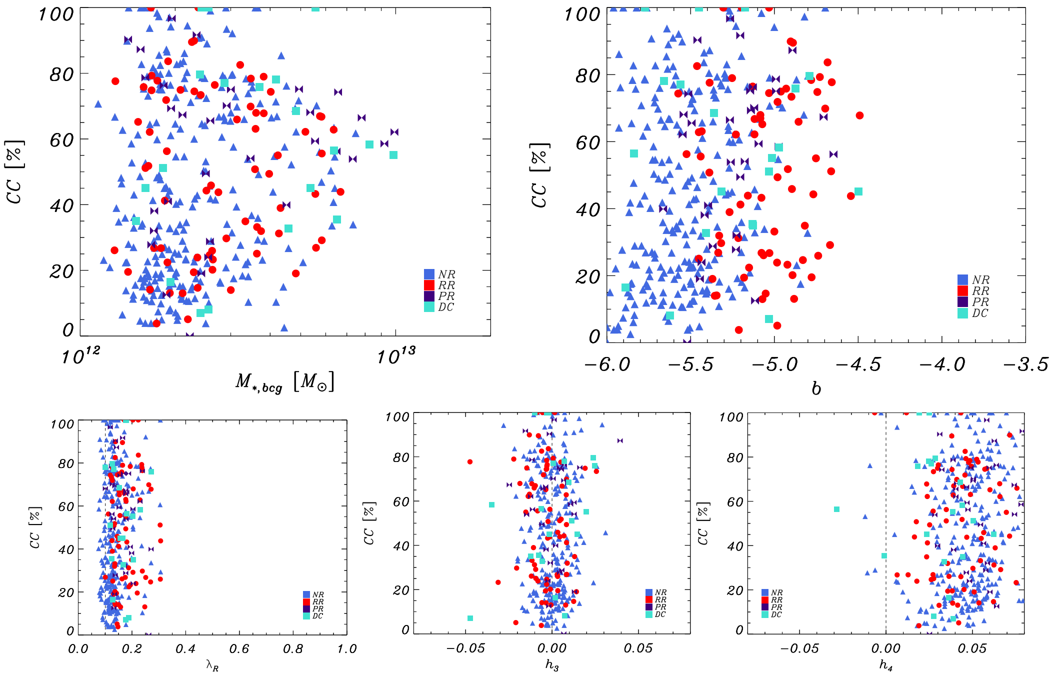

FIGURE 4.1: Coolcoreness in relation to total stellar mass, b-value, λ_R and the mean higher order moments $\overline{h_3}$ and $\overline{h_4}$ at z=0. Kinematical types are indicated as in the legend.

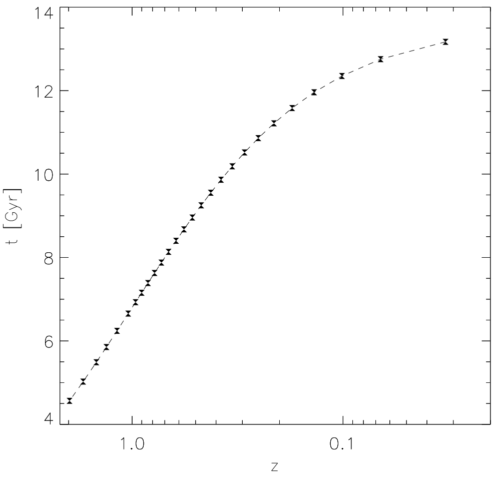

FIGURE 4.2: Redshift and absolute time for all used snapshots that contain particle data (indicated with hourglasses). They are spaced mostly equally on the logarithmic redshift axis.

have an impact on the other properties but time differentials of the properties could be relevant. Because of the possibility that properties at $z = z_1$ depend on the properties at $z = z_2 > z_1$ it is important to realise that they are dependent variables. If they would be independent we could treat the same galaxy at different redshift as independent data points. Additionally we want a case study of individual evolutions of BCGs with specific properties. Therefore, all BCGs have to be traced.

4.1 Tracing

In order to investigate the temporal *evolution* of BCG properties for an individual BCG the halo has to be traced. Following a single halo is difficult for one main reason: merging. In the course of their lives, most subhalos and even some halos will merge with other halos. This does not pose a problem for tracing a halo from high redshift to lower redshift because after a merger the reasonable thing to do is to trace the merged system. Because we classified our sample at redshift zero, however, we have to trace from low redshift to high redshift. At every point in time a merger happened an ambiguity is introduced: Which of the merged subhalos should be traced? Fortunately, there is a simple answer in the case of tracing BCGs. It is very likely that one of the two galaxies was already the BCG in the time step before. Therefore, the galaxy of interest should already have been in the centre of the potential and thus be identified by SubFind as the first subhalo. Halo mergers would still pose a problem here. Therefore, another safety measure is needed: the black holes.

4.1.1 Black Holes

In the simulation BHs are represented by collision-less 'sink particles' that can grow in mass by accreting gas from their environments or by merging with other BHs. The mass accretion rate $\dot{M}_\bullet$ is estimated by using the Bondi-Hoyle-Lyttleton approximation.

A black hole is seeded at the position of a particle with the highest binding energy

in a halo for total stellar masses larger than $10^{10} M_{\odot}/h$. This guarantees that the BHs are seeded only in halos representing clearly resolved galaxies, where efficient star formation took place. The BH then has a starting seed mass of $3.2 \times 10^5 M_{\odot}/h$ that quickly increases until reaches the stellar-BH-mass relation
There is no 'pinning' implemented in order to keep the BH in place. Rather, momentum conservation is implemented strictly. This concerns momentum transfer during gas accretion and BH merging. If the host galaxy becomes a satellite of a larger halo the BH particle remains within the host galaxy because of the dynamical friction force that is explicitly calculated following the Chandrasekhar formula. All classified galaxies are traced individually from z=0 to z=2. Particle data is stored every fourth time SubFind is executed on-the-fly. See Fig. 4.2 for their respective Δz. At first the routine searches for the halo that belongs to the BCG using SubFind. Then it searches for the most massive black hole at the central position of that halo within a radius of $0.1 R_{vir}$ and stores its position and ID. Note that this is the same radius that was used before to determine the half mass radius for the BCG.
Now the iteration to earlier snapshots begins. For each iteration, the same black hole has to be found again. This happens by searching for a black hole particle with the same ID within a box 1000kpc around the old position. If no black hole is found the box length is doubled. This iterative process is taken because it saves a lot of time and memory to not read every particle of that snapshot. Once the black hole is found it searches for the halo that minimises its distance between its centre and the position of the black hole. Since the distance of BH particles to the potential minimum is usually less then half the softening length (Hirschmann et al., 2014) this does not pose a problem in the case of eventual fly-by of other halos. The maximum redshift of z=2 guarantees sufficient resolution for our purposes and for the BH to be already seeded.

4.1.2 Descendent Trees

For some of my investigations, a higher temporal resolution was needed. This included animations of the trajectories of satellite galaxies around the central galaxy in order to get a visual understanding of the merger history of a BCG. Halo and sub halo properties like positions and mass are available every time SubFind is calculated on-the-fly. For all of these snapshots descendent trees are calculated as well. A descendent tree is an array that connects the IDs of subhalos at snapshot n with the IDs of a snapshot at $n+1$. This is a direct means of tracing a subhalo.

4.2 Environmental Properties

The kinematical properties were already introduced in the two previous chapters. Some environmental properties that are used in the following were introduced in the previous chapters as well. Nevertheless, a quick summary of all the environmental properties will be presented here in order of their appearance.

Three properties will be investigated that are connected to the galaxy cluster. Firstly, the virial cluster mass that describes the total mass of all particle types within the virial radius. The second property is the temperature of the gas. Both of these properties are calculated by SubFind on-the-fly (K. Dolag, Borgani, et al., 2009). The third property is the coolcoreness. A detailed description of the coolcoreness can be found in Hinz (2018). In Chapter 1 it was already discussed that low central cooling time and low central entropy are good proxies for a cluster with a cool core. Both properties were calculated as mass-weighted median values of the ICM particles within a region of $0.00 < r < 0.048R_{500}$ for 1199 halos. Fig. 4.3 shows the correlation between these two proxies. They have a tight relation with small scatter in log-log scale that can be fit with a linear regression. The coolcoreness of a halo is determined by their relative distance to the starting point. Points below the starting point are assigned a coolcoreness of 100% and halos above the ending point are defined to have a coolcoreness of 0%.

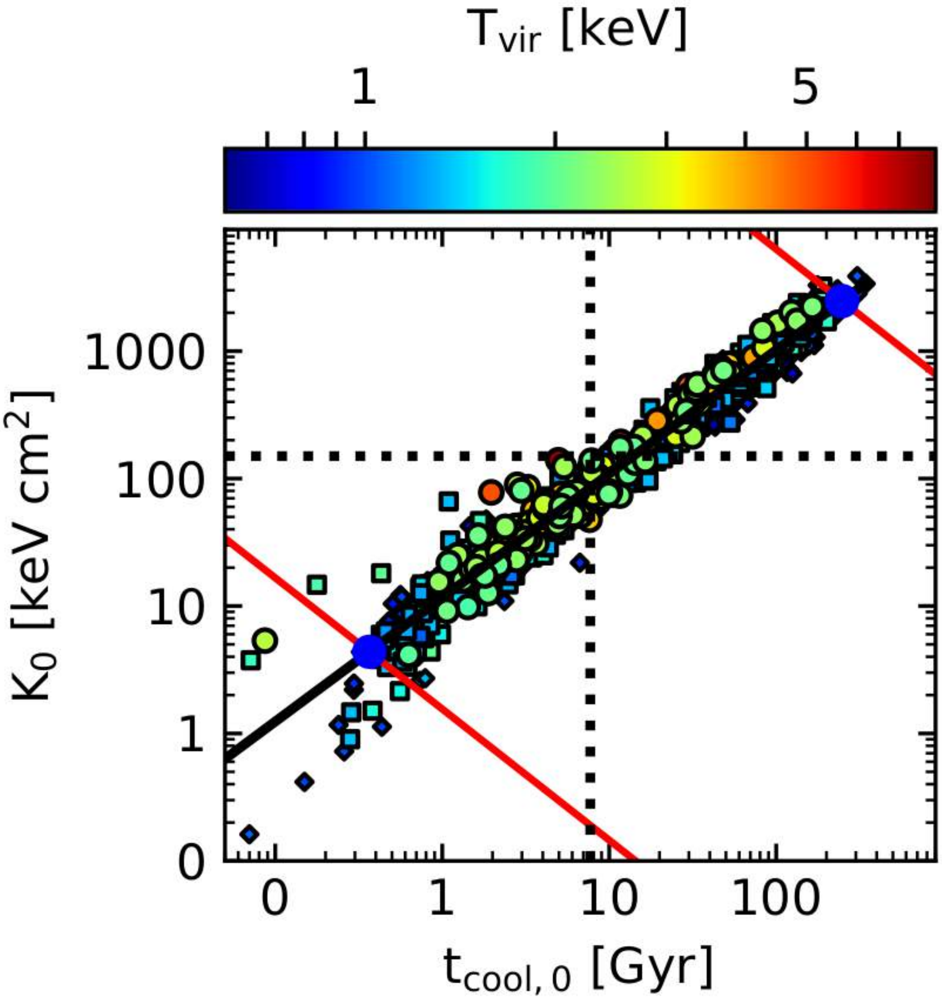

FIGURE 4.3: Correlation between central cooling time and central entropy of 1199 halos. The halos are colour-coded by their virial temperature. The sample is subdivided into high-mass halos (circles), intermediate-mass halos (squares) and low-mass halos (diamonds). The dotted vertical and horizontal lines represent thresholds on the quantities that divide the sample into CC and NCC clusters. The black line is the regression line fit. The blue points with vertical red lines indicate the starting and ending point from which the coolcoreness of the halos is determined. This is figure B.3 in Hinz (2018).

Additionally three properties will be presented that describe the environment of the BCG. First, the stellar mass that is the sum of the masses of all stellar particles within $10\%R_{\mathrm{vir}}$. The specific star formation rate: This is the star formation rate calculated on-the-fly with SubFind divided by the total stellar mass of the subhalo (BCG+ICL) that is also calculated on-the-fly with SubFind. The third property is the b-value that was already introduced in section 2.2.3. It is calculated from specific angular momentum and stellar mass within one half mass radius of the BCG.

The remaining properties are the black hole mass, fossilness and BCG to total stellar mass ratio. There are two variables that describe the mass of the black hole: the true mass and the dynamical mass. The first describes mass accretion according to the description in subsection 4.1.1. The latter is tied to dynamical events in the subhalo and can e.g. increase during mergers. The dynamical mass is roughly a factor of two higher at z=2 but both are very similar for low redshift. The first is used in the statistical evolution of residual properties and the latter is used in the scaling relations with kinematical properties. The fossilness is the fraction between the stellar mass of the most massive satellite galaxy within the halo and the total stellar mass (BCG+ICL) of the BCG. Both masses are calculated by SubFind. The BCG to total stellar mass ratio is, as the name suggests, the fraction between the stellar mass of the BCG within $10\%R_{\mathrm{vir}}$ and the total stellar mass calculated by SubFind.

Chapter 5

Temporal Evolution of Kinematics and Environmental Properties

Now that we will have a look at the temporal evolution of BCG properties, there are two main questions. The first and obvious question is: 'How do individual properties evolve over time?' These properties include the kinematical properties that we became acquainted with in Chapter 2 and global properties that were summarised in the previous chapter. This question will be tackled in the first of the following sections and act as an overview in order to get a feeling for these different properties. Then we are finally able to tackle the second question that asks how these properties evolve *with* each other or more precisely: 'What influence does the environment have on stellar kinematics in BCGs?'

5.1 Epeisodia I: Statistical Evolution

The details in the evolution of each of those properties depends on an unfathomable amount of factors. Each BCG faces unique initial conditions and merger scenarios that all influence each other. The following is therefore not a prediction of how different types of galaxies will evolve but rather a statistical analysis. The sample is split into whether the BCGs showed signs of non-rotation, regular-rotation, prolate-rotation or a distinct kinematical core at redshift zero. This split enables us to compare BCGs in the sample with other BCGs of the same sample because observational data for the evolution of specific galaxies does obviously not exist. In order to compare the regular-rotators and non-rotators in a more meaningful way the sample size of the non-rotators was reduced such that the minimum stellar BCG masses of the regular rotators and non-rotators are comparable. Since a considerable fraction of low mass BCGs might have been wrongfully classified as non-rotators due to a lack of resolution (Chapter 2) this choice is justified. In total the evolution of 134 non-rotators, 69 regular rotators, 29 prolate rotators and 18 BCGs with a kinematically distinct core were investigated.

There are numerous other ways the sample could be subdivided instead of splitting them up by kinematical type at z=0. Another possible classification could be fast and slow rotation. Since the overwhelming majority is slowly rotating, this leads to a large difference in sample sizes, rendering the statistical analysis ineffective. However, we could expect that with decreasing mass, the fraction of fast rotators increases. Hence we could classify all galaxies at every snapshot into slow and fast rotating. This way, however, the same galaxy would be treated as many independent galaxies solely because of different redshift. The information about the individual and dependent evolution would be lost. The advantage of classifying them by their kinematical type at z=0 is therefore that we have comparable sample sizes and a way of finding possible formation pathways for each of those groups.

In order to have a synoptic presentation of the 13 different properties, they are divided into four groups. At first we look at the global properties of the cluster. This includes the virial cluster mass M_{vir}, the gas temperature T and the coolcoreness CC that was introduced in the previous chapter. The second group are selected kinematical properties of the BCGs that include the angular momentum proxy λ_R and the mean higher order moments of the line of sight velocity distribution $\overline{h_3}$ and $\overline{h_4}$. There are many properties that could influence the kinematics. The third group is concerned with global properties of the BCG. This includes their stellar mass M_*, specific star formation rate SSFR and the morphological parameter b. The fourth and final group collects residual properties: the black hole mass M_{bh}, the fossilness $M_*^{\mathrm{sat}}/M_*^{\mathrm{cent}}$ and the central region stellar mass to total stellar mass ratio $M_{*,\mathrm{BCG}}/(M_{*,\mathrm{BCG}} + M_{*,\mathrm{ICL}})$.
Each panel displays the temporal evolution of one of those properties. Every column displays a property for one kinematical type classified at z=0. Top rows display the evolution for non-rotators, the second row displays regular rotators, the third row displays prolate rotators and the bottom rows display distinct core BCGs. Grey lines show the temporal evolution of the property for each individual galaxy. At each available redshift slice the median value of the property for all BCGs of that type was calculated. The median values are connected with a solid line in different colours for each property. The error bars contain 68.2% (one standard deviation) of BCGs of the sample. They are coloured depending on the kinematical type the sample is associated with. Blue for non-rotators, red for regular rotators, purple for prolate rotators and turquoise for distinct core BCGs.

Halo Properties

Fig. 5.1 shows the temporal evolution of halo properties for each of the four kinematical types. The initial median virial halo mass lies below $3 \times 10^{13} M_\odot$ for all of the kinematical types.

The virial halo mass increases over time. The final median virial halo mass lies between $2 \times 10^{14} M_\odot$ for non rotators and $4 \times 10^{14} M_\odot$ for distinct core BCGs. This discrepancy is likely due to the larger sample of non-rotators that has much more BCGs at lower masses. The different sample sizes influence the error bars especially. The scatter is relatively similar for each kinematical group but the error bars become smaller for increasing sample sizes. Showing that the distribution between minimum and maximum values is not uniform.

The median gas temperature lies around 1keV for all kinematical classes and gradually increases to values between 2keV $< T <$ 3keV. The gas temperature follows the virial mass. A deeper potential well leads higher energies and therefore to higher temperatures. For a theoretical analysis of temperature and mass evolution in a self-similar evolution model see Böhringer, K. Dolag, and Chon (2012).

All samples start with a median coolcoreness of 100% and gradually decrease until they reach a median coolcoreness between 50% to 60%. The scatter increases dramatically ranging from true non-cool core to true cool core for each kinematical class. This is underlined by the standard deviation comprising almost 60% of the possible values.

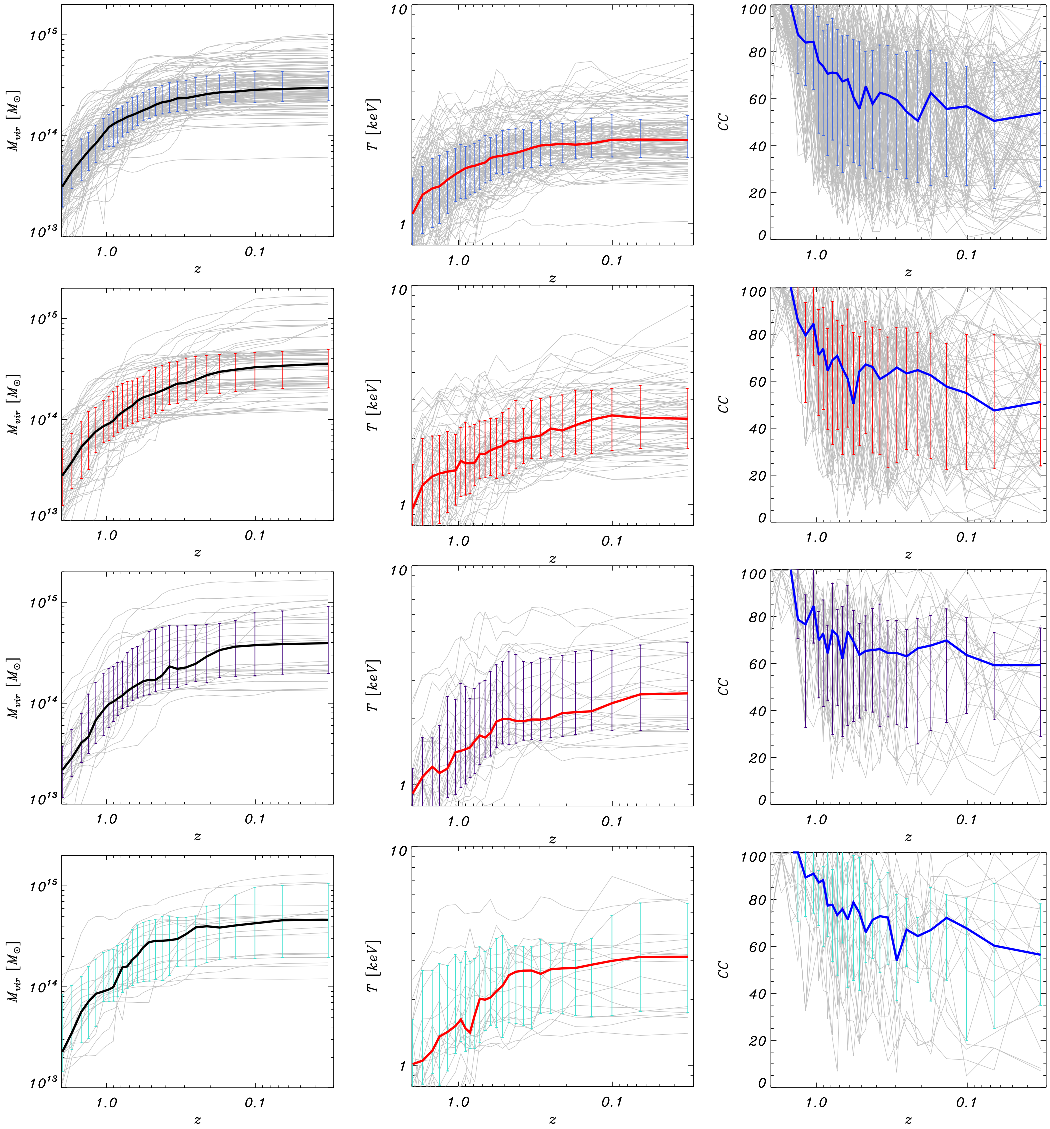

FIGURE 5.1: Temporal evolution of halo properties for each of the kinematical classes for 134 non-rotators (top row), 69 regular-rotators (second row), 29 prolate-rotators (third row) and 18 distinct cores (bottom row). The halo properties are the virial cluster mass M_{vir}, the gas temperature T and the coolcoreness CC. The solid line represents the median value of property P and the error bars represent one standard deviation of the distribution of P within one class. The solid grey lines show the evolution of property P for one specific BCG.

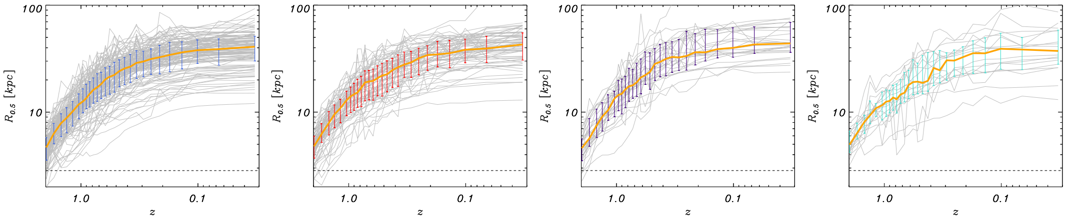

FIGURE 5.2: Temporal evolution of $R_{0.5}$ for (from left to right) 134 non-rotators, 69 regular-rotators, 29 prolate-rotators and 18 distinct cores. The solid line represents the median value of $R_{0.5}$ and the error bars represent one standard deviation of the distribution of $R_{0.5}$ within one class. The solid grey lines show the evolution of $R_{0.5}$ for one specific BCG. The dashed line marks the softening length of 2kpc/h.

Kinematical Properties

Fig. 5.3 shows the temporal evolution of selected kinematical properties for each of the kinematical type. All of these properties are calculated within one stellar half mass radius of the BCG. The evolution of the stellar half mass radius is displayed in Fig. 5.2. It can be seen that the median stellar half mass radius increases from around 5kpc at z=2 to roughly 40kpc at z=0. It is always well above the softening length.

The evolution of λ_R differs for each kinematical type. Throughout the entire redshift range the non-rotators are slowly rotating. The dashed line that marks the resolution limit of z=0 is likely an underestimate for the resolution limit of the entire redshift sample. However, the error bars have values of nearly 3.5 at z=2 and the median value is also slightly higher at this redshift. There are many peaks for individual galaxies that are probably experiencing mergers. The median λ_R of the regular rotating sample is slightly higher at z=2 but also generally very low. The main difference lies in the error bars that reach much higher values across the entire redshift range. Additionally, there are less peak values that reach above 0.6. The prolate rotating sample has a high median value at z=2 and scatters to even higher values. There are many peak values above 0.6 after z=1 especially considering the smaller sample size. The sample of BCGs with a kinematically distinct core at z=0 shows the highest median λ_R and scatter at z=2. It can be seen that the values decrease relatively unperturbed to lower λ_R in between redshift z=2 and z=1.3.

For all kinematical types, median h_3 is very close to $h_3 = 0$ for the entire redshift range. It can be seen that this parameter reacts very strongly to merger events. Nevertheless, 68% of the sample are always close to zero.

In contrast, median h_4 is increasing from values of around $h_4 = 0.015$ at z=2 up to around $h_4 = 0.045$ at z=0 with the exception of distinct core BCGs that fluctuate around $h_4 = 0.02$ during the investigated redshift range. The error bars follow the increasing median value. There are some events where h_4 peaks at large negative values for all kinematical classes except for the distinct cores.

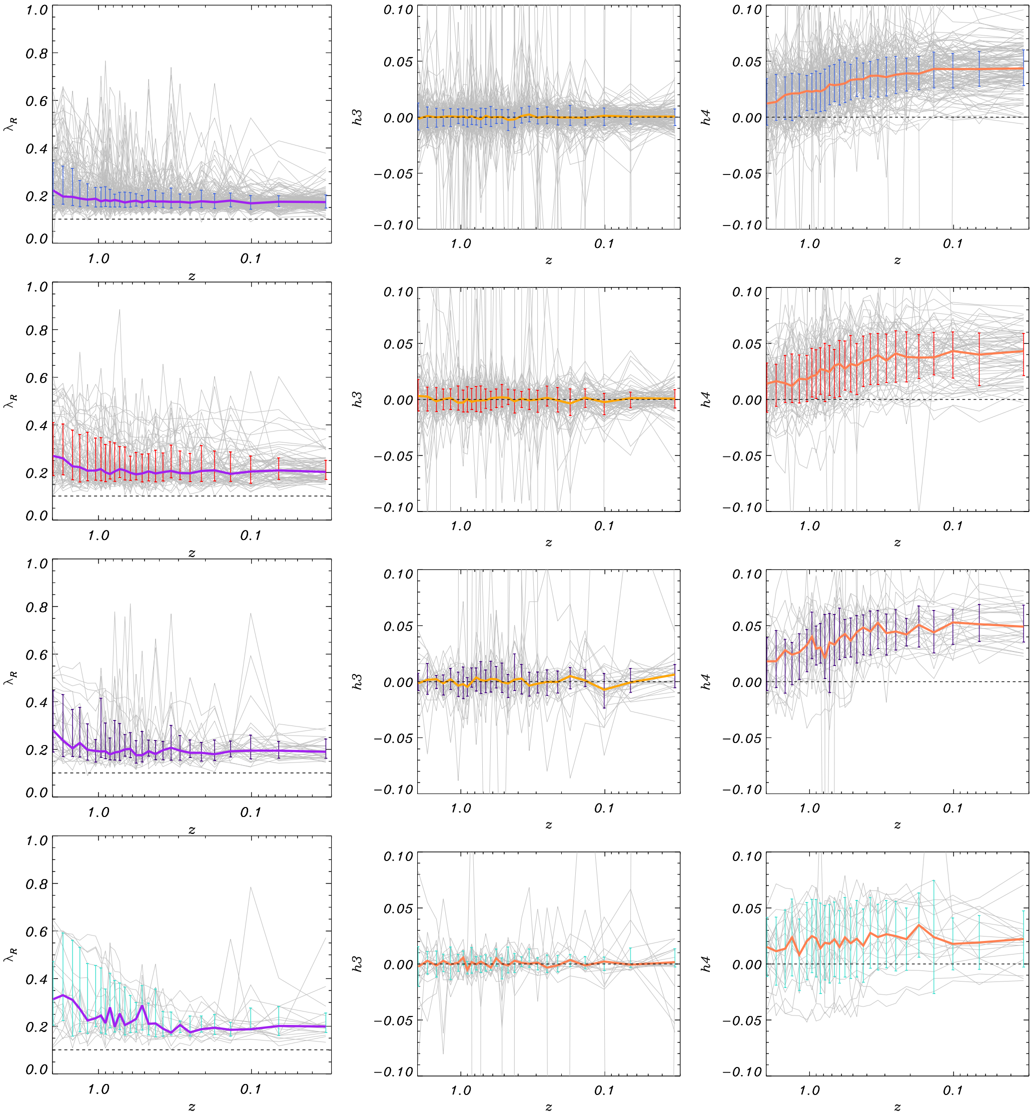

FIGURE 5.3: Temporal evolution of kinematical properties for each of the kinematical classes for 134 non-rotators (top row), 69 regular-rotators (second row), 29 prolate-rotators (third row) and 18 distinct cores (bottom row). The kinematical properties include the angular momentum proxy λ_R and the mean higher order moments of the line of sight velocity distribution $\overline{h_3}$ and $\overline{h_4}$. The solid line represents the median value of property P and the error bars represent one standard deviation of the distribution of P within one class.

BCG Properties

Fig. 5.4 shows the temporal evolution of global features of the BCG for each kinematical type.

Stellar masses of the BCG increase continually for each kinematical type. Non-rotators, regular rotators and prolate rotators start at around $5 \times 10^{11} M_{\odot}$ and reach median masses of about $2.5 \times 10^{12} M_{\odot}$. Distinct cores start at around 60% higher masses and reach masses that are factor of 2.5 higher. It is difficult to say if this is due to the smaller sample size with a bias for higher masses or if BCGs with a kinematically distinct core generally experience more stellar mass growth. Nevertheless, the final median mass difference is substantial given the rather small difference in initial stellar mass.

All four kinematical types experience a significant loss of specific star formation rate spanning roughly an entire order of magnitude across the investigated redshift range. The median values start at around $2 \times 10^{-10} 1/\mathrm{yr}$ and end up on specific star formation rates of about $2 \times 10^{-11} 1/\mathrm{yr}$. The decrease of specific star formation rate is expected because the peak of cosmic star formation density lies at z=2. For a review about cosmic star formation density see Moster (2013). It is surprising, however, that all four kinematical classes show a very similar evolution of specific star formation rate. This suggests that the kinematical patterns are mostly due to merger histories (ex-situ stellar mass) instead of star formation (in-situ stellar mass).

The b-value evolves differently for each kinematical type. For non-rotators it stays relatively constant at low values of around $b = -5.5$. The scatter is very large. Nevertheless, most of the NRs are classical ellipsoids for the entire redshift range. The median b of regular rotators is slightly higher at z=2 with $b = -5.3$ and increases to $b = -5.0$ at z=0. This is surprising since it is expected that ETGs cannot develop disk-like features especially if they are BCGs. The median b-value of the prolate rotating sample is significantly decreasing between z=2 and z=1. In the time following z=1 there are many peak values for b and the median b is increasing until it reaches a similar value to the beginning ($b = -5.2$). The sample of distinct cores starts at the highest value of $b = -5.1$. It is generally decreasing except for the last three data points. If all of the 24 data points at higher redshift would be interpolated the b-value would decrease to around $b = -5.5$. This would be roughly as low as the non-rotating sample.

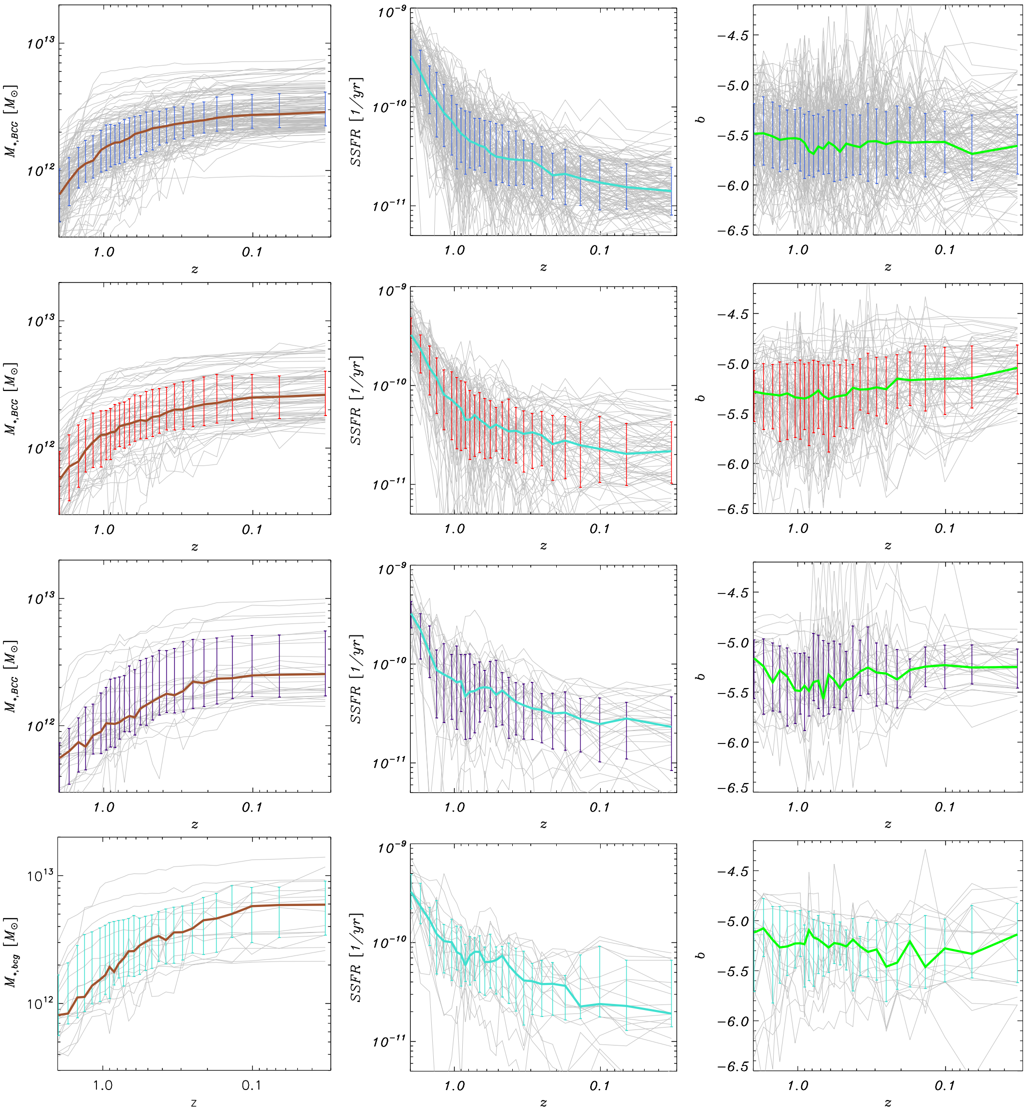

FIGURE 5.4: Temporal evolution of global galaxy properties for 134 non-rotators (top row), 69 regular-rotators (second row), 29 prolate-rotators (third row) and 18 distinct cores (bottom row). The global BCG properties include the stellar mass M_*, specific star formation rate SSFR and the morphological parameter b. The solid line represents the median value of property P and the error bars represent the standard deviation of the distribution of P within one class. The solid grey lines show the evolution of property P for one specific BCG.

Residual Properties

Fig. 5.4 shows the temporal evolution of residual properties for each kinematical type.

It can be seen that all BCGs inhibit super massive black holes with a median mass of around $2 \times 10^9 M_\odot$ at z=2 that increase their mass to about $1.5 \times 10^{10} M_\odot$ at z=0. The black hole growth does not seem to differ between the different kinematical types apart from the varying error bars that are expect due to the different sample sizes.

The fossilness differs significantly from cluster to cluster. All kinematical types show a huge scatter that almost spans two orders of magnitude. Nevertheless, some statistical features can be seen. The mass of the most massive satellite is generally double the mass at high redshift than the mass of the most massive satellite at z=0. Prolate rotators are in clusters with extraordinarily high fossilness up until around z=0.8.

There is also a general trend regarding the central stellar mass to total stellar mass fraction of the BCG. All four kinematical types build up most of their stellar mass in the ICL component after z=2. At z=2 the core comprises around 86% of the stellar mass whereas it is only responsible for around 65%. Distinct cores have the heaviest central masses with 69% and prolate rotators have the least massive cores with 64%. Furthermore, the ICL component of prolate rotating BCGs seems to grow rapidly up until z=0.5 with insignificant growth at lower redshift whereas the growth of stellar mass in the ICL seems more continuous for the other three kinematical types.

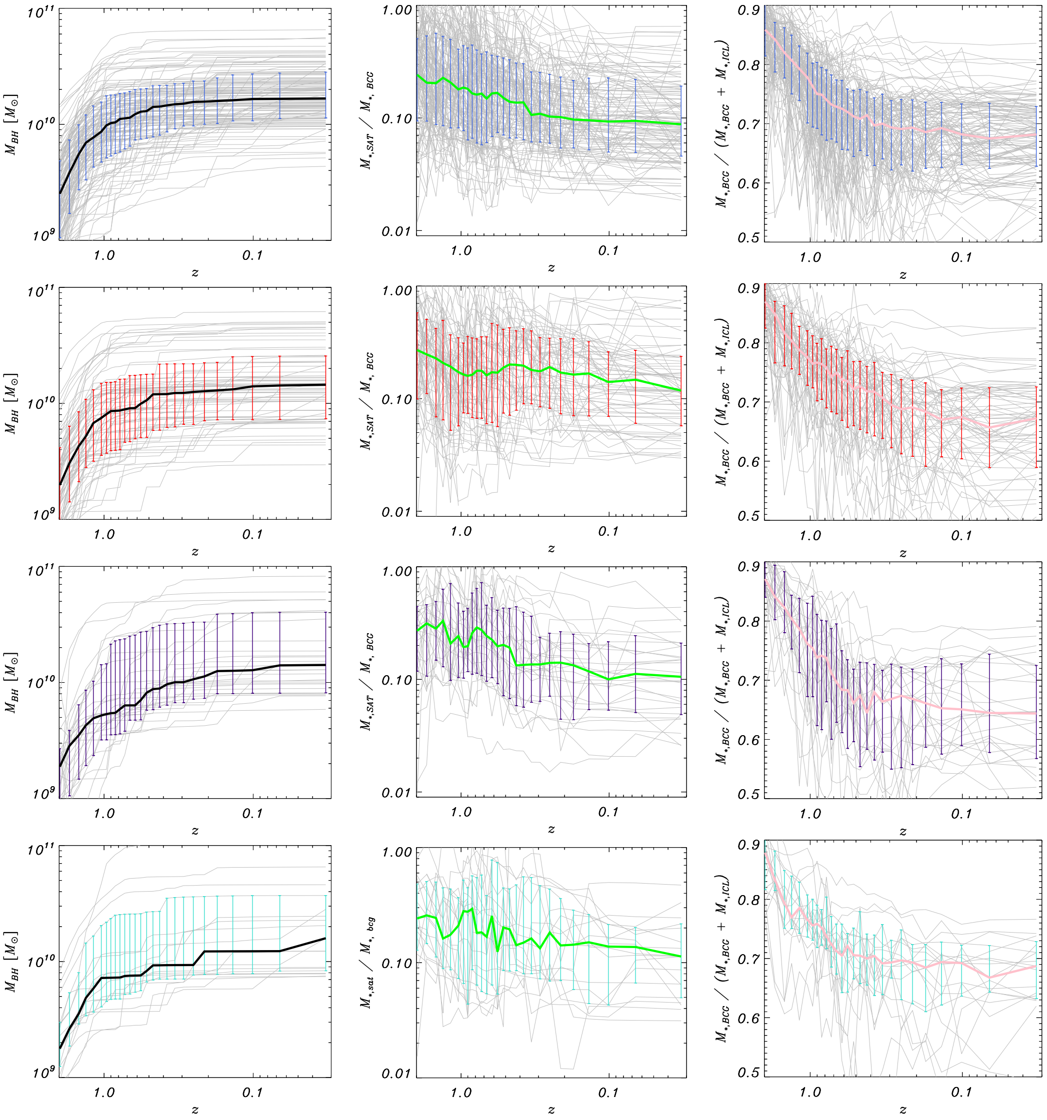

FIGURE 5.5: Temporal evolution of residual properties for 134 non-rotators (top row), 69 regular-rotators (second row), 29 prolate-rotators (third row) and 18 distinct cores (bottom row). The residual properties include the the black hole mass M_{BH}, fossilness $M_*^{\mathrm{sat}}/M_*^{\mathrm{cent}}$ and the central region stellar mass to total stellar mass ratio $M_{*,\mathrm{BCG}}/(M_{*,\mathrm{BCG}} + M_{*,\mathrm{ICL}})$. The solid line represents the median value of property P and the error bars represent one standard deviation of the distribution of P within one class. The solid grey lines show the evolution of property P for one specific BCG.

Summary

13 different environmental and kinematical properties were investigated statistically for a total of 250 BCGs. They show similar behaviour in the evolution of their virial halo mass, temperature and coolcoreness as far as the halo properties go. The mass of the central super massive black hole is also statistically growing similarly for all kinematical types. The BCGs show similar growth of stellar mass and stellar half mass radius. With the exception of BCGs with a distinct core that seem to experience a much stronger growth of stellar mass in the central region. This is underlined by the fact that the DCs show the highest central to ICL mass fraction of the four kinematical types.

This is where the differences begin and most of them seem to be connected with their respective merger history. Non-rotators are slowly rotating throughout the entire redshift range although they show significant peaks in the different kinematical properties that are signs of mergers. They have the lowest b-values and an intermediate evolution of fossilness and ICL growth. These BCGs seem to lie in the centre of clusters that were already very active well before z=2. They can still experience strong merger events but they seem stuck in a dead end. Regular rotators are up until this point a bit of a mystery. They show higher rotation and b-values at high redshift than their non-rotating counterparts. However, they are experiencing many merger events as well. One would generally expect that they should not be subject to merging in order to keep their rotation. It is even more interesting that they seem to build up a disk-like component that can be connected to rotation instead of losing it. The fossilness of their clusters and their ICL growth resembles that of non-rotators closely, however. Most prolate rotating BCGs seem to have experienced major merger events around z=1. They have relatively high λ_R at z=2 and strong peaks during the suspected merger phase. Subsequently they show a significant drop in b-value that later starts to increase again. One can suspect that it is possible for BCGs to build up rotation. Whereas regular rotating BCGs and prolate rotating BCGs differ in the fact that the latter experienced major merger events that lead to a switch of the rotational axis. Already before z=1 the prolate rotating sample shows the most massive ICL component. This might make it easier for the major merger to shift the rotation axis. BCGs with a distinct core at z=0 might experience a vastly different merger history. They slowly decrease their λ_R and b-value and slowly increase their ICL component. They also showed few peaks in the kinematical plots even when taking the smaller sample size into account. One could suspect that the core remains relatively unperturbed and keeps its rotation and a non rotating 'shell' slowly builds up around the core. This is investigated in more detail in Felix Schulze, Remus, Klaus Dolag, et al. (2020).

Although the detailed mechanisms are mere speculation it is clear that the kinematics and some of the global BCG properties that are connected to the distribution of stellar mass are influenced by mergers. The specific star formation rate is evolving very similar for each kinematical type and therefore in-situ star formation seems to play a minor role. However, the higher order moments are behaving very interestingly. First of all, it is important to mention that the median h_3 parameter does not change with redshift at all for any of the kinematical types. This behaviour is expected for axis-symmetric galaxies in equilibrium. This find makes this property less interesting for the following investigation of scaling relations. In contrast, the h_4 parameter changes drastically over time. The overall increasing behaviour for each of the kinematical classes is unlikely to find its cause in their merger history. Therefore it is more reasonable to believe that this parameter might somehow be connected to environmental properties of the BCG. Before any speculations can be made the scaling with different properties has to be investigated in more detail. It would be interesting to see if an increasing h_4 is found in non-BCG galaxies as well. If low values of h_4 are protected in the centre of BCGs this might explain why the lowest values for all classes except the distinct cores were found at z=0. Unfortunately the resolution of the simulation does not suffice to study the evolution of h_4 in the very centre of the BCG.

There also needs to be a more detailed investigation of the coolcoreness. Although no specific behaviour could be found for any of the kinematical classes with respect to coolcoreness, it is an interesting result that *all* BCGs seem to experience a cool core phase around z=2 whereas some stay cool core and others develop a non-cool core leading to a scatter that encompasses all possible fractions of coolcoreness.

5.2 Individual Evolution

This is a case study of the evolution of kinematics and environmental properties for individual galaxies. The goal is to examine how different properties evolve with *each other* in detail. First the evolution of the four poster child galaxies that were introduced in section 2.3 will be shown. For these galaxies we already saw that the kinematical features are well resolved. We will see that the cool core of their galaxy cluster evolves differently. To really understand what drives the development of a non-cool core a sample will be investigated that is comprised by eight BCGs: four of which keep their cool core and four BCGs for whom the cool core of their cluster turns into a non-cool core. Some of the features I will describe are hard to see on the printed document. Unfortunately it is not possible to squash everything into one larger plot and unfeasible to extend everything over forty pages. If there is interest in the details please refer to the digital version of this thesis.

5.2.1 Epeisodia II: Poster Child Galaxies

Time is not explicitly illustrated in the following plots. It is symbolised with a line that starts at the first data point at z=2 (indicated with a cross) and connects the following 27 data points with different Δz until it reaches z=0 (indicated with the respective symbol of the kinematical group). Every available data point is colour-coded with the respective coolcoreness the core has at that time. For each of the following galaxies there are two main plots. On the left side masses and derivatives thereof are set into relation. Namely the halo virial mass M_{vir} versus the BCG stellar mass within $10\% R_{\mathrm{vir}}$ $M_{*,BCG}$. This gives an overview of the general accretion of these systems. The second panel shows the relationship between the BCG stellar mass $M_{*,BCG}$ and the fossilness $M_{*,\mathrm{SAT}}/M_{*,\mathrm{BCG}}$. This relation helps to find the sources of major accretion. If there is e.g. a major merger the value of the fossilness will be close to 1 and quickly decrease leading to a quick increase in stellar BCG mass that is equivalent to the mass of the stellar mass of the satellite. The final panel shows the stellar mass distribution between the central region and the ICL $M_{*,\mathrm{BCG}}/(M_{*,\mathrm{BCG}} + M_{*,\mathrm{ICL}})$. This relation helps to figure out where the newly accreted mass is distributed. The relation increases if stellar mass sinks into or is formed in the centre and decreases if more stellar mass remains in the ICL. The right page sets the two kinematical properties λ_R and h_4 in relation to four environmental properties: the specific star formation rate SSFR, the *dynamical* mass of the black hole M_{BH}, the gas temperature within one virial radius T and the b-value.

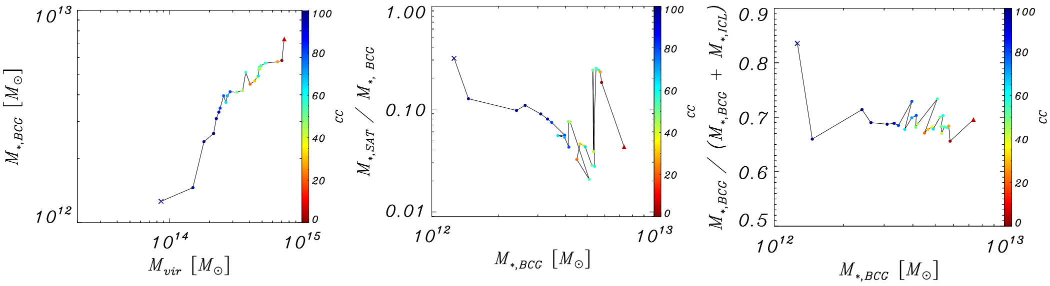

FIGURE 5.6: Evolution of stellar masses in different regions. *Left:* Virial halo mass $M_{\rm vir}$ versus stellar BCG mass $M_{*,\rm BCG}$, *middle:* $M_{*,\rm BCG}$ versus fossilness $M_{*,\rm SAT}/M_{*,\rm BCG}$, *right:* fraction of stellar BCG mass to total stellar mass $M_{*,\rm BCG}/(M_{*,\rm BCG}+M_{*,\rm ICL})$. A detailed description can be found at the beginning of this section.

Non-Rotator

From Fig. 5.6 it can be seen that there are no major merger events for this galaxy. There are several minor merger events, however. Surprisingly, the stellar mass within $10\%R_{\rm vir}$ is decreasing at two of these points. It could be that during the fly through some of the stellar particles are attributed to the wrong subhalo. The BCG to ICL mass fraction is constantly fluctuating between 0.65 and 0.75 and the core turns slowly from being a cool core to being a non-cool core.
The specific star formation rate is globally decreasing and fluctuating when the minor mergers happen. λ_R is generally low - already at z=2. It is interesting to note that λ_R was first increasing but decreased during the minor mergers with the exception of the one peak where a mismatching is likely. The opposite behaviour can be observed for h_4. During the cool core period this parameter decreases. During and after the minor mergers it increases and reaches one of the highest values at z=0. The black hole is strongly accreting during the cool core period. After the minor merger events it is only accreting rarely and is not accreting at all for a while before z=0. It can be seen that h_4 is decreasing with increasing $M_{\rm BH}$ and over all increasing when the black hole stopped accreting. The gas temperature is increasing during the cool core phase, fluctuating during the minor mergers and increases again by 25% immediately before z=0. There the increasing temperature phase at the beginning h_4 is falling, during the increasing temperature phase t the end h_4 is rising. The b-value is fluctuating between $-5.7 < b < -5.0$ with the exception of the aforementioned outlier data point.

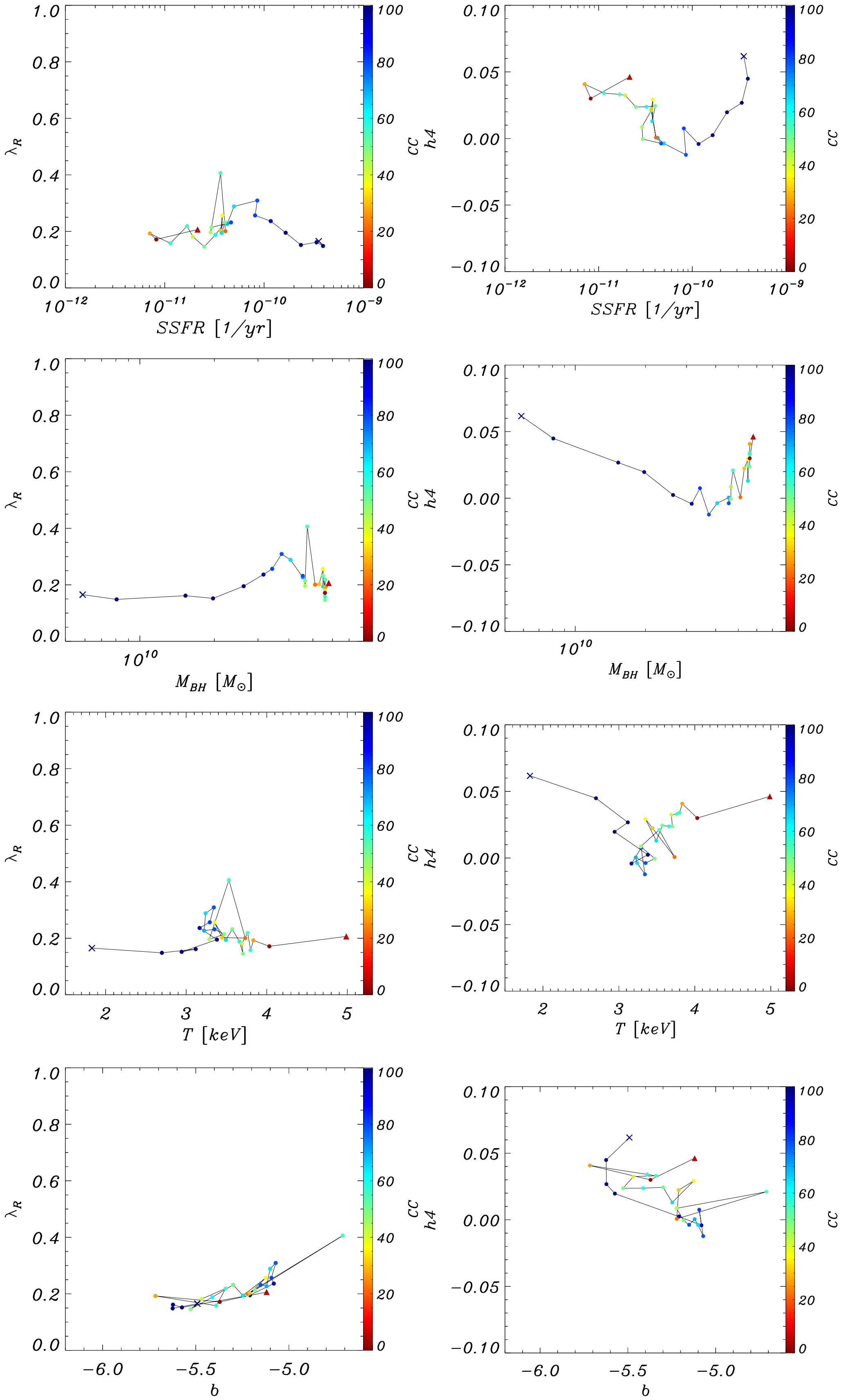

FIGURE 5.7: Relationship between kinematical properties λ_R, h_4 and environmental properties: specific star formation rate SSFR, black hole mass m_{BH}, gas temperature T and b-value. A detailed description can be found at the beginning of this section.

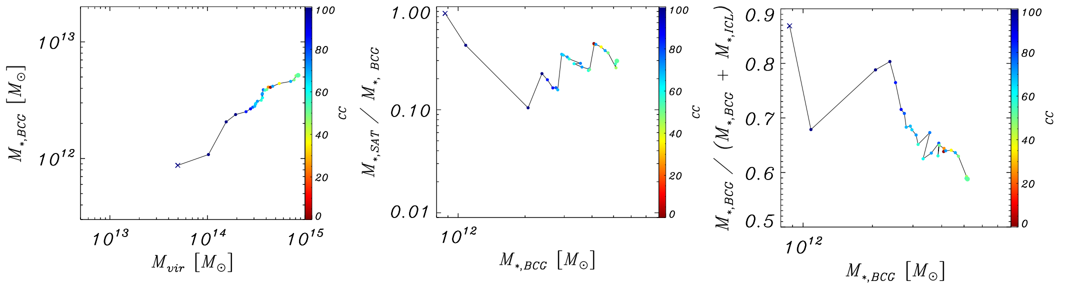

FIGURE 5.8: Evolution of stellar masses in different regions. *Left:* Virial halo mass M_{vir} versus stellar BCG mass $M_{*,\text{BCG}}$, *middle:* $M_{*,\text{BCG}}$ versus fossilness $M_{*,\text{SAT}}/M_{*,\text{BCG}}$, *right:* fraction of stellar BCG mass to total stellar mass $M_{*,\text{BCG}}/(M_{*,\text{BCG}} + M_{*,\text{ICL}})$. A detailed description can be found at the beginning of this section.

Regular Rotator

The merger history is easier to read for this BCG. In Fig. 5.8 we see that its stellar mass is increasing from around $10^{12}M_\odot$ to slightly above $5 \times 10^{12}M_\odot$. It is always accompanied by a satellite with at least 10% of its mass. During z=2 it seems like this BCG experiences a major merger followed by at least two minor mergers. The BCG has a massive central region after the major mergers but builds up a massive ICL component subsequently. The BCG always has a cool core (strong cool core at z=2 and weak cool core at z=0) with the exception of three data points.

It seems that the major merger was dry because the specific star formation rate did not increase significantly. There are some instances of increased SSFR during the minor mergers. Generally, the specific star formation rate decreases by one order of magnitude therefore it follows the median of its kinematical group closely. λ_R is always very low at values of around $\lambda_R = 0.2$ only increasing slightly during minor mergers. In contrast to the non-rotator BCG h_4 stays very constant at values of around 0.025 slightly after z=2 all the way to z=0. The behaviour of the black hole is very similar to the black hole of the BCG above. Except for the fact that the black hole is not accreting even though the core is rather cool. The behaviour of the temperature is also very similar with an increasing period for high redshift, fluctuating during intermediate redshift, followed by an increasing period again before z=0. Interestingly the b-value is increasing to $b = -5.2$ from when it reached its minimum of -6.2 right after the major merger. It is very interesting that for decreasing b-value over time no correlation with λ_R nor h_4 can be observed.

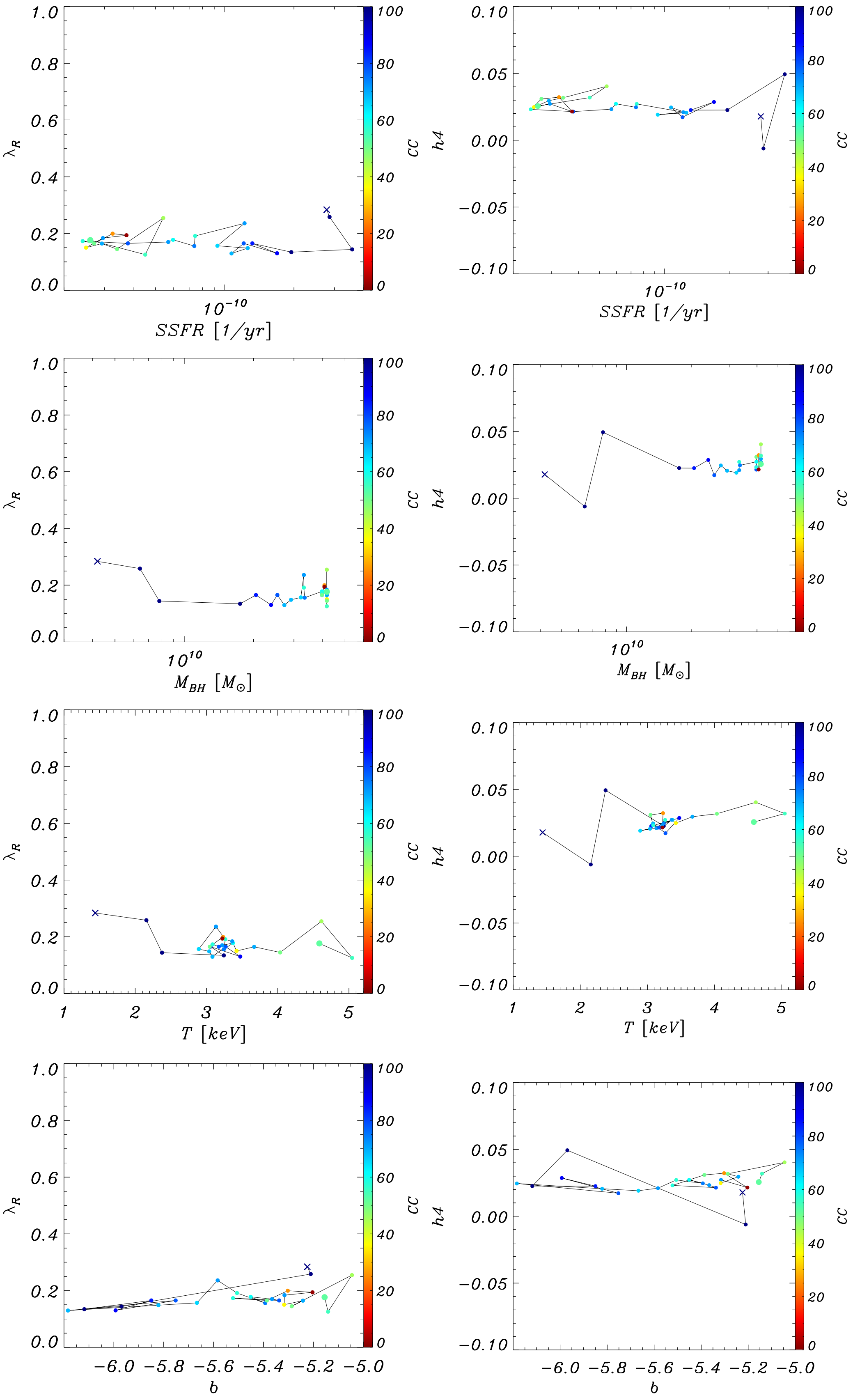

FIGURE 5.9: Relationship between kinematical properties λ_R, h_4 and environmental properties: specific star formation rate SSFR, black hole mass m_{BH}, gas temperature T and b-value. A detailed description can be found at the beginning of this section.

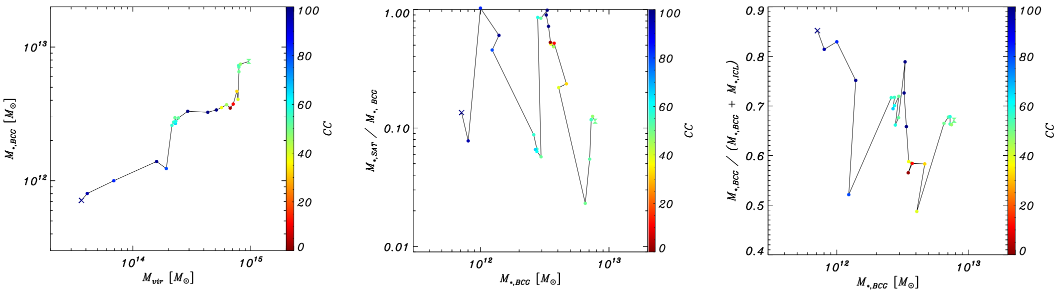

FIGURE 5.10: Evolution of stellar masses in different regions. *Left:* Virial halo mass M_{vir} versus stellar BCG mass $M_{*,\text{BCG}}$, *middle:* $M_{*,\text{BCG}}$ versus fossilness $M_{*,\text{SAT}}/M_{*,\text{BCG}}$, *right:* fraction of stellar BCG mass to total stellar mass $M_{*,\text{BCG}}/(M_{*,\text{BCG}} + M_{*,\text{ICL}})$. A detailed description can be found at the beginning of this section.

Prolate Rotator

It can be seen from Fig. 5.10 that the BCG had two major events of accretion. First, at a stellar BCG mass of $M_{*,\text{BCG}} = 10^{12} M_\odot$ and at $M_{*,\text{BCG}} = 4 \times 10^{12} M_\odot$. The accretion can be seen as steep slopes in the the left plot. Before the accretion happens, the mass of the ICL increases drastically as can be seen in the right plot. The first sign of a merger, however, is already visible for the third data point in the fossilness plot. The value of $M_{*,\text{SAT}}/M_{*,\text{BCG}} = 1$ indicates that the BCG experienced two equal mass major mergers. It seems that the coolcoreness decreases after the merger event to values of around CC$= 60\%$. The BCG has a cool-core in periods of low accretion with the exception of being a non-cool core shortly before the second merger.

The relationship between kinematical properties and environmental properties can be seen in Fig. 5.11. As expected from the statistical plots in the previous section, the star formation rate is generally decreasing. After the first merger, the star formation rate is increased shortly for a factor of two, indicating a gaseous merger. The second merger does not increase the star formation rate and therefore seems to have been a dry merger. The gaseous merger increases λ_R slightly, the dry merger increases λ_R by a factor of two. For most of the time the BCG is slowly rotating. As expected, h_4 is generally increasing with the exception of the cool core phase between the first and second merger where it reaches its minimum values. This is right after the black hole starts accreting again after a longer period of no accretion. After the second merger, the black hole is not accreting as well. During those times the gas temperature is stagnant, increasing primarily when there is a cool-core. h_4 is constantly low when the temperature increases and changes heavily when the temperature is not increasing. The b-value is fluctuating very heavily during the entire time. There is the impression that it is lower if there is a cool-core.

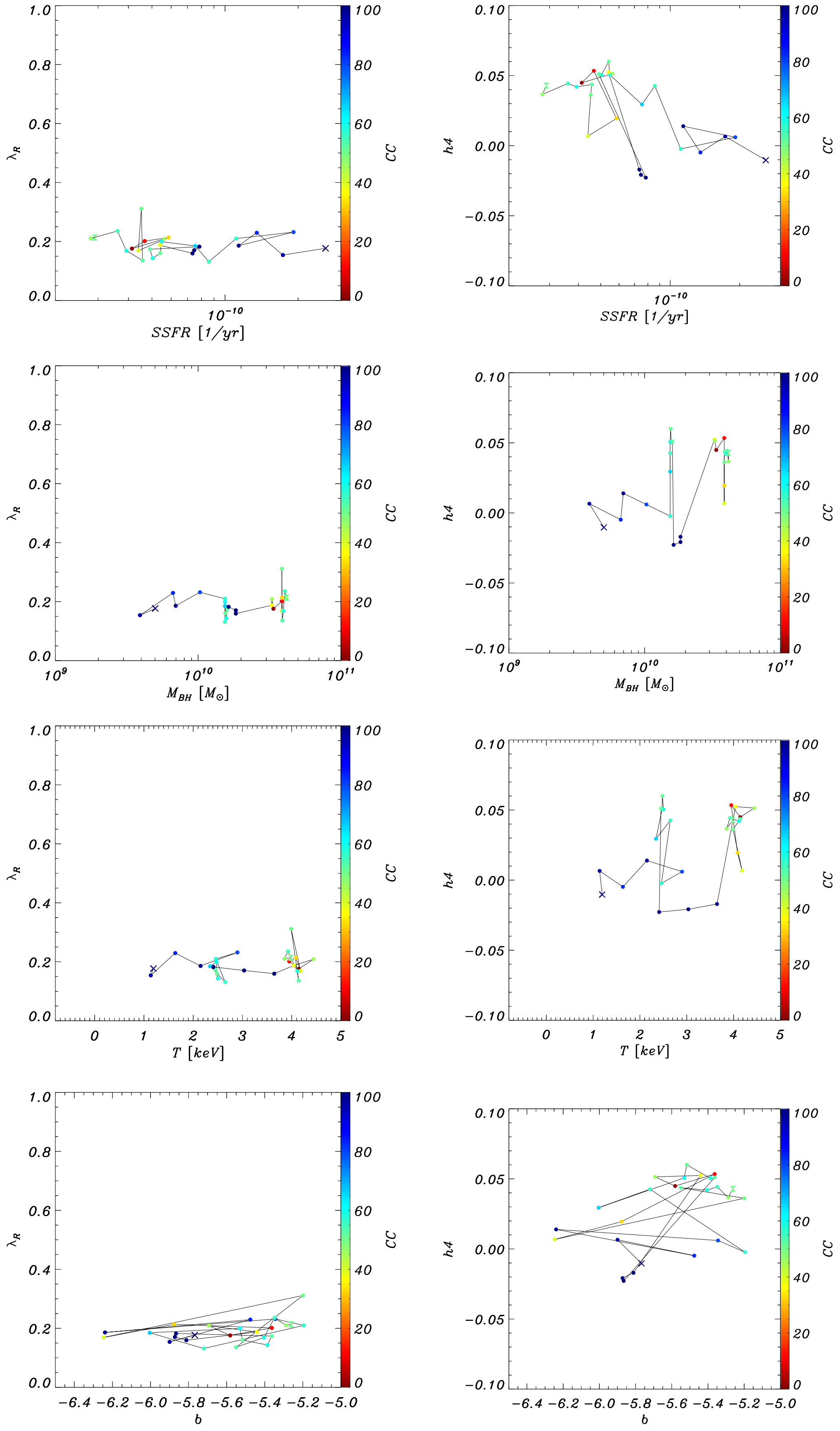

FIGURE 5.11: Relationship between kinematical properties λ_R, h_4 and environmental properties: specific star formation rate SSFR, black hole mass m_{BH}, gas temperature T and b-value. A detailed description can be found at the beginning of this section.

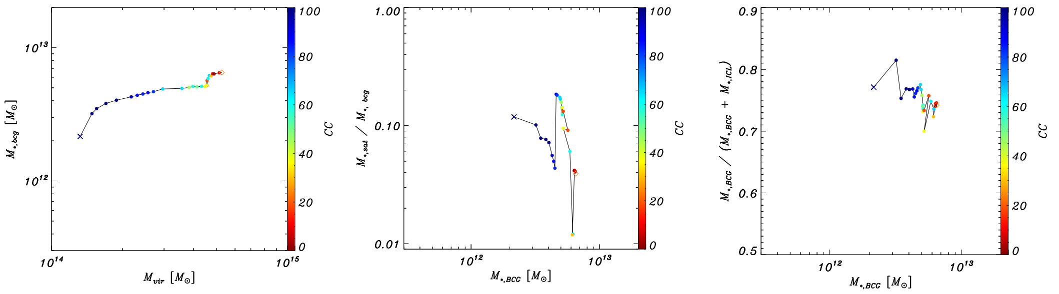

FIGURE 5.12: Evolution of stellar masses in different regions. *Left:* Virial halo mass M_{vir} versus stellar BCG mass $M_{*,\mathrm{BCG}}$, *middle:* $M_{*,\mathrm{BCG}}$ versus fossilness $M_{*,\mathrm{SAT}}/M_{*,\mathrm{BCG}}$, *right:* fraction of stellar BCG mass to total stellar mass $M_{*,\mathrm{BCG}}/(M_{*,\mathrm{BCG}} + M_{*,\mathrm{ICL}})$. A detailed description can be found at the beginning of this section.

Distinct Core

This BCG builds up mass very slowly and peaceful, with the exception of a slightly stronger accretion at low redshift with at a mass of around $M_{*,\mathrm{BCG}} = 5 \times 10^{12} M_{\odot}$. A massive satellite with around 20% of the BCGs mass formed when the halo still had a cool-core as can be seen from the fossilness plot. The merger happened later when the satellite had around 10% of the BCGs mass, thus being a minor merger. From the point when the massive satellite formed on the core became less and less cool.
The star formation history of this BCG spans almost two orders of magnitude. Being comparably highly star forming at z=2 with SSFR= $7 \times 10^{10} 1/\mathrm{yr}$ it is constantly decreasing up to a very low star formation rate of SSFR= $1 \times 10^{-11}/\mathrm{yr}$ at z=0 with the exception of some increased star formation fuelled by the minor merger. The BCG is highly rotating at z=2 with $\lambda_R = 0.6$ and constantly loses angular momentum within one half mass radius. The evolution of h_4 is rather surprising with negative values throughout its evolution except for the first data point. The first data point of this BCG is difficult to interpret, it could be an indicator of a merger event shortly before z=2 or it could simply be unreliable. In lack of more information this data point will be ignored for this discussion. During the time the cluster inhibits a cool core h_4 is decreasing and increasing after the core turned non-cool. It can be seen that the black hole is constantly accreting during the time the cluster has a cool core and only comes to a halt at times of a non-cool core. This coincides with the minor merger. During this phase h_4 is increasing. The cluster has a very high gas temperature around 3keV from early on. During the early cool-core phase it is still increasing. Once this phase ends it drops back to slightly above 3keV and is fluctuating between 3keV and 4keV from thereon. There is a clear correlation between b-value and λ_R and an anti-correlation between b-value and h_4.

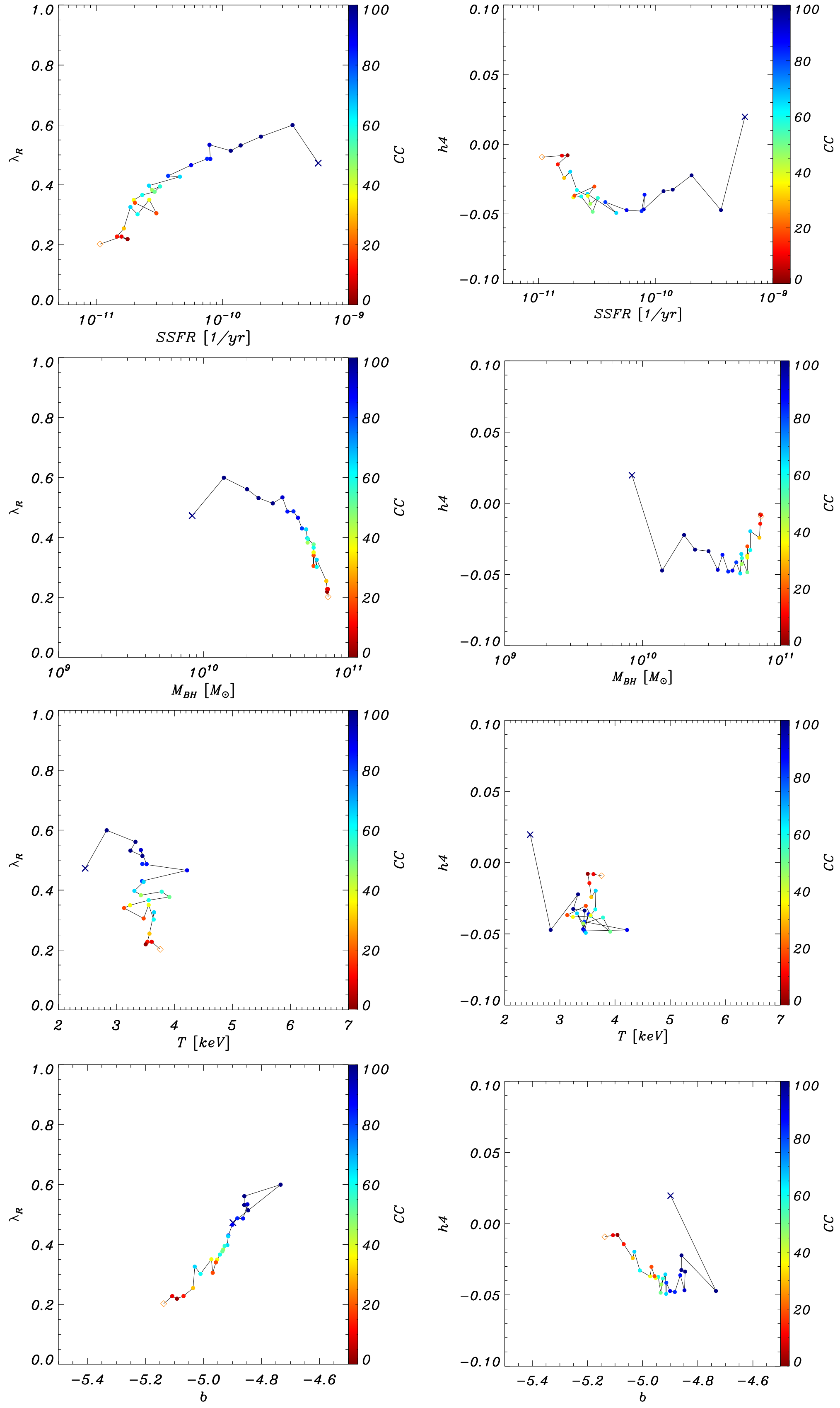

FIGURE 5.13: Relationship between kinematical properties λ_R, h_4 and environmental properties: specific star formation rate SSFR, black hole mass m_{BH}, gas temperature T and b-value. A detailed description can be found at the beginning of this section.

Summary

This sample of four BCGs whose kinematical maps were already presented in Fig. 3.10 span a wide range of merger histories, kinematics, environmental properties and their respective evolutions. The descriptions above show that there is a multitude of ways these properties can interact with each other if they interact at all. I want to point out that it would have been possible to describe and interpret each of the previous plots on several pages. I tried to focus on the things that were most striking to me and that help me to answer the main question of this thesis, namely the influence of environment on the stellar kinematics of BCGs. This summary highlights the similarities and differences between the four BCGs in that regard.

The most violent environment is around the prolate rotator which experienced two major mergers, an early wet merger and a later prolonged dry merger. The regular rotator also experienced many mergers. A dry major merger at z=2 and multiple minor mergers with some gas. The non-rotator did not experience any major mergers but rather 2 minor mergers and the distinct core might have experienced a major merger shortly before z=2 but remained rather undisturbed since with only one minor merger.

The ICL mass peaks right after mergers. It is important to note that within the context of a numerical simulation this could mean that the two systems have merged but the stars of the satellite need some time to sink into the central region of the BCG. The fraction between central mass and ICL mass can also change if there are no mergers. It is fluctuating for all four BCGs (possibly showing minor and mini mergers with less massive satellites) and slightly increasing for the distinct core.

The NR, RR and PR were already slow rotators at z=2 and generally stayed slowly rotating since. The DC was fast rotating with steadily decreasing λ_R. This could be an indicator that the non-rotating outer regions formed around the always fast rotating central region due to constant accretion.

The evolution of h_4 is more complex. The NR and the DC show that during the initial cool core phase h_4 is decreasing but starts increasing once the core starts turning into a non-cool core. Both of these BCGs span a wide range of specific star formation rate of around two orders of magnitude because they receive only small amounts of gas through mergers. The RR and PR do not show the opposite but they do not show the same behaviour either. PR has low values in h_4 during cool core phases but is generally increasing. h_4 of RR is neither increasing nor decreasing but rather stays constant at higher h_4 values. Both of these BCGs receive significant amounts of gas through mergers and therefore the specific star formation rate decreases only by one order of magnitude.

The black holes of all four BCGs are strongly accreting during the initial cool core phase and only the black hole of the DC keeps on accreting, reaching roughly twice the mass of the others. This is the BCG whose ICL component is generally increasing. The accretion of the black hole of PR stops during the major mergers. This coincides with a less cool core. The accretion starts again when there is a cool core. This behaviour is similar for NR and RR in the regard that the black hole is not accreting during their respective minor mergers.

The distinct core has a high initial temperature that does not have an increasing behaviour. The temperature of the other BCGs increase from around half the initial value of the DC to 3 (NR), 4 (PR), 5 (RR) times their own initial temperature. The NR and the RR have a phase of stagnant temperature at intermediate temperatures that cannot be connected to black hole growth or coolcoreness at first glance. The temperature of the PR is increasing when the black hole is accreting and stagnant when the black hole is not accreting.

The behaviour of the *b*-value is entirely different for each of the four BCGs. It is increasing after the early major merger of RR without much scatter. The *b*-values of the DC also do not show much fluctuations but are decreasing. They show a clear correlation with λ_R and an anti-correlation with h_4. The *b*-values of NR and PR are fluctuating heavily between a smaller range $-5.7 < b < -5.0$ for the NR and a large range $-6.2 < b < -5.0$ for the PR.

Every galaxy ends up showing vastly different kinematical patterns than the others. Therefore, it is expected that they show different evolutions of their kinematical properties. We saw that their environmental properties evolve differently as well. Which of these properties is tied to their kinematical evolution and which are independent? Two of these BCGs ended up with a cool core and two had a non-cool core at z=0. From the statistical examination we know that the chance of a cool core at z=0 is roughly the same for all four kinematical types. Therefore it seems that there is no direct influence between these properties. The following section will present two BCGs for each kinematical type with one of which ending up having a cool core and the other with a non-cool core. Through this separation the similarities should give a hint at what drives the kinematical evolution and the differences should indicate what drives the development of a non-cool core.

5.2.2 Epeisodia III: Cool Core and non-Cool Core Evolution

The following plots show the same properties as before for eight different BCGs: two of each kinematical type. The BCGs were selected such that their coolcoreness is either above 90% or below 10% at redshift zero, i.e. being a strong cool and non-cool core respectively. Only a few of the classified galaxies fulfil these strict criteria. Finally, the BCGs presented here were selected such that they have similar masses at z=0.

The plots can be read similarly to before. The evolution starts at z=0 marked with a cross and ends at z=0 marked with the symbol of the kinematical type the BCG has by then. The data points that belong to the BCG that has a cool core at z=0 are sorted by redshift and connected with a blue line. The data points that belong to the BCG that has a non-cool core at z=0 are sorted by redshift as well and connected with a red line. In the following I will call the first *C* and the latter *N*.

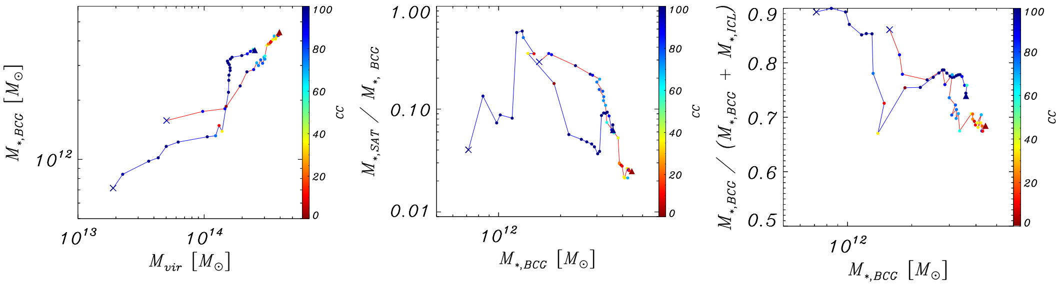

FIGURE 5.14: Evolution of stellar masses in different regions. *Left:* Virial halo mass M_{vir} versus stellar BCG mass $M_{*,\text{BCG}}$, *middle:* $M_{*,\text{BCG}}$ versus fossilness $M_{*,\text{SAT}}/M_{*,\text{BCG}}$, *right:* fraction of stellar BCG mass to total stellar mass $M_{*,\text{BCG}}/(M_{*,\text{BCG}} + M_{*,\text{ICL}})$. A detailed description can be found at the beginning of this section.

Non-Rotators

Fig. 5.14 shows two BCGs that both show a non-rotating pattern at z=0. The main difference we can see from this plot is that C experiences a major merger before it reaches the initial mass of N followed by rapid accretion. N does not seem to experience mergers with comparable masses whatsoever. Although C experiences multiple minor mergers around z=0. Generally, both BCGs show a growing ICL component. The growth of Cs ICL is disrupted during its major merger.
Fig. 5.15 shows how the kinematical properties λ_R and h_4 evolve with environmental properties. It can be seen that λ_R is very low all across the observed redshift range for both BCGs with the exception of Cs major merger. The evolution of h_4 however differs significantly. For N h_4 is continually increasing whereas for C it increases significantly during the merger but is generally decreasing instead. The specific star formation rate of C decreases by over one order of magnitude even though it received significant gas supply during the wet merger leading to a rise of SSFR by a factor of two. It loses SSFR after the major merger rapidly. The SSFR of N at z=0 is less than an order of magnitude smaller than its SSFR at z=2. This is because it increases its SSFR at high redshift during the minor mergers and only decreases slowly as it approaches values less than $10^{-11}1/\text{yr}$. The black holes of these two BCGs are very different. Although the stellar mass of N is only around 30% larger than Cs stellar mass at z=0 their black hole masses differ by more than a factor of 10! This is due to the fact that Cs black hole is almost not accreting any mass but the BH of N is increasing its mass by almost a factor of six. Interestingly enough C has a cool core almost the entire time but Ns black hole is mainly accreting during the time it has a BH. For N it seems like there is a correlation between black hole growth and h_4. Both BCGs increase their gas temperature at high redshift followed by stagnation and fluctuation at intermediate to low redshift. The final temperature of C is lower than Ns initial temperature. Both BCGs show strong fluctuations in b-value between $-6.4 < b < -5.6$. Both of these BCGs show very similar kinematics and morphology (being NR, low rotation, fluctuating b-value, increasing ICL) despite being very different when it comes to environmental properties. However the h_4 parameter shows opposite behaviour for N (generally increasing) and C (generally decreasing).

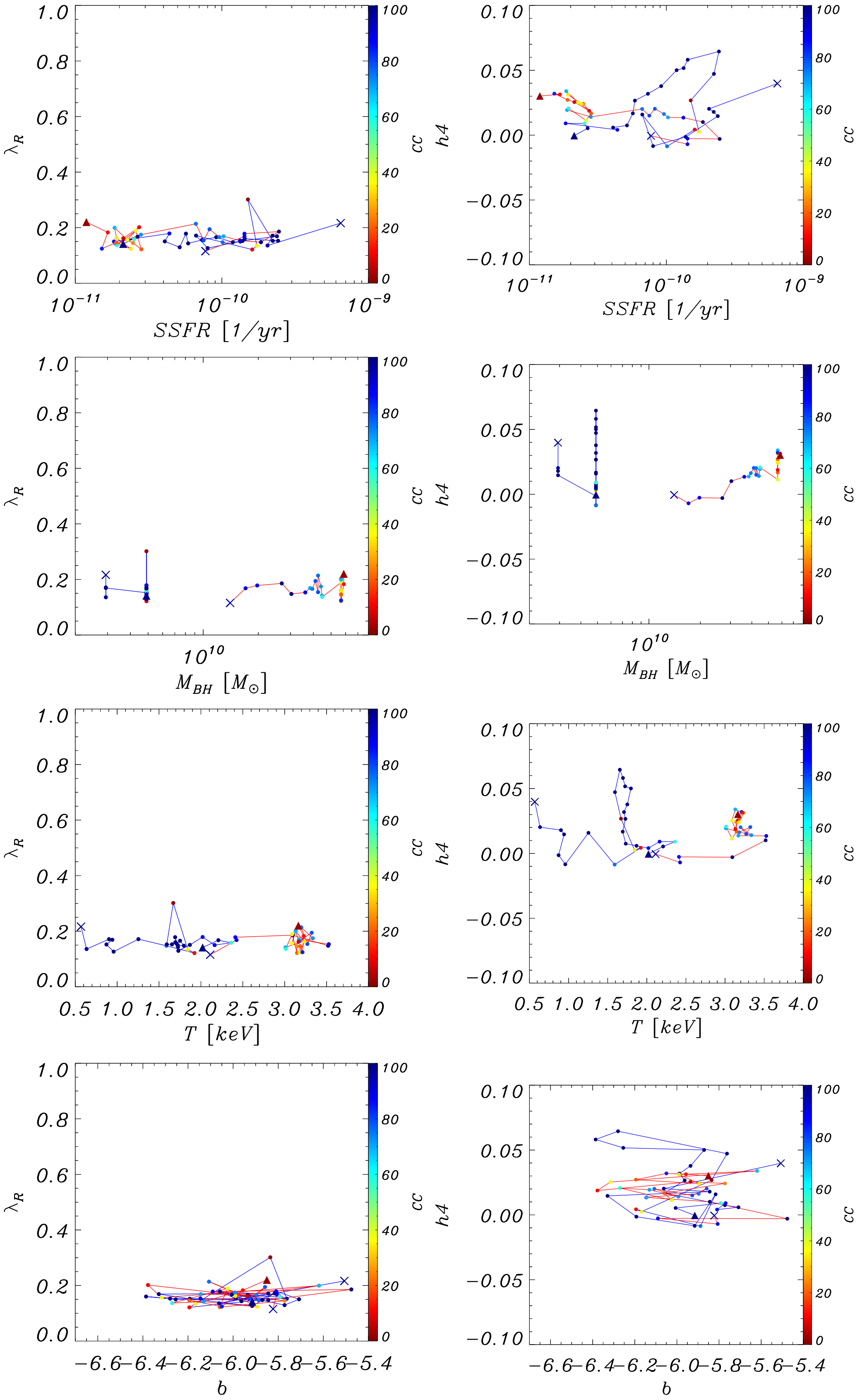

FIGURE 5.15: Relationship between kinematical properties λ_R, h_4 and environmental properties: specific star formation rate SSFR, black hole mass m_{BH}, gas temperature T and b-value. A detailed description can be found at the beginning of this section.

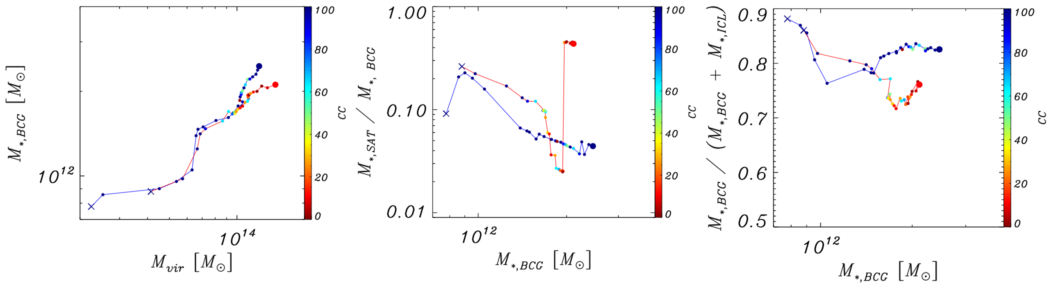

FIGURE 5.16: Evolution of masses in the same regions as before. A detailed description can be found at the beginning of this section.

Regular Rotators

The merger history of these two BCGs are rather similar. C seems to have experienced a 1:2 merger at high redshift although the most massive satellite was not massive enough to deliver all this mass by itself so there could be a lot of in-situ star formation as well. From thereon C is slowly building up stellar mass that is mostly confined to the inner regions of the BCG. N is also slowly building up mass with some minor mergers at high redshift. It strikes that at lower redshift a massive satellite is introduced in the system. The origin of this satellite would be based on speculation. Since it does not seem like it had yet the chance to interact with the BCG, I will refrain from doing so. At high redshift Ns ICL is increasingly more dominant but starts decreasing with respect to the central region at intermediate redshift. The two BCGs show different behaviour in both λ_R and h_4. N starts at relatively high λ_R which continually decreases, whereas C is always rather slowly rotating with some increase at lower redshift. In h_4 we can see that (as before) h_4 is generally decreasing for C and generally increasing for N. Both of these BCGs start with similar SSFR although the specific star formation rate of C at z=0 is almost a factor of six higher than that of N. C seems to have a large enough gas reservoir or gas supply that it can form stars at a specific rate of $10^{-10}1/\text{yr}$ for a long time whereas Ns SSFR quickly goes below $10^{-11}1/\text{yr}$. There is one outlier point at very low SSFR that is hard to explain because no counter part can be found in any of the other panels. The black hole masses behave very differently as well. Both start at similar masses but Ns black hole is continually accreting until it has twice the mass of Cs black hole at redshift zero. Nevertheless, the BH of C experiences a phase of major accretion when it almost doubles its mass. This happens shortly before the disruption of the cool core for one data point but the core recovers quickly with only few data points at lower coolcoreness. N has roughly twice Cs initial temperature. Both increase their temperatures at very high and very low redshift and are fluctuating in between. Surprisingly, the BCGs show very different behaviour in b-value. C reaches values as low as $b = -5.8$ but is increasing from thereon such that it forms a correlation with λ_R. There is a b-value λ_R correlation for C as well but it is much steeper. But it *starts* at high b-value and λ_R. Similarly for b and h_4: There is an anti correlation for most of the data points. However, their correlations have to be read in opposite directions. Despite the fact that both are BCGs, have very similar mass evolution and are regular rotating at redshift zero they seem to have more differences than what they have in common. Their star formation, BH mass and temperatures evolve differently and are partially therefore in different regimes. Their kinematics seem similar at first glance but differ significantly on further inspection.

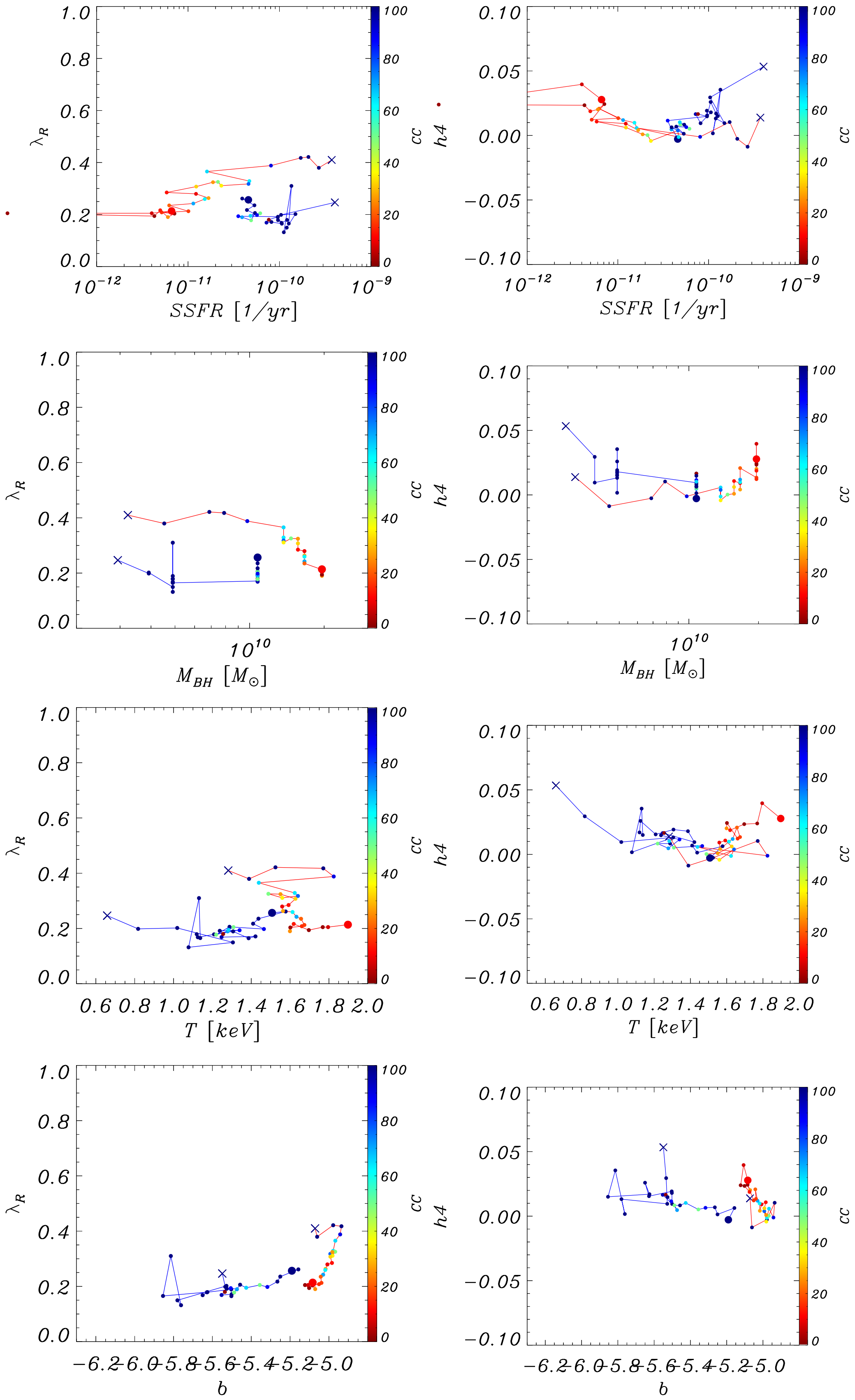

FIGURE 5.17: Relationship between kinematical properties λ_R, h_4 and environmental properties: specific star formation rate SSFR, black hole mass m_{BH}, gas temperature T and b-value. A detailed description can be found at the beginning of this section.

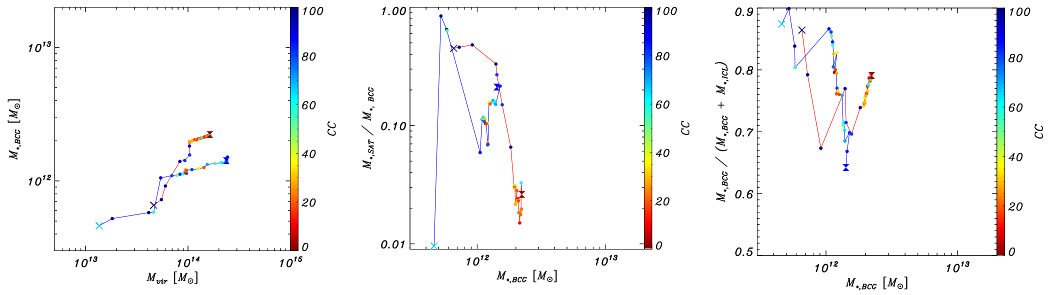

FIGURE 5.18: Evolution of masses in the same regions as before. A detailed description can be found at the beginning of this section.

Prolate Rotators

Both of these BCGs are prolate rotating at z=0 however one keeps its cool core and the other develops a non-cool core. The BCGs start with similar masses although N has roughly twice Cs mass at z=0. Both BCGs experience a major merger early on, whereas Cs merger happens very quickly and N experiences a prolonged accretion phase. After their respective major merger phases their mass distribution evolves contrary to each other. C builds up a massive stellar ICL component whereas N contains most of its stellar mass within 10%R_{vir}. C has a satellite with a tenth of its mass at z=0 and N low mass satellites with the most massive having 2.5% of its stellar mass.

Both BCGs start at intermediate λ_R values. They quickly become slow rotators during their mergers and stay slowly rotating. Both BCGs experience a significant jump in h_4 during the merger, followed by small growth with large scatter. Cs specific star formation rate is significantly increased by the merger (almost by a factor of 3) whereas the specific star formation rate of N decreases and eventually fluctuates around very low values. This leads to N having only half the specific star formation rate of C at z=0. The black holes behave akin to one another. Ns black hole accretes in the beginning when the halo has a cool core and accretes almost no mass during the entire time the halo has a non-cool core. Around the time the halo almost has a cool core the black hole doubles its mass and destroys the cool core again. The black hole of C has many phases when it does not accrete mass. During the time Cs halo has a non-cool core it accretes a significant fraction of its mass. Both BCGs have rapidly increasing gas temperatures during the initial time their parent halos have cool cores. Ns temperature decreases again and fluctuates around 1.8keV until z=0. Ns temperature fluctuates many time steps around 1.3keV followed by increasing temperatures eventually leading to both BCGs having roughly the same temperature although Ns temperature as initially twice as high. The b-value of both BCGs decreases significantly during their respective mergers and starts to fluctuate between $-5.7 < b < -5.4$ for both. There is a correlation between b-value and λ_R during the merger but not after. The same can be seen for the anti-correlation between b-value and h_4. Both BCGs experience a major merger although the mergers differ in their details (dry vs. wet, short vs. long merging). In contrast to the BCGs before we see similarities not only in the kinematics (intermediate, quickly decreasing and fluctuating λ_R and b-value) but also in their black hole masses and gas temperatures.

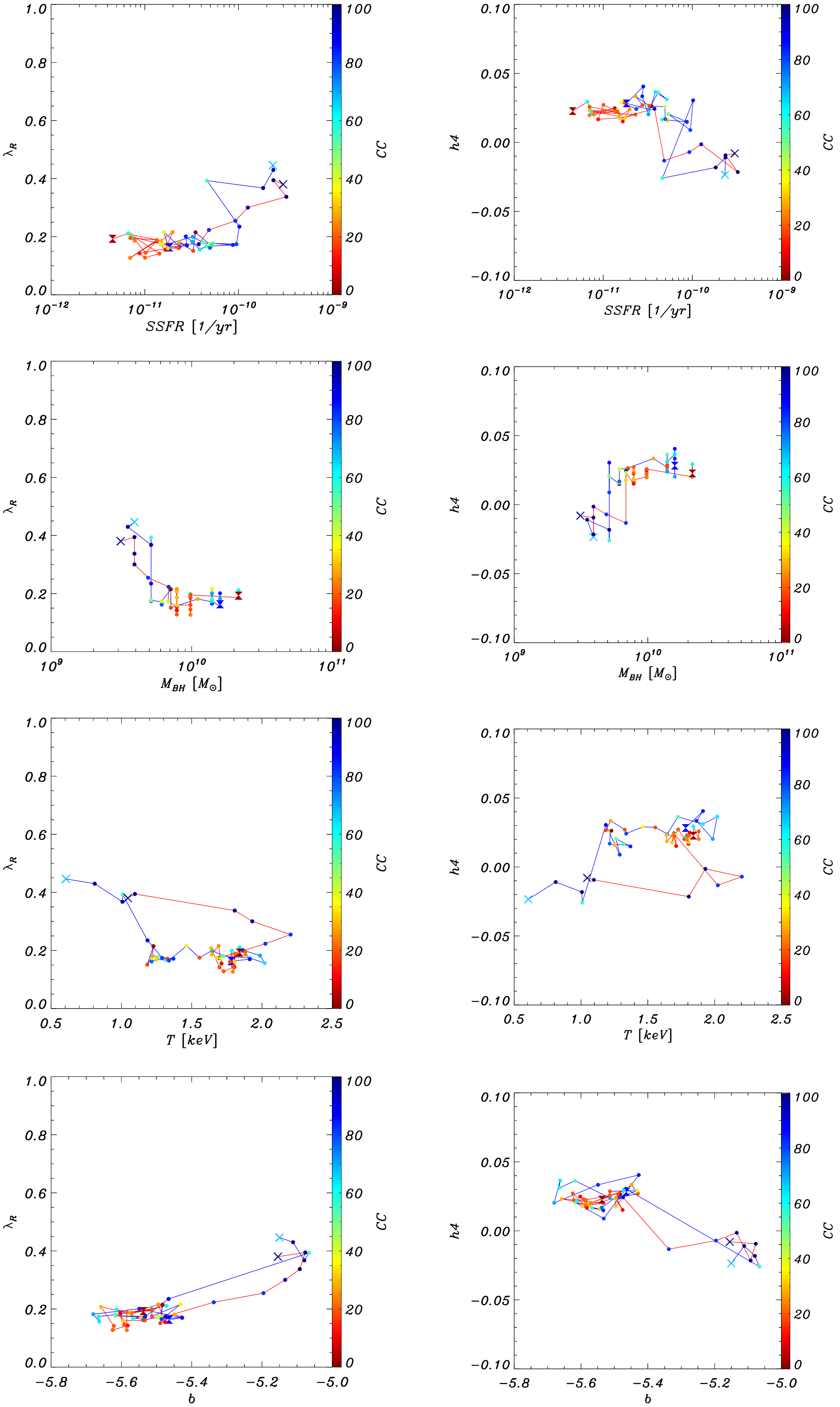

FIGURE 5.19: Relationship between kinematical properties λ_R, h_4 and environmental properties: specific star formation rate SSFR, black hole mass m_{BH}, gas temperature T and b-value. A detailed description can be found at the beginning of this section.

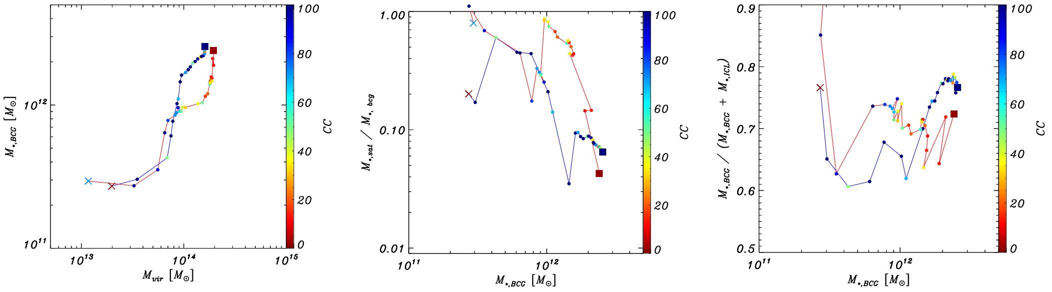

FIGURE 5.20: Evolution of masses in the same regions as before. A detailed description can be found at the beginning of this section.

Distinct Cores

From Fig. 5.20 it is possible to see that both of these BCGs have different merger histories. *C* experiences a major merger or many minor mergers at high redshift and a significant merger at intermediate redshift that is accompanied by a doubling of stellar mass although there is no satellite heavy enough to attribute this merger solely to. Followed by smooth accretion until z=0. *N* experiences a significant major merger at high redshift, followed by a period of smooth accretion and another major merger shortly before redshift zero. Consequently, their stellar ICL mass behaves differently. After their initial merging period *C* builds up more and more stellar mass in its central region whereas *N* increases the mass fraction in its ICL followed by strong fluctuations due to the violent mergers at low redshift.

Their evolutions of λ_R are different as well. λ_R of *C* increases slightly with lots of fluctuation during its initial merging, then generally decreases until it is slowly rotating. *N* becomes quickly slow rotating at high redshift and peaks enormously due to the major merger. This could be due to high velocities at large radii and does not need to have anything to do with rotation. This is underlined by the fact that λ_R decreases again very quickly. Both BCGs reach their minimum values in h_4 during their major mergers. Most of the time both BCGs have increasing h_4 values whereas *N*s are roughly twice as high as *C*s before the merger. The SSFR of both BCGs is generally decreasing. Only *C* receives significant gas supply during its mergers at high redshift. *N*s black hole increases its mass significantly during the early cool core phase but does not increase further during the following non-cool core phase except for a significant jump following the major merger when it roughly doubles its mass. *C*s black hole is initially not accreting a lot of mass but triples its mass at intermediate redshift probably triggered by the major merger. This does not have either an immediate nor a long lasting impact on the coolcoreness. Both BCGs start at similar gas temperatures, increase their temperatures significantly in the beginning but fluctuate at intermediate values until redshift zero. *C* shows the expected albeit hard to see correlation between λ_R and b and anti-correlation between h_4 and b. *N*s b-value is heavily fluctuating most of the time and changes significantly because of the merger. This suggests that the core formed shortly before z=0 when the strongly rotating satellite was incorporated in the centre. These BCGs show that the kinematical pattern can evolve over a long time but do not have to. They show very different merger histories with one BCG experiencing a violent major merger just shortly before z=0. This is nicely illustrated with the $\lambda_R - b$ plot. Overall they show similar behaviour in SSFR, black hole mass and gas temperature where the differences can mostly be attributed to their different merger histories.

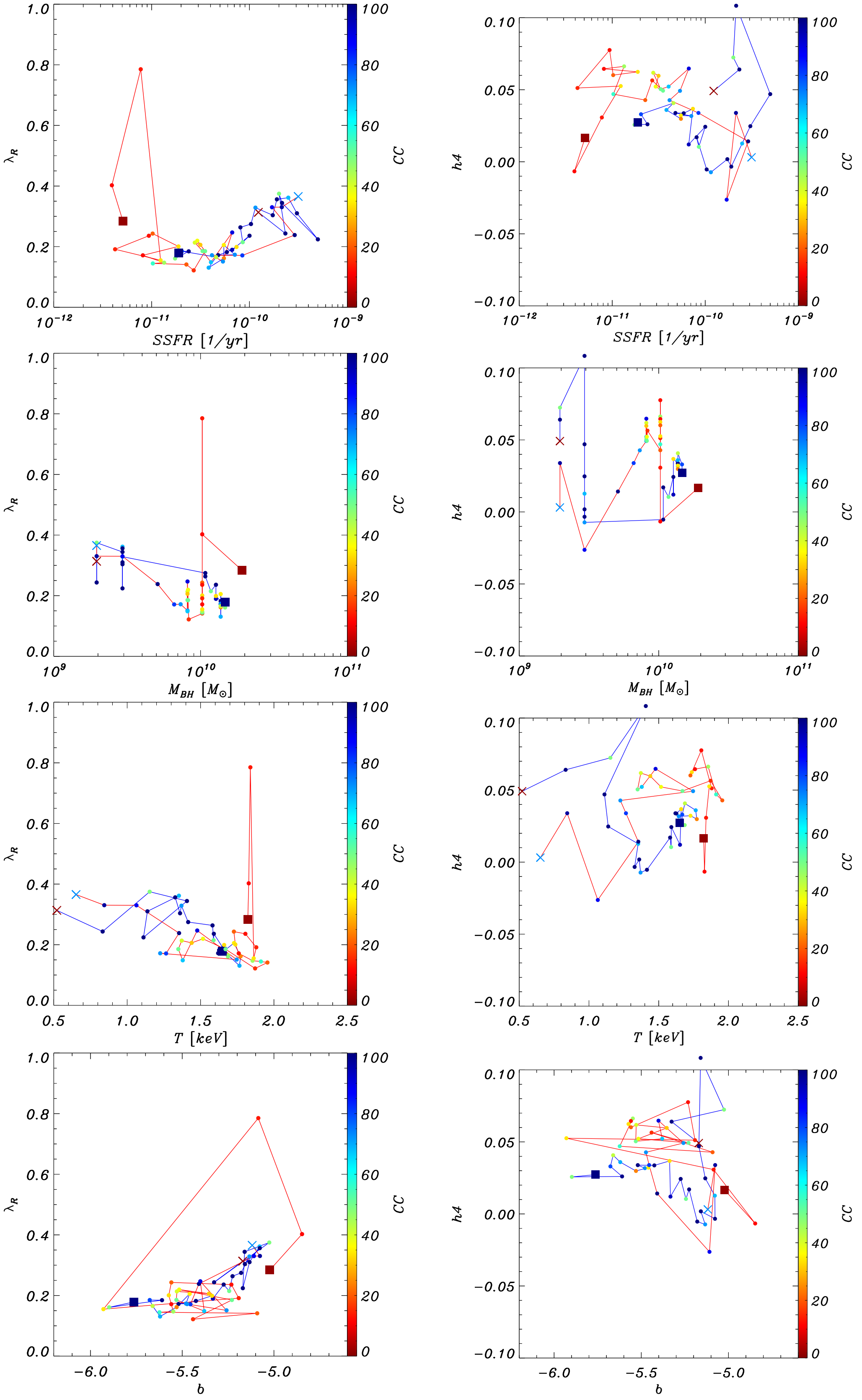

FIGURE 5.21: Relationship between kinematical properties λ_R, h_4 and environmental properties: specific star formation rate SSFR, black hole mass m_{BH}, gas temperature T and b-value. A detailed description can be found at the beginning of this section.

5.3 Summary

We see that the evolution of kinematics is determined by a delicate interplay between environmental properties and merger history. BCGs in cool core clusters and non-cool core clusters both experience all different kinds of mergers. Although the only wet major mergers were found for cool cores.
From the sample above it is not possible to tell if the stellar mass distribution between central region and ICL is connected to either kinematical type or coolcoreness since both the NRs and the RRs behave similar but the PRs and the DCs show opposite behaviour. Therefore, this could be depended on the individual merger histories of each BCG.
The evolution of λ_R and b seems to be specific for each kinematical type and does not depend on coolcoreness or other global environmental properties. NRs are generally slowly rotating already at z=2 with strongly fluctuating b. The PRs show higher λ_R values at high redshift but decrease their λ_R quickly during a major merger event. The b-value is reduced quickly during the merger event as well and starts fluctuating around low values. The poster child DC and the cool core DC both show slowly decreasing λ_R and b that form a linear correlation. The non-cool core BCG shows that distinct cores can also form as a result of a major merger where the behaviour between λ_R and b before the merger resembled more that of a non-rotator. The RRs also show two different formation mechanisms. The non-cool core rotator shows rather expected behaviour. High λ_R and b for high redshift. Both values decrease over time such that they form a steep linear correlation. Both the poster child RR (that is a cool core most the observed time and a weak cool core at z=0) and the cool core RR are slowly rotating for the entire redshift range with the exception of the cool core RR increasing its λ_R again at low redshift. Both increase their b-value over the redshift range significantly such that they are comparable to the regular rotator that decreased its b-value. Because of the late increase in λ_R for the cool core RR a correlation between λ_R and b can be observed as well. It seems that one formation channel keeps its initial rotation and the other builds up rotation. Further investigation is needed to confidently state what drives these different formation mechanisms. From this very small sample it seems that the BCGs must not be disturbed by major merger for a long time. Especially the regular rotators that keep their initial rotation. Both RRs that build up rotation show relatively high star formation rates but differ in black hole growth and temperature significantly. They both have a relatively cool core for most of the observed redshift.
The evolution of h_4 seems more complicated because it is sensitive to mergers. It depends on the individual merger conditions if it leads to a rise or a fall and - in contrast to λ_R - h_4 shows different behaviour if there is a cool core and if there is none. All three NRs show decreasing h_4 during the cool core phase and increasing h_4 during the non-cool core phase. The same decreasing behaviour is found for the cool core RR and the same increasing behaviour is found for the non-cool core RR. The poster child RR, however, is constantly at intermediate h_4. The h_4 of the cool core and the non-cool core PR are initially at low values but jump to higher values after the major merger and stay relatively constant subsequently. The poster child PR has rising h_4 through intermediate CCness but the lowest values are found when there is a cool core. The poster child DC fits the aforementioned behaviour of a falling h_4 during the cool core phase and a rising h_4 during the non-cool core phase. Although it is important to note that this BCG always has extremely low h_4 values. Both the non-cool core and cool core DC show rising h_4 during their respective cool core phase which is contrary to the observations above. In total eight out of twelve

investigated galaxies show both falling h_4 during cool core phase and rising h_4 during non cool core phase. The others show parts or none of these features.
There seems to be a correlation between the development of a non-cool core and the mass accretion history of the black hole. Both NRs that have a non-cool core at z=0 show significant BH accretion during their cool core phase and small accretion afterwards. The BH of the cool core NR is not accreting except for one strong jump in mass during its merger. It is unclear if the cool core is destroyed for one data point due to the BH or due to a misplacement during the merger. Something similar can be observed for the RRs. The BH of the non-cool core RR is accreting significantly during the cool core phase but less at low redshift. The BH of the cool core RR is almost not accreting except for one big jump that seems to destroy the cool core for one data point. Here the event does not coincide with a merger. The black hole of the poster child RR increases its mass significantly during the initial cool core phase. Contrary to the above the non-cool core and cool core PR have comparable black hole masses during the entire redshift range. The non-cool core PR is increasing during the initial cool core phase but stops after it loses its cool core except for a significant jump at low redshift that does not seem to coincide with a merger. The cool core PR also increases during the initial cool core phase and during its non-cool core phase but nowhere else. The BH mass of the poster child PR increases significantly during the initial and a second cool core phase. The BH of the non-cool core DC shows significant black hole accretion during the initial cool core phase but none after except for the significant jump during the major merger. The black hole of the cool core DC also accretes enormously after a lot of mass from the major merger fell into the central region but it did not accrete during the initial cool core phase. The poster child DC shows constant black hole accretion up until very high masses. In total five out of five BCGs that develop a non-cool core show significant black hole accretion during the initial cool core phase and most show smaller accretion at smaller redshift. These accretion rates cannot be found for any of the five BCGs that keep their cool core although their black holes can strongly accrete during mergers. The two BCGs that have an intermediate cool core at z=0 also show significant black hole mass accretion rate at high redshift. Therefore, it can be assumed that they lose their cool core too.
The specific star formation rate is on average higher for BCGs with a cool core, although every BCG shows generally decreasing SSFR with the exception of gas inflow through wet mergers. The gas temperature seems to be vaguely correlated with BH mass and coolcoreness but does not show correlations with any of the other properties.

Chapter 6

Exodus

This thesis provided a detailed statistical and individual analysis of kinematical and environmental properties for a large sample of BCGs from a fully cosmological, hydrodynamical simulation. As a first step the velocity maps of the most massive BCGs at z=0 were classified, resulting in a sample of 298 BCGs divided into four kinematical types: non-rotators, regular rotators, prolate rotators and BCGs with a kinematically distinct core. This sample was compared to observational data from *MASSIVE* (Ma et al., 2014), the Atlas 3D survey (Emsellem, Cappellari, Krajnović, et al., 2011) and Kravtsov, Vikhlinin, and Meshcheryakov (2014). Despite the masses being significantly larger than the masses in observations (mostly because kinematics of galaxies at this mass range have yet to be observed) the kinematics of MAGNETICUM BCGs are in good agreement with observations. As a second step the temporal evolution of kinematical and environmental properties was investigated. To begin with, the statistical redshift evolution of individual properties was analysed for a sample 250 traced BCGs. Finally, a case study of 12 BCGs was completed where the dependent evolution between kinematical and environmental properties was examined. Six of these galaxies developed a non-cool core and four galaxies kept their cool core. Thus we arrive at the following conclusions:

- No general correlation between the evolution of the angular momentum proxy λ_R and the evolution of specific star formation rate, black hole mass or gas temperature could be found. $\lambda_R(z)$ rather depends on each individual merger history. Furthermore, it was shown that the relationship between λ_R and b-value for different redshift is more complex than the theoretical prediction in F. Schulze et al. (2018). Regular rotators and distinct cores usually show an increasing correlation curve whereas non-rotators and prolate rotators (after they experienced the major merger) show a strongly fluctuating relationship between these two properties.

- BCGs with a regular rotation pattern can evolve from slowly rotating, low b-value galaxies by increasing their b-value. This effect might be connected to the existence of a cool core although a larger sample needs to be studied to confirm this suspicion. Nevertheless, a possible formation mechanism of rotation for high mass BCGs could explain the decreasing non-rotator fractions for high stellar masses at z=0.

- A redshift dependent evolution of the h_3 parameter could not be found at all. The median value of this parameter is remarkably close to zero for the entire redshift range between $2 > z > 0$.

- This is contrasted by a significantly increasing h_4 parameter. The median value at z=2 corresponds to roughly 20% of the median h_4 at z=0 for all kinematical types except the BCGs with a kinematically distinct core. Some BCGs show an anti-correlation between h_4 and b-value.

- All 250 traced BCGs show a cool core phase during the peak of cosmic star formation rate. The development of a stable non-cool core is a continuous process that spans several Gyrs. This process might be triggered by strong mass accretion of the black hole at a redshift around z=2. Six out of six BCGs that developed a non-cool core showed strong dynamical black hole mass accretion at that time and four out of four of the BCGs that kept their cool core only had small to no dynamical mass accretion. None of the twelve individually investigated BCGs showed a non-cool core turning back to a cool core although this was no selection criterion. Subsequently, the median coolcoreness decreases with time. At redshift z=0 roughly 60% of the sample have a core with a coolcoreness above 50%. However, the sample spans the entire range of coolcoreness for all kinematical types.

- There is no apparent scaling between coolcoreness and kinematical properties at z=0. However, the h_4 parameter showed signs of influence through environmental properties. Eight out of twelve BCGs showed an increasing h_4 parameter during their cool-core phase and a decreasing h_4 during the non-cool core phase. The suggestion of an anti-correlation between h_4 and coolcoreness is additionally backed up by the opposite time development mentioned above. The low h_4 values that are found in the centres of BCGs of all kinematical types except the distinct cores could be a relic of that evolution. Low h_4 values in the centres of slow rotating galaxies are not observed in van de Sande et al. (2017). This further adds to the suspicion that this is a property exclusive to BCGs. A possible theoretical explanation for the correlation between coolcoreness and h_4 could be that a cool core is responsible for similar circular orbits in the inner part of BCGs.

These findings support the idea of different kinematical types having their origin in different merger scenarios even at the extremely high mass end. Additionally, the λ_R parameter seems to be mainly a product of merger history. Finally, the data suggest that there is some form of correlation between the cluster environment and stellar kinematics in the form of the coolcoreness and the h_4 parameter.

List of Abbreviations

AGN	**A**ctive **G**alactic **N**ucleus
BCG	**B**rightest **C**luster **G**alaxy
BH	**B**lack **H**ole
CMB	**C**osmic **M**icrowave **B**ackground
CC	**C**ool **C**ore
DC	**D**istinct **C**ore
DM	**D**ark **M**atter
ETG	**E**arly **T**ype **G**alaxy
HST	**H**ubble **S**pace **T**elescope
ICL	**I**ntra **C**luster **L**ight
ICM	**I**ntra **C**luster **M**edium
Λ**CDM**	Cosmological Constant **C**old **D**ark **M**atter
LOSVD	**L**ine-**O**f-**S**ight **V**elocity **D**istribution
LTG	**L**ate **T**ype **G**alaxy
MOND	**MO**dified **N**ewtonian **G**ravity
NR	**N**on-**R**otator
NCC	**N**on-**C**ool **C**ore
RR	**R**egular **R**otator
PR	**P**rolate **R**otator
SMBH	**S**uper **M**assive **B**lack **H**ole
SPH	**S**moothed **P**article **H**ydrodynamics
SSFR	**S**pecific **S**tar **F**ormation **R**ate
VLT	**V**ery **L**arge **T**elescope

Bibliography

Beck, A. M. et al. (2015). *An improved SPH scheme for cosmological simulations*. arXiv: 1502.07358 [astro-ph.CO].

Bender, R., R. P. Saglia, and O. E. Gerhard (Aug. 1994). "Line-of-sight velocity distributions of elliptical galaxies." In: 269, pp. 785–813. DOI: 10.1093/mnras/269.3.785.

Böhringer, H., K. Dolag, and G. Chon (Mar. 2012). "Modelling self-similar appearance of galaxy clusters in X-rays". In: 539, A120, A120. DOI: 10.1051/0004-6361/201118000. arXiv: 1112.5035.

Bois, Maxime et al. (Sept. 2011). "The ATLAS3D project – VI. Simulations of binary galaxy mergers and the link with fast rotators, slow rotators and kinematically distinct cores". In: *Monthly Notices of the Royal Astronomical Society* 416.3, pp. 1654–1679. ISSN: 0035-8711. DOI: 10.1111/j.1365-2966.2011.19113.x. eprint: https://academic.oup.com/mnras/article-pdf/416/3/1654/2836988/mnras0416-1654.pdf. URL: https://doi.org/10.1111/j.1365-2966.2011.19113.x.

Bureau, M. and E. Athanassoula (June 2005). "Bar Diagnostics in Edge-On Spiral Galaxies. III. N-Body Simulations of Disks". In: 626.1, pp. 159–173. DOI: 10.1086/430056. arXiv: astro-ph/0403226 [astro-ph].

Cappellari, Michele, Eric Emsellem, R. Bacon, et al. (July 2007). "The SAURON project – X. The orbital anisotropy of elliptical and lenticular galaxies: revisiting the (V/σ,) diagram with integral-field stellar kinematics". In: *Monthly Notices of the Royal Astronomical Society* 379.2, pp. 418–444. ISSN: 0035-8711. DOI: 10.1111/j.1365-2966.2007.11963.x. eprint: https://academic.oup.com/mnras/article-pdf/379/2/418/3370236/mnras0379-0418.pdf. URL: https://doi.org/10.1111/j.1365-2966.2007.11963.x.

Cappellari, Michele, Eric Emsellem, Davor Krajnović, et al. (May 2011). "The ATLAS^{3D} project - I. A volume-limited sample of 260 nearby early-type galaxies: science goals and selection criteria". In: 413.2, pp. 813–836. DOI: 10.1111/j.1365-2966.2010.18174.x. arXiv: 1012.1551 [astro-ph.CO].

Clowe, Douglas, Anthony Gonzalez, and Maxim Markevitch (Apr. 2004). "Weak-Lensing Mass Reconstruction of the Interacting Cluster 1E 0657558: Direct Evidence for the Existence of Dark Matter". In: *The Astrophysical Journal* 604.2, pp. 596–603. ISSN: 1538-4357. DOI: 10.1086/381970. URL: http://dx.doi.org/10.1086/381970.

Dolag, K., S. Borgani, et al. (Oct. 2009). "Substructures in hydrodynamical cluster simulations". In: 399.2, pp. 497–514. DOI: 10.1111/j.1365-2966.2009.15034.x. arXiv: 0808.3401 [astro-ph].

Dolag, K., M. Jubelgas, et al. (May 2004). "Thermal Conduction in Simulated Galaxy Clusters". In: 606.2, pp. L97–L100. DOI: 10.1086/420966. arXiv: astro-ph/0401470 [astro-ph].

Dolag, K. and F. Stasyszyn (Oct. 2009). "An MHD GADGET for cosmological simulations". In: 398.4, pp. 1678–1697. DOI: 10.1111/j.1365-2966.2009.15181.x. arXiv: 0807.3553 [astro-ph].

Dolag, K., F. Vazza, et al. (Dec. 2005). "Turbulent gas motions in galaxy cluster simulations: the role of smoothed particle hydrodynamics viscosity". In: 364.3, pp. 753–772. DOI: `10.1111/j.1365-2966.2005.09630.x`. arXiv: `astro-ph/0507480 [astro-ph]`.

Emsellem, Eric, Michele Cappellari, Davor Krajnović, et al. (July 2007). "The SAURON project – IX. A kinematic classification for early-type galaxies". In: *Monthly Notices of the Royal Astronomical Society* 379.2, pp. 401–417. ISSN: 0035-8711. DOI: `10.1111/j.1365-2966.2007.11752.x`. eprint: `https://academic.oup.com/mnras/article-pdf/379/2/401/3368364/mnras0379-0401.pdf`. URL: `https://doi.org/10.1111/j.1365-2966.2007.11752.x`.

Emsellem, Eric, Michele Cappellari, Davor Krajnović, et al. (June 2011). "The ATLAS^{3D} project - III. A census of the stellar angular momentum within the effective radius of early-type galaxies: unveiling the distribution of fast and slow rotators". In: 414.2, pp. 888–912. DOI: `10.1111/j.1365-2966.2011.18496.x`. arXiv: `1102.4444 [astro-ph.CO]`.

Emsellem, Eric, Michele Cappellari, Reynier F. Peletier, et al. (Aug. 2004). "The SAURON project - III. Integral-field absorption-line kinematics of 48 elliptical and lenticular galaxies". In: 352.3, pp. 721–743. DOI: `10.1111/j.1365-2966.2004.07948.x`. arXiv: `astro-ph/0404034 [astro-ph]`.

Fabian, A. C. (1994). "Cooling Flows in Clusters of Galaxies". In: *Annual Review of Astronomy and Astrophysics* 32.1, pp. 277–318. DOI: `10.1146/annurev.aa.32.090194.001425`. eprint: `https://doi.org/10.1146/annurev.aa.32.090194.001425`. URL: `https://doi.org/10.1146/annurev.aa.32.090194.001425`.

Fabian, A. C. et al. (Apr. 1974). "Copernicus X-Ray Observations of NGC 1275 and the Core of the Perseus Cluster". In: 189, p. L59. DOI: `10.1086/181464`.

Fabjan, D. et al. (Jan. 2010). "Simulating the effect of active galactic nuclei feedback on the metal enrichment of galaxy clusters". In: 401.3, pp. 1670–1690. DOI: `10.1111/j.1365-2966.2009.15794.x`. arXiv: `0909.0664 [astro-ph.CO]`.

Fall, S. M. (Jan. 1983). "Galaxy formation - Some comparisons between theory and observation". In: *Internal Kinematics and Dynamics of Galaxies*. Ed. by E. Athanassoula. Vol. 100. IAU Symposium, pp. 391–398.

Frenk, C.S. and S.D.M. White (Sept. 2012). "Dark matter and cosmic structure". In: *Annalen der Physik* 524.9-10, pp. 507–534. ISSN: 0003-3804. DOI: `10.1002/andp.201200212`. URL: `http://dx.doi.org/10.1002/andp.201200212`.

Genzel, R. and A. Eckart (1999). "The Galactic Center Black Hole". In: *The Central Parsecs of the Galaxy*. Ed. by Heino Falcke et al. Vol. 186. Astronomical Society of the Pacific Conference Series, p. 3.

Gerhard, O. E. (Nov. 1993). "Line-of-sight velocity profiles in spherical galaxies: breaking the degeneracy between anisotropy and mass." In: 265, p. 213. DOI: `10.1093/mnras/265.1.213`.

Hinz, Jennifer (Jan. 2018). "Cool Core Clusters in the Magneticum Pathfinder Simulation". In: eprint: `https://www.usm.uni-muenchen.de/CAST/cms/media/theses/bachelor/BachelorThesis_JenniferHinz.pdf`.

Hirschmann, Michaela et al. (Aug. 2014). "Cosmological simulations of black hole growth: AGN luminosities and downsizing". In: 442.3, pp. 2304–2324. DOI: `10.1093/mnras/stu1023`. arXiv: `1308.0333 [astro-ph.CO]`.

Hubble, E. P. (Dec. 1926). "Extragalactic nebulae." In: 64, pp. 321–369. DOI: `10.1086/143018`.

Hudson, D. S. et al. (Apr. 2010). "What is a cool-core cluster? a detailed analysis of the cores of the X-ray flux-limitedHIFLUGCScluster sample". In: *Astronomy and*

Astrophysics 513, A37. ISSN: 1432-0746. DOI: 10.1051/0004-6361/200912377. URL: http://dx.doi.org/10.1051/0004-6361/200912377.

Komatsu, E. et al. (2010). "Seven-Year Wilkinson Microwave Anisotropy Probe (WMAP) Observations: Cosmological Interpretation". In: DOI: 10.1088/0067-0049/192/2/18. eprint: arXiv:1001.4538.

Krajnović, Davor et al. (Apr. 2018). "Climbing to the top of the galactic mass ladder: evidence for frequent prolate-like rotation among the most massive galaxies". In: *Monthly Notices of the Royal Astronomical Society* 477.4, pp. 5327–5337. ISSN: 0035-8711. DOI: 10.1093/mnras/sty1031. eprint: https://academic.oup.com/mnras/article-pdf/477/4/5327/25101377/sty1031.pdf. URL: https://doi.org/10.1093/mnras/sty1031.

Kravtsov, A. V., A. A. Vikhlinin, and A. V. Meshcheryakov (Jan. 2014). "Stellar Mass—Halo Mass Relation and Star Formation Efficiency in High-Mass Halos". In: *Astronomy Letters* 44.1, pp. 8–34. ISSN: 1562-6873. DOI: 10.1134/s1063773717120015. URL: http://dx.doi.org/10.1134/S1063773717120015.

Li, Yuan and Greg L. Bryan (Feb. 2012). "SIMULATING THE COOLING FLOW OF COOL-CORE CLUSTERS". In: *The Astrophysical Journal* 747.1, p. 26. DOI: 10.1088/0004-637x/747/1/26. URL: https://doi.org/10.1088%2F0004-637x%2F747%2F1%2F26.

Ma, Chung-Pei et al. (Nov. 2014). "The MASSIVE Survey. I. A Volume-limited Integral-field Spectroscopic Study of the Most Massive Early-type Galaxies within 108 Mpc". In: 795, 158, p. 158. DOI: 10.1088/0004-637X/795/2/158. arXiv: 1407.1054 [astro-ph.GA].

McNamara, B. R. and P. E. J. Nulsen (Sept. 2007). "Heating Hot Atmospheres with Active Galactic Nuclei". In: 45.1, pp. 117–175. DOI: 10.1146/annurev.astro.45.051806.110625. arXiv: 0709.2152 [astro-ph].

Moster, B. P. (2013). "Simulated Galaxy Merger Trees: A New Numerical Tool to Study Galaxy Evolution". In: *Galaxy Mergers in an Evolving Universe*. Ed. by W. -H. Sun et al. Vol. 477. Astronomical Society of the Pacific Conference Series, p. 115.

Naab, Thorsten and Andreas Burkert (July 2001). "The Formation of Disks in Elliptical Galaxies". In: 555.2, pp. L91–L94. DOI: 10.1086/323182. arXiv: astro-ph/0103476 [astro-ph].

Naab, Thorsten, L. Oser, et al. (Nov. 2014). "The ATLAS^{3D} project - XXV. Two-dimensional kinematic analysis of simulated galaxies and the cosmological origin of fast and slow rotators". In: 444.4, pp. 3357–3387. DOI: 10.1093/mnras/stt1919. arXiv: 1311.0284 [astro-ph.CO].

Oort, J. H. (Apr. 1940). "Some Problems Concerning the Structure and Dynamics of the Galactic System and the Elliptical Nebulae NGC 3115 and 4494." In: 91, p. 273. DOI: 10.1086/144167.

Oser, Ludwig et al. (Dec. 2010). "The Two Phases of Galaxy Formation". In: 725.2, pp. 2312–2323. DOI: 10.1088/0004-637X/725/2/2312. arXiv: 1010.1381 [astro-ph.CO].

Penzias, A. A. and R. W. Wilson (July 1965). "A Measurement of Excess Antenna Temperature at 4080 Mc/s." In: 142, pp. 419–421. DOI: 10.1086/148307.

Perlmutter, S. et al. (June 1999). "Measurements of Ω and Λ from 42 High-Redshift Supernovae". In: *The Astrophysical Journal* 517.2, pp. 565–586. ISSN: 1538-4357. DOI: 10.1086/307221. URL: http://dx.doi.org/10.1086/307221.

Peterson, J.R. and A.C. Fabian (2006). "X-ray spectroscopy of cooling clusters". In: *Physics Reports* 427.1, pp. 1–39. ISSN: 0370-1573. DOI: https://doi.org/10.1016/j.physrep.2005.12.007. URL: http://www.sciencedirect.com/science/article/pii/S0370157306000020.

Ragagnin, A. et al. (July 2017). “A web portal for hydrodynamical, cosmological simulations”. In: *Astronomy and Computing* 20, pp. 52–67. DOI: 10.1016/j.ascom.2017.05.001. arXiv: 1612.06380 [astro-ph.IM].

Remus, Rhea-Silvia (Apr. 2015). “The Outer Halos of Elliptical Galaxies –Implications for their Formation Histories”. In: eprint: https://edoc.ub.uni-muenchen.de/18420/1/Remus_Rhea-Silvia.pdf.

Remus, Rhea-Silvia, Klaus Dolag, and Tadziu Hoffmann (Sept. 2017). “The Outer Halos of Very Massive Galaxies: BCGs and their DSC in the Magneticum Simulations”. In: *Galaxies* 5.3, p. 49. DOI: 10.3390/galaxies5030049. arXiv: 1709.02393 [astro-ph.GA].

Röttgers, Bernhard, Thorsten Naab, and Ludwig Oser (Dec. 2014). “Stellar orbits in cosmological galaxy simulations: the connection to formation history and line-of-sight kinematics”. In: 445.2, pp. 1065–1083. DOI: 10.1093/mnras/stu1762. arXiv: 1406.6696 [astro-ph.GA].

Schulze, F. et al. (Nov. 2018). “Kinematics of simulated galaxies - I. Connecting dynamical and morphological properties of early-type galaxies at different redshifts”. In: 480, pp. 4636–4658. DOI: 10.1093/mnras/sty2090. arXiv: 1802.01583.

Schulze, Felix, Rhea-Silvia Remus, and Klaus Dolag (Aug. 2017). “On the Kinematics, Stability and Lifetime of Kinematically Distinct Cores: A Case Study”. In: *Galaxies* 5, p. 41. DOI: 10.3390/galaxies5030041. arXiv: 1708.05390 [astro-ph.GA].

Schulze, Felix, Rhea-Silvia Remus, Klaus Dolag, et al. (Apr. 2020). “Kinematics of simulated galaxies II: Probing the stellar kinematics of galaxies out to large radii”. In: 493.3, pp. 3778–3799. DOI: 10.1093/mnras/staa511. arXiv: 2001.02237 [astro-ph.GA].

Springel, Volker (Dec. 2005). “The cosmological simulation code gadget-2”. In: *Monthly Notices of the Royal Astronomical Society* 364.4, pp. 1105–1134. ISSN: 1365-2966. DOI: 10.1111/j.1365-2966.2005.09655.x. URL: http://dx.doi.org/10.1111/j.1365-2966.2005.09655.x.

Springel, Volker and Lars Hernquist (Feb. 2003). “Cosmological smoothed particle hydrodynamics simulations: a hybrid multiphase model for star formation”. In: 339.2, pp. 289–311. DOI: 10.1046/j.1365-8711.2003.06206.x. arXiv: astro-ph/0206393 [astro-ph].

Springel, Volker, Simon D. M. White, et al. (June 2005). “Simulations of the formation, evolution and clustering of galaxies and quasars”. In: 435.7042, pp. 629–636. DOI: 10.1038/nature03597. arXiv: astro-ph/0504097 [astro-ph].

Teklu, Adelheid F. et al. (Oct. 2015). “Connecting Angular Momentum and Galactic Dynamics: The Complex Interplay between Spin, Mass, and Morphology”. In: 812.1, 29, p. 29. DOI: 10.1088/0004-637X/812/1/29. arXiv: 1503.03501 [astro-ph.GA].

Tornatore, L. et al. (July 2003). “Cooling and heating the intracluster medium in hydrodynamical simulations”. In: 342.4, pp. 1025–1040. DOI: 10.1046/j.1365-8711.2003.06631.x. arXiv: astro-ph/0302575 [astro-ph].

van de Sande, Jesse et al. (Jan. 2017). “The SAMI Galaxy Survey: Revisiting Galaxy Classification through High-order Stellar Kinematics”. In: 835.1, 104, p. 104. DOI: 10.3847/1538-4357/835/1/104. arXiv: 1611.07039 [astro-ph.GA].

van der Marel, Roeland P. and Marijn Franx (Apr. 1993). “A New Method for the Identification of Non-Gaussian Line Profiles in Elliptical Galaxies”. In: 407, p. 525. DOI: 10.1086/172534.

Veale, Melanie et al. (June 2017). “The MASSIVE Survey – VII. The relationship of angular momentum, stellar mass and environment of early-type galaxies”. In:

Monthly Notices of the Royal Astronomical Society 471.2, pp. 1428–1445. ISSN: 1365-2966. DOI: `10.1093/mnras/stx1639`. URL: `http://dx.doi.org/10.1093/mnras/stx1639`.

Watson, Scott (2000). *An Exposition on Inflationary Cosmology*. arXiv: `astro-ph/0005003 [astro-ph]`.

Zwicky, Fritz (1933). *Die Rotverschiebung von Extraglaktischen Nebeln*. arXiv: `1711.01693 [astro-ph.IM]`.

Declaration of Authorship

Hiermit erkläre ich, die vorliegende Arbeit selbstständig verfasst zu haben und keine anderen als die in der Arbeit angegebenen Quellen und Hilfsmittel benutzt zu haben.

München,

Unterschrift: